Probing the Structure and Dynamics of a Protein-DNA Complex Using Electron Spin Resonance

by

Jessica L. Sarver

B.S. Chemistry, Penn State Behrend, 2005

Submitted to the Graduate Faculty of the Kenneth P. Dietrich

School of Arts and Sciences in partial fulfillment

of the requirements for the degree of

Doctor of Philosophy

University of Pittsburgh

2012

UNIVERSITY OF PITTSBURGH

DIETRICH SCHOOL OF ARTS AND SCIENCES

This dissertation was presented

by

Jessica L. Sarver

It was defended on

May 2, 2012

and approved by

David Waldeck, Ph.D., Professor, Department of Chemistry

Stephen Weber, Ph.D., Professor, Department of Chemistry

Linda Jen-Jacobson, Ph.D., Professor Emerita, Department of Biological Sciences

Dissertation Advisor: Sunil Saxena, Ph.D., Associate Professor, Department of Chemistry

Probing the Structure and Dynamics of a Protein-DNA Complex Using Electron Spin Resonance

Jessica Sarver, PhD

University of Pittsburgh, 2012

In this thesis, we employ site-directed spin labeling and electron spin resonance to probe the changes in structure and dynamics for different EcoRI-DNA complexes. EcoRI is a restriction endonuclease that, due to its high binding specificity, is a model system for investigating protein-DNA interactions. Distance constraints were previously obtained for spin-labeled mutants of EcoRI in complex with DNA. However, the length and flexibility of the spin label convolute these distance measurements, making it difficult to extract biologically relevant information. We performed molecular dynamics (MD) simulations on the spin-labeled EcoRI-DNA complex to understand the packing and dynamics of the spin label. We show that correlated distance constraints can be leveraged with MD simulations to learn about the preferred conformers of the spin label on sites in an α-helix and a β-strand. In addition, we used the simulations to gain information on the backbone motion at the spin-labeled site by measuring the C_α-C_α distributions.

Dynamics and order may play a role in the DNA binding specificity of EcoRI. We performed continuous wave (CW) experiments to measure the dynamics and order of EcoRI bound to its specific, miscognate (one base pair mismatch) and nonspecific (≥2 base pair mismatch) DNA sites. We analyzed CW spectra for three EcoRI complexes spin-labeled at various sites in a region of the protein that is believed to play a role in the binding specificity of EcoRI. Simulation of the spectra provided details on the change in dynamics and order in the different complexes. We found the protein-DNA interface to be most sensitive to the changes

between the complexes. Spin-labeled sites further from the DNA were found to show little variation in dynamics between the complexes.

Lastly, this thesis discusses the comparison of two distance measurement techniques for a metal-nitroxide system. We performed distance measurements between a bound Cu^{2+} and a spin label on two polyalanine peptides of differing length using DEER and relaxation-based saturation recovery experiments. By comparing the results of both measurements, we show that the relaxation-based technique is biased to shorter average distances. This work highlights the advantages of using DEER to perform metal-nitroxide distance measurements.

TABLE OF CONTENTS

LIST OF TABLES

LIST OF FIGURES

PREFACE

It has been a long, hard road. However, the road would have been longer, and exceedingly more difficult had it not been for the support and love I have had from so many people. First and foremost, I would like to thank my advisor, Sunil. From day one in his group he pushed me to be my best. I enjoyed the challenge as well as groaned about the hard work. However, I can ultimately look back on my PhD and know that I did my best and had his support all along the way. He has been a great teacher, mentor, and friend.

I would like to thank my committees: Dr. David Pratt and Dr. Adrian Michael for serving on my comprehensive exam committee and Dr. David Waldeck, Dr. Stephen Weber, and Dr. Linda Jen-Jacobson for serving on my dissertation committee. I would also like to thank Dr. Lillian Chong for serving as my proposal mentor.

I have spent many hours working on the spectrometer and analyzing and reanalyzing my data, however, this would not have been possible without many, many samples. I would like to thank my great collaborator Dr. Linda Jen-Jacobson and her previous graduate student, and my friend, Dr. Jacque Townsend. Jacque spent several hours (days?) in the cold room prepping EcoRI samples for me to run. I am very appreciative of all the work that went into preparing such great samples. I would like to thank Linda for reading over my manuscripts and data so thoroughly and providing me with wonderful advice. I would also like to thank Dr. Dan

Zuckerman for his advice with respect to my MD simulations and Mike Yonkunas who taught me how to do the simulations in the first place.

I have made some great friends at Pitt, especially within the Saxena group. I want to thank previous members, Dr. Soraya Pornsuwan, Dr. Katherine Stone, Dr. Sharon Ruthstein, Dr. Sangmi Jun, Dr. Zhongyu Yang, Dr. Byong-kyu Shin, and Gayathri Rajapackse. They taught me a lot about ESR spectroscopy and research in the Saxena lab. I would especially like to thank Katherine who has become one of my best friends and was a great mentor when I first joined the group. Sharon has also become a close friend and I thank her for the advice and support she provided for me during the few years we worked together in the Saxena group. I would also like to thank the current Saxena group members, Ming Ji, Ishara Silva, Tim Cunningham, Marshall McGoff, and Matt Shannon. I have enjoyed the group studies, birthday lunches and spats with the spectrometer with all of you. Thank-you Ming for letting me "pick your brain" all the time and Tim for being there to talk to. I would also like to thank Katie Micko, Sruti Bhaumik, and Amy Rupert for becoming close friends of mine throughout my graduate career. I have enjoyed their support through happy hours and coffee breaks.

Last but not least I want to thank my family for their unending support and love. I want to thank my parents for always helping me when I was in need and patiently listening to me talk about my science when they had no idea what I was saying. Thank-you to my sister Shannon, brother Shane, brother-in-law Scott, and my wonderful niece and nephew Sarah and Jackson. Having a great family behind you sometimes makes all the difference when life is stressing you out. They have provided me with many laughs and smiles. And lastly I would like to thank my love, Josh. He is my best friend and my anchor. He has been there every step of the way, carrying me part of the time. I thank him for all the support and love he has given me and the

great memories we share from our time together in Pittsburgh. And thank-you Bogus, for being the best dog a girl could have!

In this thesis, part of Chapter 2 was written in collaboration with Jacqueline Townsend, Gayathri Rajapackse, Linda Jen-Jacobson and Sunil Saxena and has been published in the Journal of Physical Chemistry B, 2012, 116, 4024-4033. The work in Chapter 3 was written in collaboration with Jacqueline Townsend, Sunil Saxena, Linda Jen-Jacobson and is in preparation for submission to Biochemistry.

1.0 INTRODUCTION

Site-directed spin labeling (SDSL) used in conjunction with electron spin resonance (ESR) spectroscopy has become an important biophysical tool to probe the structure and dynamics of biological systems. In SDSL, a spin label, possessing a stable nitroxide radical group, is site-specifically attached to the peptide or protein of interest.(*1-4*) The presence of the spin label can be used to probe distance constraints and dynamics within the system. Double electron-electron resonance (DEER), a pulsed ESR technique, is often used to measure the distance between two or more spin labels by measuring the dipolar interaction between them.(*5-8*) DEER is advantageous as it not only provides the average distance between the two spin labels, but a distance distribution as well. Alternatively, relaxation-based measurements, such as the pulsed saturation recovery experiment, can be used to measure the dipolar interaction between a slow (spin label) and fast (metal) relaxing spin.(*9-13*) The change in relaxation of the spin label in the presence and absence of the fast relaxing metal enables the average distance between the two spins to be determined. In addition to distance measurements, ESR can also be used to probe the dynamics of the spin-labeled system through continuous wave (CW) experiments. The spectral line shape of the CW spectrum is sensitive to the motional dynamics and order of the spin label and spin-labeled site. Therefore, quantitative information on dynamics can be gained by fitting the CW spectra to simulation.(*14-16*)

ESR is useful for probing systems that may not be amenable to other techniques such as NMR and X-ray crystallography. However, the added length and flexibility of the spin label convolutes the biologically relevant details that can be gained through ESR measurements. Therefore, an understanding of the packing and dynamics of the spin label is needed. In chapter 2, molecular dynamics simulations are used to extract the preferred conformers of the spin label in EcoRI, a restriction endonuclease. Comparison to DEER experimental distance distributions is used to validate the simulated results. The simulations provide insight into the preferred spin label conformations and backbone mobility at the spin-labeled sites of EcoRI.

Dynamics and order may be important determinants of the specificity with which some DNA-binding proteins recognize their specific DNA sites. For this reason, SDSL was used to resolve changes in the dynamics of EcoRI bound to its specific, miscognate (one base pair mismatch), and nonspecific ($\geq$ 2 base pair mismatch) DNA sites. CW spectra were collected and analyzed to measure the dynamics at several spin-labeled sites of EcoRI at two different frequencies. The results for the CW analyses are discussed in Chapter 3.

In Chapter 4, a comparison is made between two ESR-based distance measurement techniques. The distance between a bound Cu^{2+} ion and a spin label present on two polyalanine peptides of differing lengths is measured. Comparisons are made between the DEER and relaxation-based experiments in measuring the average distance and the effect the distance distribution has on these measurements.

The subsequent sections of this chapter will discuss the ESR theories and techniques utilized in the research presented in this thesis.

1.1 ESR INTERACTIONS OF A SPIN-LABELED SYSTEM

1.1.1 Site-Directed Spin Labeling of Biological Systems

Site-directed spin labeling (SDSL) is utilized in a variety of biological systems including soluble and membrane proteins as well as DNA and RNA.(*1, 4, 17-19*) SDSL is performed by first using site-directed mutagenesis to mutate the residue of interest into a cysteine residue. The free cysteine is then reacted with the spin labeling reagent methanethiosulfonate (MTS) which reacts with the sulfur group present on the end of the cysteine residue. The reaction scheme for SDSL is illustrated in Figure 1-1. The sulfur-sulfur bond that is formed between the cysteine residue and the spin label covalently links the spin label to the protein providing the unpaired electron spin needed to perform ESR measurements. Spin-labeled locations that are mostly solvent accessible are chosen so that they are accessible to the MTS. For such locations, labeling causes little to no perturbation to the protein structure or function.(*20-21*) For this reason, this is a widely utilized technique for performing ESR measurements on biological systems.

1.1.2 Spin Hamiltonian for a Nitroxide System

In the presence of an external magnetic field, the unpaired electron spin of the spin label interacts with the field, as well as with surrounding electron and nuclear spins. The spin Hamiltonian for the electron spin in a magnetic field can be written as:

$$\hat{\mathrm{H}} = \beta_e \vec{B} \cdot \vec{\vec{g}} \cdot \hat{S} + \hat{S} \cdot \vec{\vec{A}} \cdot \hat{I} \qquad (1\text{-}1)$$

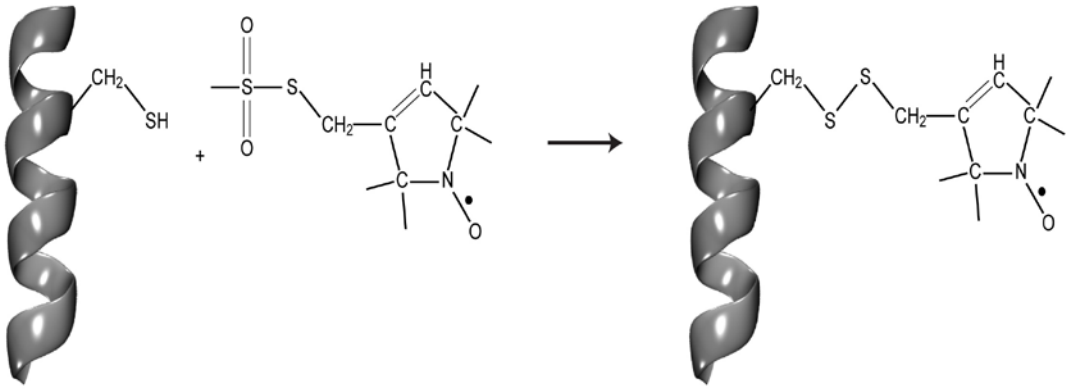

Figure 1-1. Site-directed spin labeling of a free cysteine on a peptide using the methanethiosulfonate (MTS) spin labeling reagent.

where β_e is the Bohr magneton, $\vec{B}$ is the external magnetic field vector, $\vec{g}$ is the electron g-tensor, and $\hat{S}$ is the electron spin angular momentum operator. In the second term, $\vec{A}$ is the hyperfine tensor and $\hat{I}$ is the nuclear spin angular momentum operator. The first term describes the Zeeman interaction between the electron spin and the external magnetic field. The second term is the hyperfine interaction between the electron and nuclear spins. In the spin label, this is the interaction between the unpaired electron and the nitrogen atom of the nitroxide. The hyperfine interaction consists of an isotropic (Fermi) and anisotropic term (dipolar).

In the case where the spin label is tumbling fast in solution (rotational rates of ~10^9-10^{11} s^{-1}), the anisotropy in the g and A-tensors will average out. In this case the isotropic g and A values can be used, and these are defined as:

$$g_{iso} = \tfrac{1}{3}\left(g_{xx} + g_{yy} + g_{zz}\right) \tag{1-2}$$

$$A_{iso} = \tfrac{1}{3}(A_{xx} + A_{yy} + A_{zz}) \tag{1-3}$$

where g_{xx}, g_{yy}, g_{zz}, A_{xx}, A_{yy}, and A_{zz} describe the principal components of the g-tensor and A-tensor.

If the external magnetic field is taken to be aligned along the z-axis and under the high-field approximation, the Hamiltonian can be rewritten as:

$$\hat{H} = g_{iso}\beta_e B_0 \hat{S}_z + A_{iso}\hat{S}_z\hat{I}_z \tag{1-4}$$

Here B_0 represents the z-component of the external magnetic field and $\hat{S}_z$ and $\hat{I}_z$ are the z-components of the electron and nuclear spin angular momentum operators, respectively. The electron Zeeman interaction breaks the degeneracy of the electron spin energy levels in the presence of an external magnetic field. This yields two energy levels for the spin states of the $\hat{S}_z$

operator characterized by the quantum numbers m_S = +1/2 and -1/2. Hence, the energy of each state can be expressed as:

$$E = g_{iso}\beta_e B_0 m_S + A_{iso} m_S m_I \tag{1-4}$$

where E is the energy of the level, and m_I is the quantum number for the nuclear spin state.

In the spin label the unpaired electron is delocalized over the nitroxide bond between the nitrogen and oxygen atoms. Due to the fact that the oxygen atom (^{16}O – natural abundance = 99.76%) has a nuclear spin quantum number of 0, there is no hyperfine interaction between the unpaired electron spin and oxygen atom nuclear spin. On the other hand, the nitrogen atom (^{14}N – natural abundance = 99.63%) has a nuclear spin quantum number of 1. Therefore three nuclear spin states of nitrogen can exist: m_I = +1, 0, -1. Due to the hyperfine interaction with the nitrogen nuclear spin, the energy levels of the electron spin are split even further. The electron spin energy levels and their splitting are illustrated in Figure 1-2. Based on the ESR selection rules, $\Delta m_S = \pm 1$ and $\Delta m_I = 0$, there are three allowed transitions.

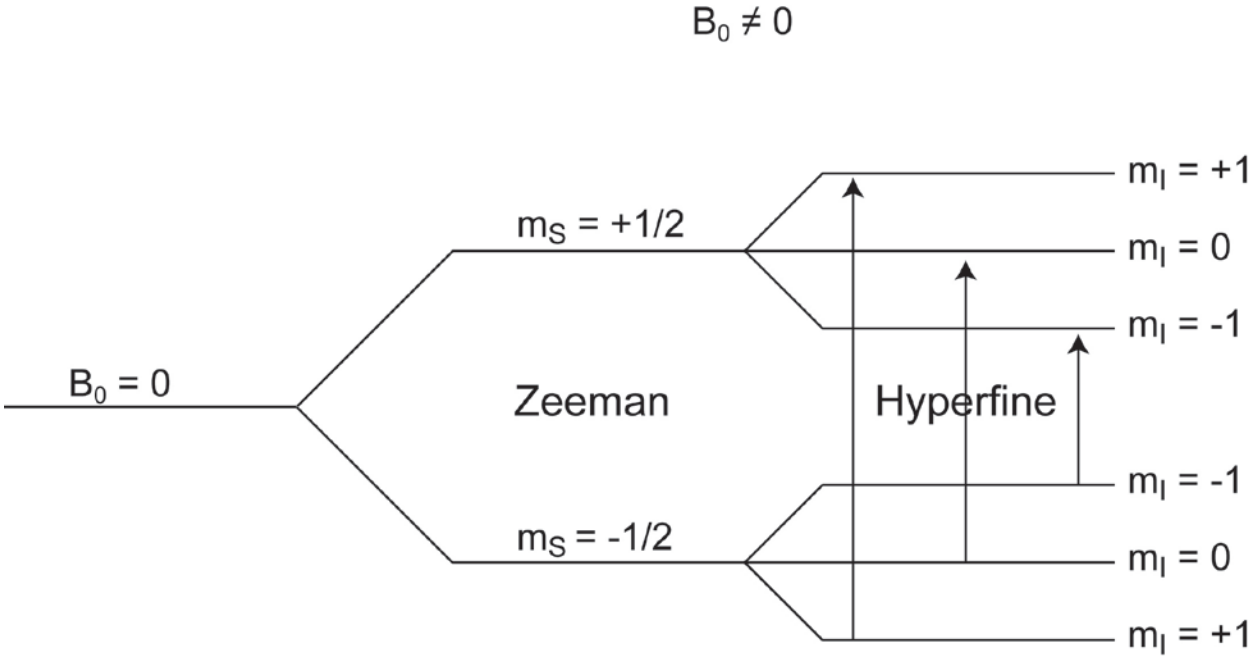

Figure 1-2. Nitroxide energy level diagram. In the absence of a magnetic field ($B_0 = 0$) the electron spin energy levels are degenerate. When an external magnetic field is applied ($B_0 \neq 0$), the electron spin energy levels split due to the Zeeman interaction. These energy levels are further split due to the hyperfine interaction with the neighboring nitrogen nuclear spin in the nitroxide moiety. The three allowed transitions are shown.

1.2 THE USE OF CONTINUOUS WAVE ESR TO PROBE MOLECULAR DYNAMICS

The transitions in Figure 1-2 give rise to the three peaks of the nitroxide CW spectrum. Due to the anisotropy of the g and hyperfine interactions, the resonance frequency of the electron spin is sensitive to the orientation of the spin label with respect to the magnetic field. This orientational sensitivity manifests itself in the characteristic line shapes of the nitroxide spectrum.

1.2.1 Orientational Sensitivity of the Nitroxide Spectrum

The contribution of the two anisotropic terms (g and hyperfine), and hence orientational effects, to the nitroxide CW spectrum is illustrated in Figure 1-3. In Figure 1-3A, the magnetic axes of the g- and A-tensors are defined with respect to the spin label. The orientation of these tensors has been resolved through theoretical and experimental studies.(*22*-*23*) The axes have been chosen so the g-values follow the trend $g_{xx} > g_{yy} > g_{zz}$. Thus, the g_{zz} axis lies along the p_z orbital of the nitrogen atom, the g_{xx} axis is parallel to the N-O bond, and g_{yy} is orthogonal to both axes. The typical values for the three magnetic axes of the g-tensor are: $g_{xx} = 2.009$, $g_{yy} = 2.006$, $g_{zz} = 2.002$.(*24*) Due to the different g-values, the resonance field for each orientation is different [equation (1-1)]. The orientational dependence of the nitroxide spectrum is shown in Figure 1-3B. Here, theoretical spectra were calculated with the magnetic field directed along each of the three magnetic axes individually. It can be seen that due to the difference in the g-values, the field positions of the x, y, and z oriented spectra differ (colored dashed lines).

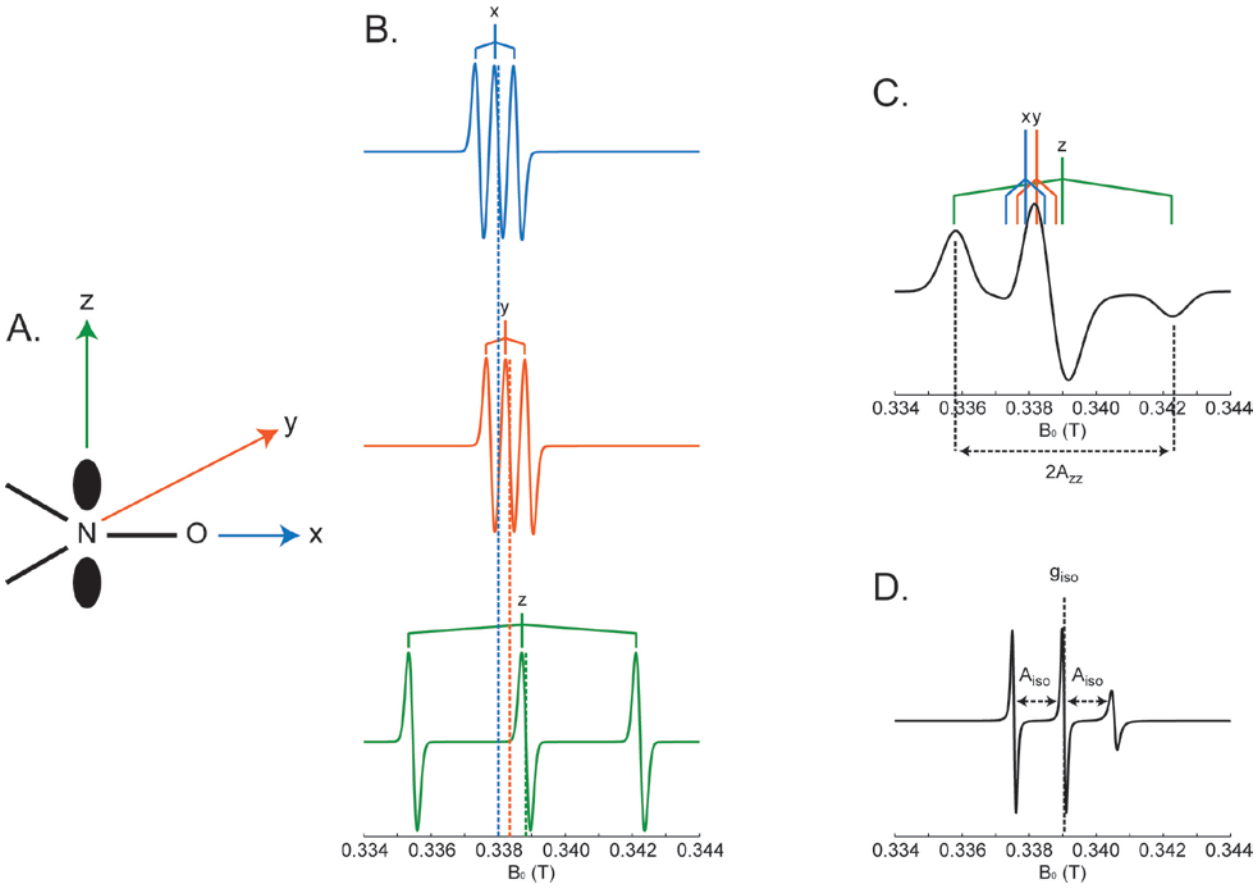

Figure 1-3. A. The orientation of the g- and A-tensors with respect to the spin label is defined along the three magnetic axes. B. The orientational effects of the g-values and hyperfine splitting. C. In a nitroxide powder (low temperature) spectrum only the $A_{zz,}$ hyperfine splitting is resolved. D. When the spin label undergoes faster motions the spectrum becomes isotropic, here the hyperfine splitting is reduced to the isotropic value.

In addition to the change in field position, each spectrum is split by the hyperfine coupling to the nitrogen atom as discussed in Section 1.1.2. Like the g-tensor, the hyperfine splitting is orientation dependent. However, in the spin label the g-tensor typically displays rhombic symmetry where as the hyperfine splitting values are axially symmetric. The typical values of the hyperfine splitting are: $A_{xx} \approx A_{yy} \approx 6$ G, $A_{zz} \approx 32$ G.(*24*) The orientation of the g-tensor and A-tensor is typically collinear.

At 9 GHz, the small shifts in the g-values and the small A_{xx} and A_{yy} hyperfine splitting are typically unresolved. Shown in Figure 1-3C is a powder (low temperature) nitroxide spectrum. The major characteristic of this spectrum is the A_{zz} hyperfine splitting ($2A_{zz}$ is highlighted by the dashed lines). All other orientational components overlap in the spectrum and contribute mainly to the central line width of the $m_I = 0$ (center) peak. In the case of a spin label experiencing fast rotational motion, these orientational effects are averaged out. This results in a nitroxide spectrum characterized by the isotropic g and A values. An isotropic nitroxide spectrum is shown in Figure 1-3D where the hyperfine splitting is reduced to the isotropic value ($A_{iso} \approx 18$ G).

1.2.2 CW Models Based on the Stochastic Liouville Equation

The differences between the spectra in Figures 1-3C and 1-3D demonstrate the sensitivity of the CW spectrum to the motional dynamics of the spin label. To further illustrate this point, nitroxide spectra were simulated using different spin label rotational rates ($\overline{R}$). It can be seen from these spectra, shown in Figure 1-4, that the spectral line shape is sensitive to the change in the rotational rates. This spectral sensitivity to spin label motion can be exploited to understand the dynamics of spin-labeled systems.

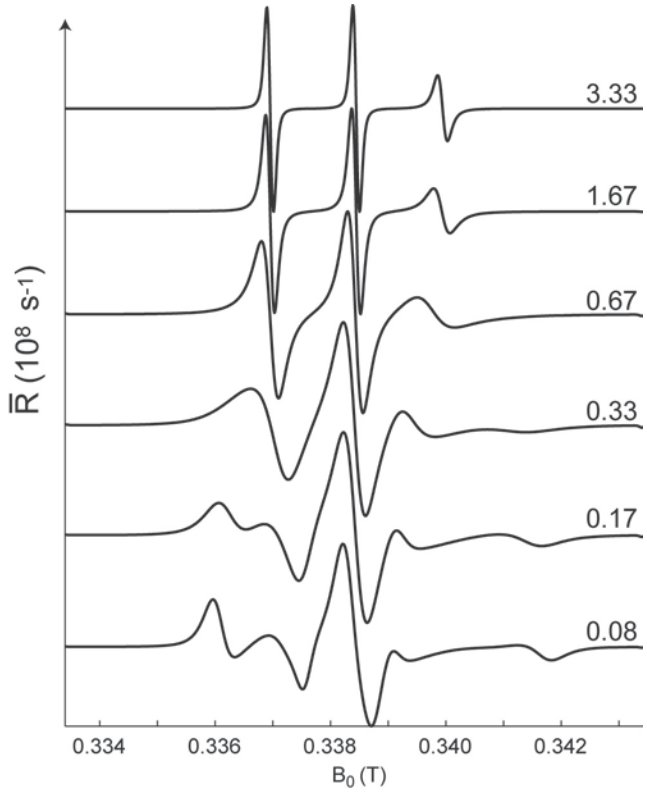

Figure 1-4. Nitroxide spectra were simulated using different rotational rates ($\bar{R}$) of the spin label to indicate the sensitivity of the spectra to spin label motion.

Analysis of the CW spectral line shape has proved to be an effective method to resolve the dynamics of spin-labeled biological systems.(*1, 4, 18, 25-28*) Quantitative parameters such as the inverse central line width (δ^{-1}) and the second moment ($\langle H^2 \rangle$) of the CW spectra provide insight into the mobility of the spin-labeled sites.(*4, 18, 21, 29*) However, to gain a deeper understanding of the system dynamics, fitting the CW spectra by simulation is needed.

Calculation of the ESR spectrum can be done using the stochastic Liouville equation (SLE). Based on the SLE, Freed and coworkers have developed models to calculate the spectrum of a spin label undergoing reorientational motions.(*14-16*) The first model considered here is the anisotropic Brownian diffusion model. In this model, rotational diffusion of the spin label is simulated as a series of infinitesimal reorientational steps. This rotational diffusion occurs about the axes of a rotational diffusion frame, which is fixed relative to the magnetic frame of the spin label. The anisotropic Brownian diffusion model would be applicable for describing the motions of a free spin label in a solution. Such a case is illustrated if Figure 1-5. Here the motion of the spin label with respect to the external magnetic field is modeled using the rotation of the spin label magnetic frame (orange) about the rotational diffusion axes (blue). The rotational rates of the spin label about the axes of the rotational diffusion frame can be defined using axial rotational diffusion parameters described by (*15*):

$$\begin{aligned} \overline{R} &= \sqrt[3]{R_{\perp}^2 R_{\parallel}} \\ N &= \frac{R_{\parallel}}{R_{\perp}} \end{aligned} \tag{1-6}$$

Here, $R_{\parallel}$ and $R_{\perp}$ are the axially symmetric rotational diffusion rate constants, $\overline{R}$ is the average rotational rate constant and N is the anisotropy parameter. Together these parameters describe the rotational motions of the spin label as well as the anisotropy of these motions. Another

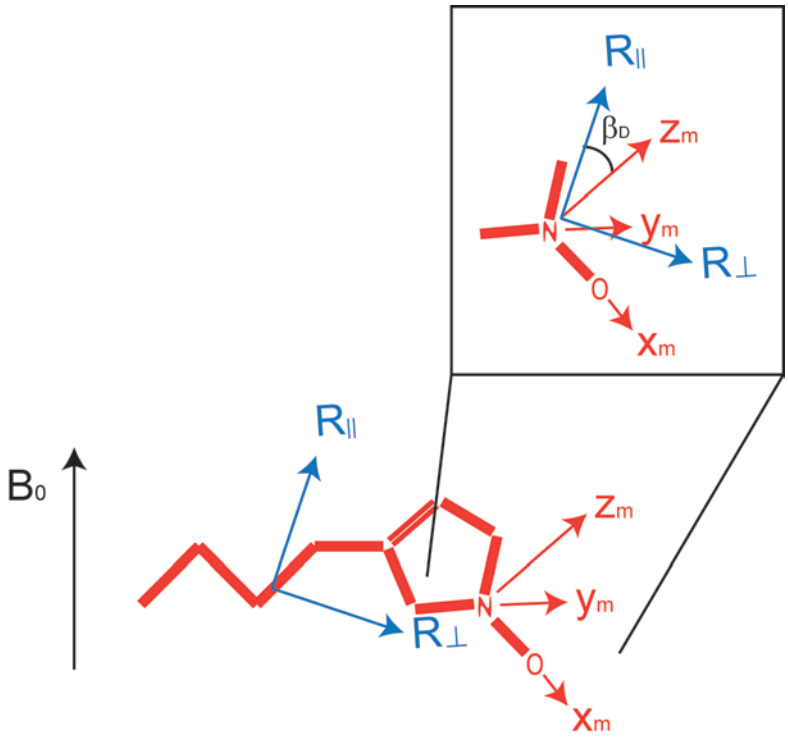

Figure 1-5. The Brownian diffusion model can be used to explain the rotational motions of a free spin label in solution. The magnetic frame of the spin label (x_m, y_m, z_m) defines the orientation of the g and A parameters (orange). The rotational diffusion frame describing the rotational motions of the spin label is defined by $R_{\|}$ and $R_{\perp}$ (blue). Inset: The transformation of the rotational diffusion frame into the magnetic frame is done using the Euler angle, β_D.

parameter that can be used to describe these motions is the rotational correlation time, τ, which can be defined as (*16*):

$$\tau = \frac{1}{6\bar{R}} \tag{1-7}$$

Lastly, three Euler angles are defined to transform the rotational diffusion frame into the spin label magnetic frame (α_D, β_D, γ_D). For axially symmetric rotational parameters only the β_D angle is typically needed.(*30-31*)

Another model that has been developed to describe the motions of the spin label is the microscopic order macroscopic disorder or MOMD model. In this model, the same rotational parameters are used as in the anisotropic Brownian diffusion model. However, an ordering potential is applied which constrains the spin label motion such that the spin label samples a restricted range of orientations. The MOMD model is well-suited for the simulation of a spin-labeled site on a protein. Here, the spin label can experience rotational motions as described in the anisotropic Brownian diffusion model. However, these motions may be restricted due to the local environment of the spin label, i.e. the protein backbone and local side chains.

The orientation of this potential can be described by a director axis (z_D) which is fixed relative to the protein. The ordering potential, U, is expressed by a series of spherical harmonics (*14*):

$$U(\theta,\phi) = \sum_{L,K} c_{LK} D_K^L(\theta,\phi) \tag{1-8}$$

where θ and ϕ are the Euler angles which specify the orientation of the director axis with respect to the rotational diffusion frame. c_{LK} represents the dimensionless potential energy coefficient for the harmonic function D_K^L. In most cases, the $D_0^2(\theta)$ term is sufficient to describe the spin label ordering potential and has the form:

$$D_0^2(\theta) = \frac{1}{2}(3\cos^2\theta - 1) \tag{1-9}$$

The effect of the ordering potential on the ESR spectrum is a distribution of spin label orientations produced by the potential which can be represented by the order parameter, S_{20}:

$$S_{20} = \left\langle D_0^2(\theta) \right\rangle = \left\langle \frac{1}{2}(3\cos^2\theta - 1) \right\rangle = \frac{\int_0^{2\pi} \exp[-U(\theta)/kT] D_0^2 d\theta}{\int_0^{2\pi} \exp[-U(\theta)/kT] d\theta} \tag{1-10}$$

Here, k is the Boltzmann constant and T is the temperature.

Figure 1-6 illustrates the use of the MOMD for a spin-labeled protein system. Here, the magnetic and rotational diffusion frames describing the rotational motion of a spin label located on a protein molecule are the same as in the anisotropic Brownian diffusion model (Figure 1-6, gray box). Also present, however, is the director axis (z_D), fixed relative to the protein, which describes the ordering potential. This ordering potential induces a *microscopic ordering* of the spin label with respect to the protein. However, in solution, the protein molecules, and hence their director axes, are randomly oriented with respect to the external magnetic field. This *macroscopic disorder* is implemented in the MOMD model by integrating over a distribution of director orientations. This disorder is illustrated at the top of Figure 1-6, where the protein molecules, and thus director axes, are randomly oriented with respect to the external magnetic field vector.

Lastly, the slowly relaxing local structure or SRLS model was developed to account for motion of the ordering potential on the ESR timescale.(*14, 32-33*) This effect can arise from motions which are slow on the ESR timescale such as backbone motions or the global tumbling of the protein. In both cases, the motions of the spin label are oriented in a local environment that is rotating on a longer timescale. Thus, the change in orientation of the ordering potential is

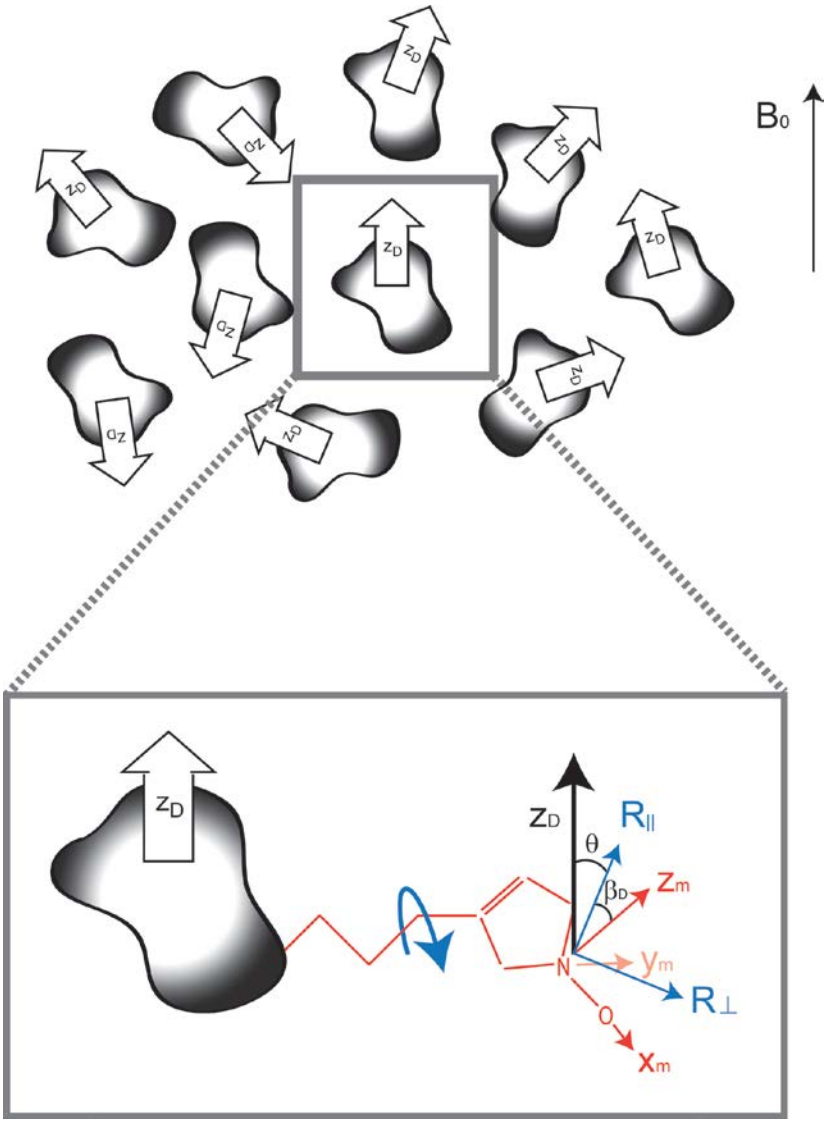

Figure 1-6. The MOMD model can describe the dynamics of a spin label attached to a protein molecule. Here the rotational dynamics of the spin label are modeled in the same way as for the anisotropic Brownian diffusion model, however, an ordering potential is implemented. The director axis, z_D, is defined relative to the protein and describes the ordering potential which restricts the spin label motion. Although the spin label is microscopically ordered, the protein molecules are randomly distributed in solution (macroscopically disordered).

accounted for in the SRLS model. The reorientational rate of the ordering potential is described using additional rotational diffusion parameters $R_{\|}^{c}$ and $R_{\perp}^{c}$ (illustrated in Figure 1-7). Multifrequency data is advantageous as it can resolve these different motional modes of a spin-labeled protein. Thus, SRSL is ideal for modeling multifrequency data.(*30, 32, 34-35*)

1.2.3 Spin Label Dynamics at High Frequencies

Although the majority of analyses using CW-ESR to probe dynamics have been done at 9 GHz, more work is being done at higher frequencies, such as 95 GHz. The advantage of performing simulations at higher frequencies is that faster motions can be probed. In particular, the anisotropic motions of the spin label can be resolved.(*28-29, 36*) More recently, multifrequency analyses have been performed to further enhance the amount of information that can be gained.(*32, 35, 37-41*) Multifrequency ESR is advantageous because motions at different timescales can be investigated.(*34*)

At higher frequencies, the hyperfine splitting values will not change; however, the magnetic field positions will shift. This can be understood using the following equation (*29*):

$$\Delta B = \frac{h\nu}{\beta_e}\left(\frac{1}{g_1} - \frac{1}{g_2}\right) \tag{1-5}$$

where ΔB represents the magnetic field separation between ESR signals from two g-values (g_1 and g_2). This equation illustrates that as the magnetic field of the CW spectrum increases, the splitting between the g-values increases as well. Thus, at 95 GHz, the anisotropy of the g-values can be resolved as shown in the nitroxide powder spectrum in Figure 1-8A. As a comparison, the nitroxide powder spectrum at 9 GHz is also shown (dashed).

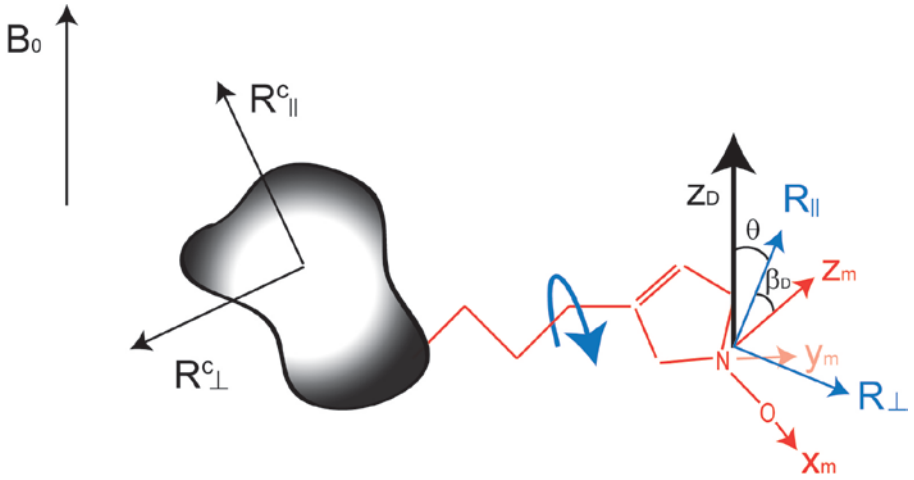

Figure 1-7. In the SRLS model, two additional rotational diffusion axes ($R_{\parallel}^{c}$ and $R_{\perp}^{c}$) are defined to describe the motion of the ordering potential.

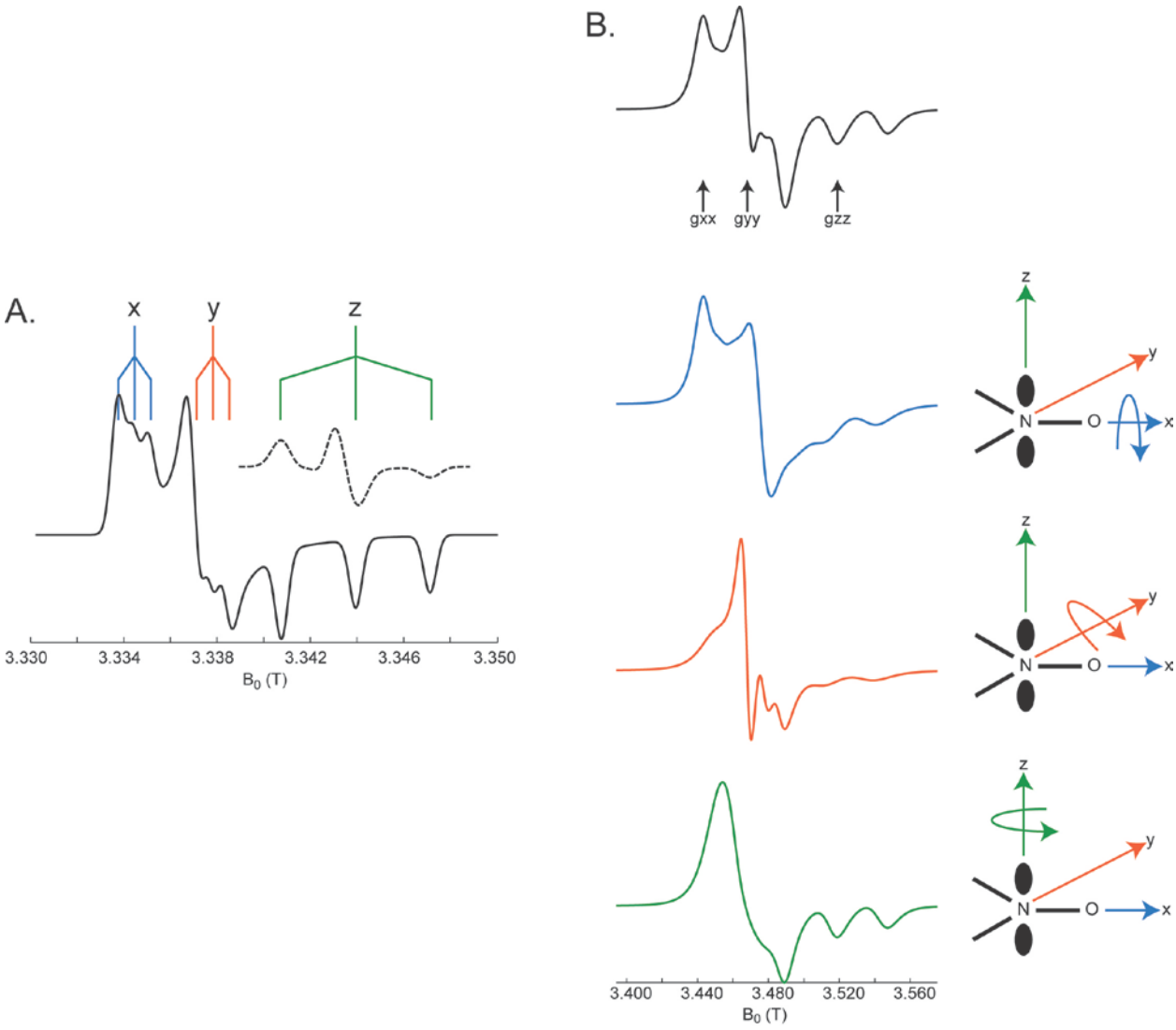

Figure 1-8. A. At higher frequencies (95 GHz) the orientational g-values are resolved as well as the hyperfine splitting. The 9 GHz nitroxide powder spectrum is also shown (dashed) for comparison. B. Three spectra were simulated to illustrate the sensitivity of the higher frequencies to the orientational motions of the spin label. The black spectrum represents an isotropic rotational rate that is slow along all three magnetic axes. However, if the rate is fast along just one of the axes, that orientation is more resolved in the spectrum. This is shown for faster rotational rates around the x (blue), y (orange), and z (green) magnetic axes of the g-tensor.

In addition to enhanced orientational resolution, 95 GHz CW-ESR are more sensitive to the anisotropic rotational diffusion about the magnetic axes of the spin label.(*29*) Such an effect is illustrated in Figure 1-8B where the spectra are simulated for several rotational diffusion conditions. The first spectrum (black) is simulated using slow rotational rates for all three magnetic axes. However, if the rotational rates are anisotropic, different orientational components of the spectrum will be resolved. For example, the blue spectrum in Figure 1-8B was simulated using a rotation rate along the x magnetic axis that is 5 times faster than the rates along the y and z axes. Therefore, because the rotational rate about the x-axis is fast, the y and z features of the spectrum are averaged out, but the x component is not. Similar cases can be made for fast rotational rates about the y and z axes as well.(*29*) This effect provides increased sensitivity to the rotational dynamics of the spin label at high frequencies.

1.3 THE DIPOLAR INTERACTION AND DISTANCE MEASUREMENTS

Several ESR methods have been developed to extract the distance between two or more coupled electron spins.(*13, 42*) The methods employed include continuous wave (*43-46*) as well as pulsed experiments, such as the double electron-electron resonance (DEER) (*5-6, 8, 47*) or the double quantum coherence (DQC) (*48-51*) experiments. Additionally, relaxation-based pulse techniques, such as inversion and saturation recovery experiments, can be used to measure the distance between a spin pair.(*9-12*) In each of these techniques the distance-dependent dipolar interaction is measured between two spins. ESR distance measurements are advantageous because they provide structural constraints for biological systems which may not be amenable to other techniques such as NMR or X-ray crystallography.

The dipolar interaction between two electron spins can be expressed by the following Hamiltonian (*13*):

$$\hat{H}_{dipolar} = \frac{\mu_0}{4\pi\hbar} g_A g_B \beta_e^2 \left[\frac{(\hat{S}_A \cdot \hat{S}_B)}{r_{AB}^3} - \frac{3(\hat{S}_A \cdot \vec{r}_{AB})(\hat{S}_B \cdot \vec{r}_{AB})}{r_{AB}^5} \right] \tag{1-11}$$

Here μ_0 is the permeability of a vacuum, ħ is the reduced Planck constant, g_A and g_B represent the isotropic g-values of the A and B spins which are coupled, and β_e is the Bohr magneton. $\hat{S}_A$ and $\hat{S}_B$ are the electron spin angular momentum operators of the A and B spins, while $\vec{r}_{AB}$ is the interspin vector connecting them. The full dipolar interaction can be expanded out to six terms (*13*):

$$\begin{aligned}
A &= (3\cos^2\theta - 1)\hat{S}_{A,z}\hat{S}_{B,z} \\
B &= -\frac{1}{4}(3\cos^2\theta - 1)(\hat{S}_{A+}\hat{S}_{B-} + \hat{S}_{A-}\hat{S}_{B+}) \\
C &= -\frac{3}{2}\sin\theta\cos\theta e^{-i\phi}(\hat{S}_{A,z}\hat{S}_{B+} + \hat{S}_{A+}\hat{S}_{B,z}) \\
D &= -\frac{3}{2}\sin\theta\cos\theta e^{i\phi}(\hat{S}_{A,z}\hat{S}_{B-} + \hat{S}_{A-}\hat{S}_{B,z}) \\
E &= -\frac{3}{4}\sin^2\theta e^{-2i\phi}\hat{S}_{A+}\hat{S}_{B+} \\
F &= -\frac{3}{4}\sin^2\theta e^{2i\phi}\hat{S}_{A-}\hat{S}_{B-}
\end{aligned} \tag{1-12}$$

where θ represents the orientation of the interspin vector with respect to the external magnetic field and ϕ is the angle between the projection of the interspin vector on the x-y plane and the x-axis. Taken together, these terms describe the full dipolar interaction; however, different terms contribute to the measured dipolar signal depending on the experiment being performed.

The remainder of this section will focus on two pulsed distance measurement techniques that have been used in the systems investigated in this thesis.

1.3.1 Double Electron-Electron Resonance

The double electron-electron resonance (DEER) experiment is applicable to distances in the 15-80 Å range.(*13, 52-53*) Using DEER, distance measurements have been performed in soluble (*54-59*) and membrane proteins (*60-65*) as well as peptides and peptide aggregates.(*66-72*) The technique has also been extended to measuring distances in nucleotides, both DNA (*73-74*) and RNA.(*75-78*)

In the DEER experiment the dipolar interaction between the two unpaired electron spins is detected in the modulation of a spin echo at low temperatures. Term A from equation (1-12) dominates the dipolar interaction detected by the DEER experiment. All other terms from equation (1-12) are negligible. Thus, the dipolar Hamiltonian for the DEER experiment can be written as:

$$\hat{H}_{dipolar} = \frac{\mu_0}{4\pi\hbar r_{AB}^3} g_A g_B \beta_e^2 \hat{S}_{A,z} \hat{S}_{B,z} (3\cos^2\theta - 1) \qquad (1\text{-}13)$$

where θ represents the orientation of the interspin vector with respect to the external magnetic field. Due to the anisotropy of g and A as well as the flexibility of the spin label, all θ angles are typically excited.

In the DEER experiment, pulses are applied at two different frequencies to probe the dipolar interaction between the coupled electron spins. A nitroxide echo-detected spectrum is shown in Figure 1-9. Here the location of excitation and designation of the spins are illustrated. The observer frequency is used to excite the A spins which are detected throughout the experiment (blue). The pump frequency which is applied ~70 MHz away from the observer spins is used to excite the B spins (red).

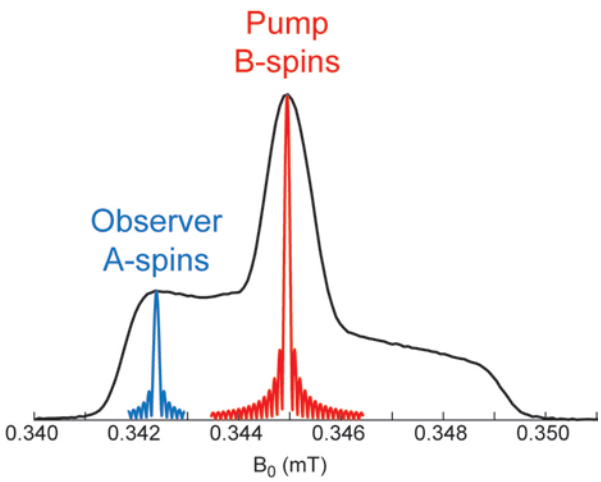

Figure 1-9. Echo-detected spectrum of a nitroxide spin label. The positions of the two spin packets which are excited in the DEER experiment are highlighted.

The pulse sequence for the 4-pulse DEER experiment is illustrated in Figure 1-10A. Here it can be seen that one pulse sequence is applied at the observer frequency, affecting the A spins, and one which affects the B (pump) spins. The spin diagram (Figure 1-10B) illustrates the behavior of the A and B spins as the pulse sequence is carried out. At the end of the observer sequence, a refocused echo is formed by the A spins. The time at which this echo occurs does not change throughout the experiment. The pump pulse at time t_p flips the B spins 180°. This inverts the dipolar interaction between the A and B spins, changing the Larmor frequency of the A spins. This change in the Larmor frequency causes the refocused echo to be off by a phase, φ, relative to the detector axis (y-axis Figure 1-10B). The phase at the end of the experiment can be calculated as shown in Figure 1-10C, leading to the signal (*79*):

$$V(t_p) = \cos(\omega_{AB} t_p) \tag{1-14}$$

where t_p is the time point at which the pump pulse is applied and ω_{AB} is the angular frequency of the dipolar interaction which can be defined as:

$$\omega_{AB} = \frac{\mu_0 g_A g_B \beta_e^2}{4\pi\hbar r_{AB}^3}(3\cos^2\theta - 1) \tag{1-15}$$

As the pump pulse is stepped out (t_p changes) the phase will change. This modulates the refocused echo with a frequency that is proportional to the dipolar frequency of the coupled A and B spins. For each orientation the contribution to the echo amplitude as a function of time can be expressed as (*79*):

$$V(t_p, \theta, r) = 1 - \lambda_B(1 - \cos(\omega_{AB} t_p)) \tag{1-16}$$

where λ_B is the fraction of B spins that are excited by the pump pulse, i.e. the fraction of spins that perturb the A spins. In a powder sample, all orientations are spanned. Therefore, averaged over all orientations, the echo signal can be expressed as (*79*):

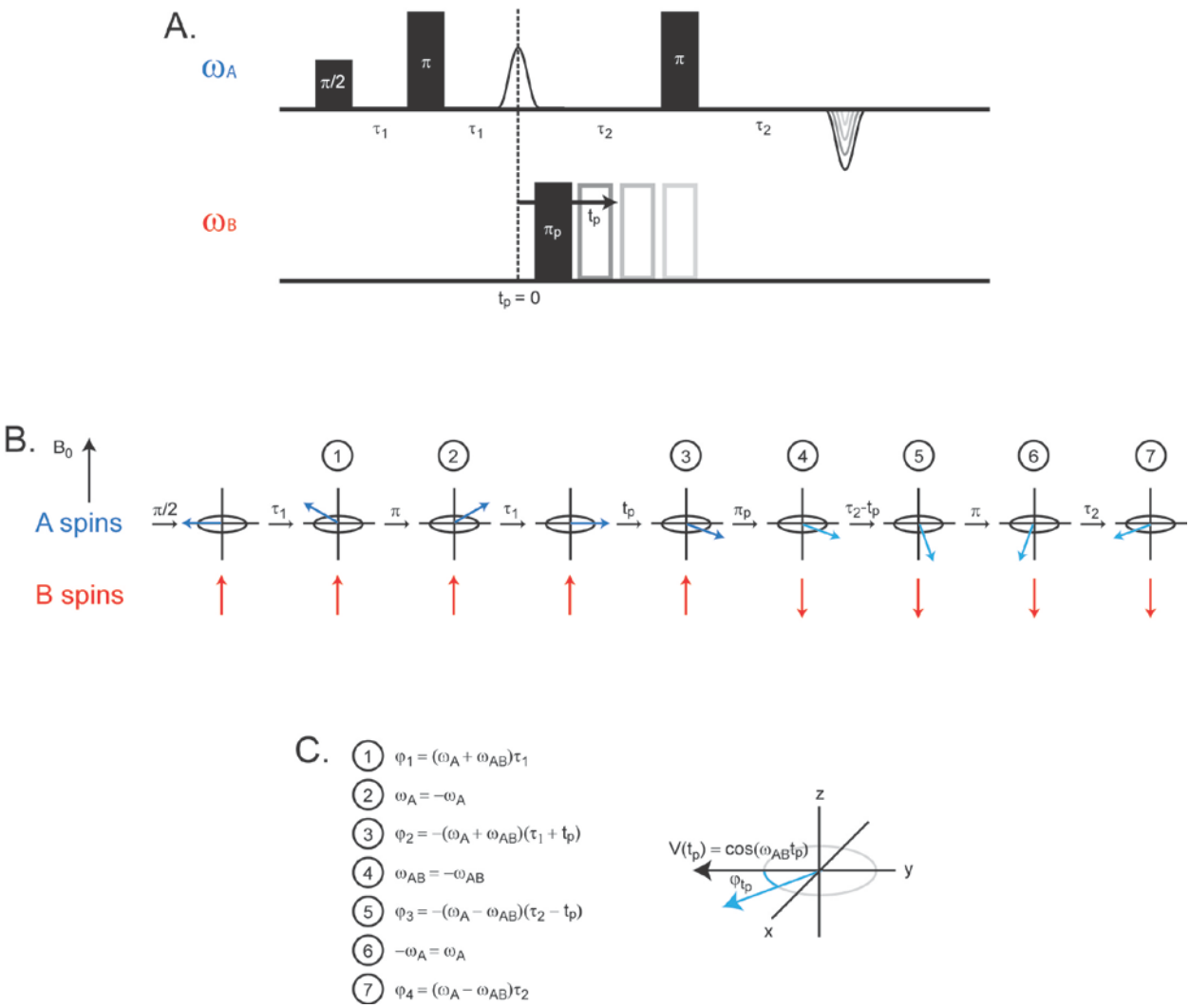

Figure 1-10. A. The pulse sequence for the 4-pulse DEER experiment. As the experiment is carried out, the pump pulse (π_p) is stepped out. B. The spin diagram for the precession of the spin system throughout the DEER experiment. The change in the Larmor frequency of the A spins is shown by different shades of blue. C. Using the spin diagram in B. the phase at the end of the DEER experiment can be determined by calculating the phases of the spin system throughout the DEER sequence, the final phase at the end of the experiment is also illustrated.

$$V(t_p, r) = 1 - \lambda_B \left[1 - \int_0^1 \cos\left(\frac{\mu_0 g_A g_B \beta_e^2}{4\pi\hbar r_{AB}^3}(3\cos^2\theta - 1)t_p\right) d\cos\theta \right] \quad (1\text{-}17)$$

Until now, the DEER signal has been expressed in terms of a single distance, r. However, in reality, a distribution of distances, P(r), is measured by the DEER experiment. Thus, the DEER signal can be expressed as:

$$V(t_p) = \int_{r_{AB,\min}}^{r_{AB,\max}} P(r) V(t_p, r) dr_{AB} \quad (1\text{-}18)$$

Equation (1-18) is a Fredholm equation of the first kind where $V(t_p,r)$ is the kernel and P(r) is the unknown function to be solved for.(*80*) Tikhonov regularization is used to effectively solve for P(r) from the time domain data. This is done by minimizing a function that describes the smoothness and mean square deviation of the fit to the time domain signal. Using an L-curve criterion, the optimal smoothness and mean square deviation for a successful fit to the data can be achieved.

In addition to the Tikhonov regularization technique, the time domain signal can be fit using a simple model such as a Gaussian distribution. In this case the model is simply fit to the data using the average distance, r, and standard deviation, $\sigma(r)$. In the case of a bimodal distribution the data can be fit using two average distances, r_1 and r_2, and two standard deviations, $\sigma(r_1)$ and $\sigma(r_2)$, as well as a population parameter, p_1.(*80*)

Ideally the DEER experiment is used to probe the distance between two coupled spins within a molecule, or the *intramolecular* distance. However, DEER is not a single molecule experiment, therefore the surrounding molecules create a range of spins which are coupled and thus contribute to what is known as the *intermolecular* signal. This is illustrated in Figure 1-11

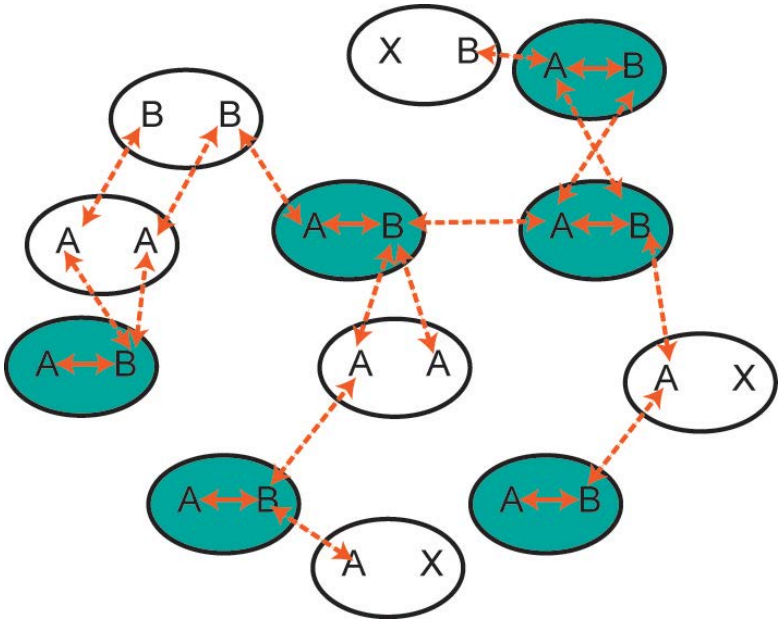

Figure 1-11. The dipolar coupling of interest is manifested in the intramolecular interactions, i.e. interactions between an A and a B spin present in the same molecule (green). All other interactions between A and B spins in different molecules are considered intermolecular interactions. Spins which are not A or B spins are designated with an X to illustrate that other spin packets are still present in the nitroxide spectrum.

where a distribution of molecules are represented as circles, each with two spin-labeled sites. Each spin-labeled site is designated with a letter which represents a spin packet (a group of spins with the same resonance frequency) in the nitroxide spectrum. A and B represent the spin packets which are excited by the ω_A and ω_B frequencies of the DEER experiment, respectively. All the other spin packets which make up the nitroxide spectrum, but are not excited in the DEER experiment, are designated with an X. The intramolecular interaction exists only in the molecules which possess an A and a B spin within one molecule (green, with a dipolar interaction indicated by a solid orange line). All the other dipolar interactions between the A and B spins contribute to the intermolecular interaction (white, with a dipolar interaction indicated by a dashed line). Thus, the time domain signal for the DEER experiment is a product of the intra and intermolecular interactions (*53*):

$$V(t) = V_{\text{intra}}(t)V_{\text{inter}}(t) \tag{1-19}$$

Due to the large range of distances that make up the intermolecular signal, $V_{inter}(t)$ is an exponential decay that depends on the spin concentration (C) as well as fraction of B spins excited by the pump pulse (λ_B). It can be represented by the following equation (*47*):

$$V_{\text{inter}}(t) = \exp(-kC\lambda_B t) \tag{1-20}$$

in which:

$$k = \frac{8\pi^2}{9\sqrt{3}} \frac{g_A g_B \beta_e^2}{\hbar} \tag{1-21}$$

The $V_{intra}(t)$ signal, is represented by equation (1-17). To obtain just the $V_{intra}(t)$ signal, the raw DEER data is fit to a background decay [i.e. $V_{inter}(t)$] which is subsequently divided out. This process is illustrated in Figure 1-12 where $V_{inter}(t)$ is represented by a red line.

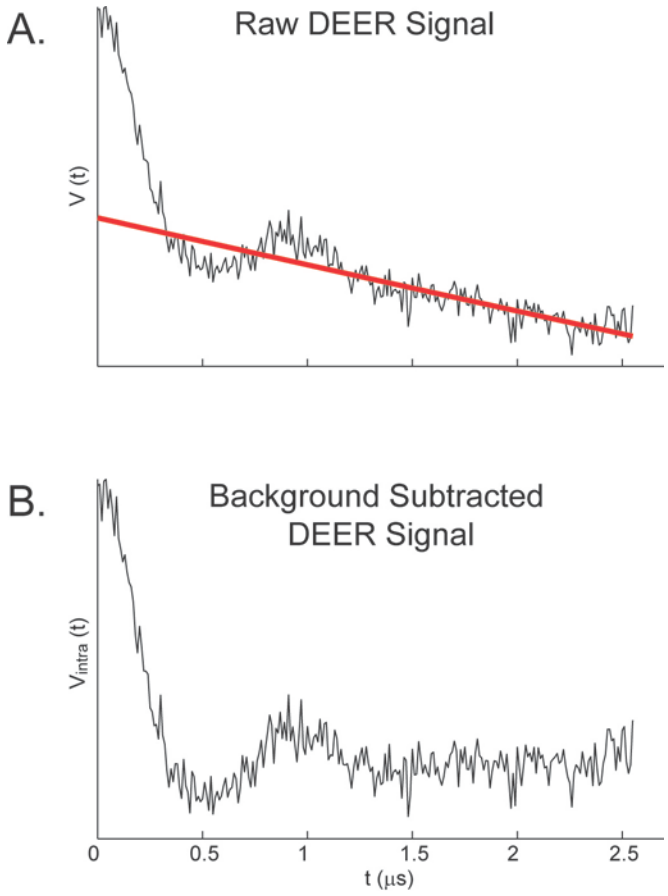

Figure 1-12. DEER time domain signals for the A. raw and B. background subtracted data. $V_{inter}(t)$ is represented by the red line.(*54*)

1.3.2 Saturation Recovery

In addition to the DEER experiment, relaxation mechanisms can be exploited to measure the dipolar interaction, and hence distance, between a paramagnetic metal and spin label. In these experiments, the relaxation rate of the slower relaxing spin (spin label) is enhanced by the faster relaxing spin (metal) to which it is coupled. Relaxation-based experiments, such as saturation recovery can be used for measuring distances in the 15-40 Å distance range.(*13*) Like the DEER experiment, saturation recovery is echo-based and performed at low temperatures. In the past several years, saturation recovery experiments have been primarily used to measure distances in Fe-containing systems.(*81-85*)

The average distance, r, between a fast and slowly-relaxing spin can be determined using the Bloembergen theory as modified by Kulikov and Likhtenshtein (*9-13*):

$$\begin{aligned}
\frac{1}{T_{1s}} &= \frac{1}{T_{1s}^{0}} + \frac{S(S+1)g_s g_f \beta_e^4}{\hbar^2 r^6}\left[\frac{1}{6}B + 3C + \frac{3}{2}E\right] \\
B &= \frac{T_{2f}}{1+(\omega_s-\omega_f)^2 T_{2f}^2}(3\cos^2\theta - 1)^2 \\
C &= \frac{T_{1f}}{1+\omega_s^2 T_{1f}^2}\sin^2\theta\cos^2\theta \\
E &= \frac{T_{2f}}{1+(\omega_s+\omega_f)^2 T_{2f}^2}\sin^4\theta
\end{aligned} \qquad (1\text{-}18)$$

where r is the average metal-nitroxide interspin distance, and f and s represent the metal and nitroxide electron spins, respectively. T_{1s} and T_{1s}^{0} represent the nitroxide longitudinal relaxation in the presence and absence of the metal, respectively. The parameters T_{1f} and T_{2f} are the longitudinal and transverse relaxation rates of the metal electron spin. g_f and g_s represent the metal and nitroxide electron spin isotropic g-values. The resonant frequencies for the metal and

nitroxide are represented by ω_f and ω_s. Finally, β_e is the Bohr magneton, $\hbar$ is the reduced Planck constant and θ is the angle between the interspin vector and the external magnetic field. The B, C, and E equations are related to the B, C, and E terms in the full dipolar equation.(*13*) Using this equation, the average distance between the two spins can be determined. However, as can be seen in equation (1-18), the average distance goes as r^{-6}. Therefore, the distance measurements performed using the relaxation theory may be biased to shorter distances.

The pulse sequence for the saturation recovery experiment is shown in Figure 1-13A. Here a picket-fence sequence is used where a series of $\pi/2$ pulses are applied to saturate the spin system. After saturation, an echo-detection pulse sequence is applied ($\pi/2$-τ_2-π-τ_2). As this detection sequence is stepped out over the time of the experiment, the echo amplitude will increase at a rate which is proportional to the T_1 or longitudinal relaxation of the spin. An example of such a recovery curve is shown in Figure 1-13B. Fitting of this curve to a single or biexponential function provides the relevant T_1 values.

Using the saturation recovery experiment and equation (1-18), the average metal-nitroxide distance is determined. This is done by measuring the T_{1f} and T_{2f} values of the metal as well as the T_1 of the nitroxide in the presence (T_{1s}) and absence (T_{1s}^0) of the metal. As in the DEER experiment, the signal is averaged over all orientations of θ due to the distribution of the spin label.

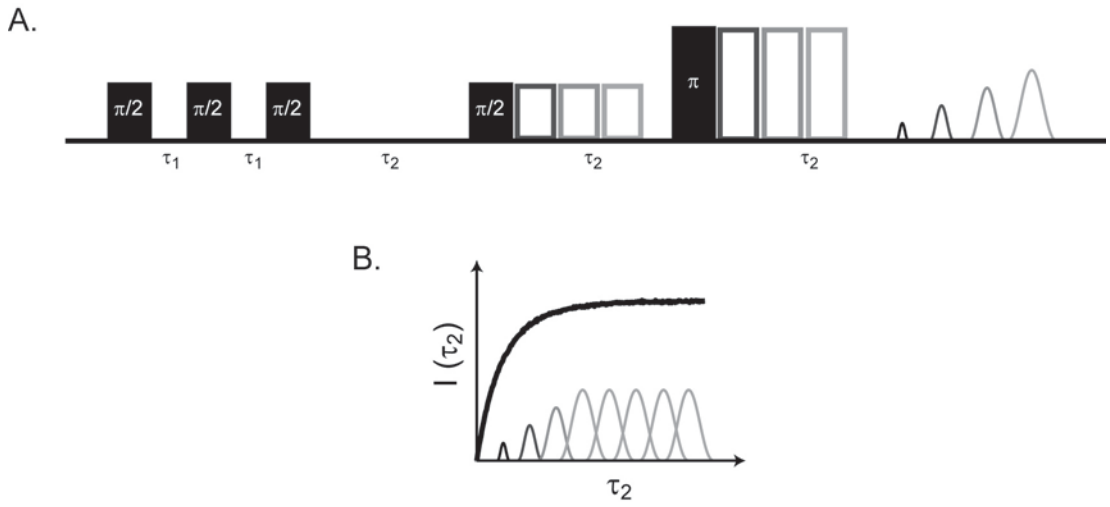

Figure 1-13. Saturation recovery A. pulse sequence and B. signal.

2.0 SIMULATING THE DYNAMICS AND ORIENTATIONS OF SPIN-LABELED SIDE CHAINS IN A PROTEIN-DNA COMPLEX

2.1 ABSTRACT

Site-directed spin labeling, wherein a nitroxide side chain is introduced into a protein at a selected mutant site, is increasingly employed to investigate biological systems by electron spin resonance (ESR) spectroscopy. An understanding of the packing and dynamics of the spin label is needed to extract the biologically relevant information about the macromolecule from ESR measurements. In this work, molecular dynamics (MD) simulations were performed on the spin-labeled restriction endonuclease, EcoRI in complex with DNA. Mutants of this homodimeric enzyme were previously constructed and distance measurements were performed using the double electron-electron resonance experiment. These correlated distance constraints have been leveraged with MD simulations to learn about side chain packing and preferred conformers of the spin label on sites in an α-helix and a β-strand. We found three dihedral angles of the spin label side chain to be most sensitive to the secondary structure where the spin label was located. Conformers sampled by the spin label differed between secondary structures as well. C_α-C_α distance distributions were constructed and used to extract details about the protein backbone mobility at the two spin-labeled sites. These simulation studies enhance our understanding of the

behavior of spin labels in proteins and thus expand the ability of ESR spectroscopy to contribute to knowledge of protein structure and dynamics.

2.2 INTRODUCTION

Site-directed spin labeling (SDSL) for electron spin resonance (ESR) spectroscopy has now become a widely utilized method to obtain structural constraints, probe conformational changes, and monitor protein-protein and protein-ligand interactions.(*1, 4*) In such experiments the presence of the spin label contributes substantially to the experimental observables. The inherent mobility of the spin label side chain contributes to the dynamics measured in the continuous wave (CW) spectral line shape. Furthermore, the length of the spin label adds to the distance constraints that are measured most commonly using the pulsed double electron-electron resonance (DEER) experiment.(*5, 86*) Ultimately, the position and mobility of the *backbone* are sought when performing ESR distance and dynamics measurements on biological systems or nanostructures. For this reason, work has progressed towards deconvoluting the backbone and spin label effects on such measurements through experiment and simulation.

The DEER experiment has been utilized to probe the flexibility and orientations of terminally spin-labeled oligomers [bis-peptides or oligo(para-phenyleneethynylene)s] by analysis of orientational effects (*87*) and distance distribution functions.(*67*) Molecular models have also been developed to more accurately extract backbone details of these oligomers.(*66, 68-69*) In these models, parameters describing the orientation and flexibility of each segment with respect to subsequent segments of the oligomer were optimized such that the simulated distance distributions agreed with experiment. From these studies, end-to-end distance distributions from

the oligomer backbone could be extracted, providing insight into the shape and flexibilities of these structures.

To resolve the backbone details for larger systems, such as peptides and proteins, a systematic understanding of the spin label conformation and packing as well as dynamics is needed. The behavior of the spin label has been probed in various systems by a number of methods, including X-ray crystallography (*88-95*), *ab initio* calculation (*96-98*), rotamer libraries (*63, 99-100*) as well as molecular dynamics (MD) (*101-108*) and Monte Carlo simulations.(*109-112*) Using X-ray crystallography, Hubbell and coworkers determined preferred conformations of the spin label side chain at solvent accessible helical and loop sites in T4 lysozyme.(*89-90, 92*) The spin label conformation can be defined by five dihedral angles (χ_1-χ_5) along the length of the spin label side chain. These angles are represented on the spin label in Figure 2-1. These analyses suggest that for solvent-accessible, non-interacting spin-labeled sites, the internal motion of the spin label results primarily from the rotations about the terminal dihedral angles (χ_4 and χ_5), known as the χ_4/χ_5 model. At such sites, local interactions with the backbone atoms and disulfide group of the spin label restrained the side chain such that the [χ_1, χ_2] and occasionally the disulfide bond conformations (χ_3) could be resolved. On the other hand, the nitroxide ring was rarely resolved indicating that the χ_4 and χ_5 angles were highly unconstrained. These structures, taken together with CW-ESR data (*21, 25*), led to the formulation of the χ_4/χ_5 model. At sites where the spin label is involved in interactions with neighboring groups, fully resolved crystal structures of the entire nitroxide side chain were possible.(*88, 91, 94*)

Freed and coworkers (*96*) used the Hartree-Fock theory to calculate torsional profiles of the five defining dihedral angles of the spin label using fragments of the spin label side chain.

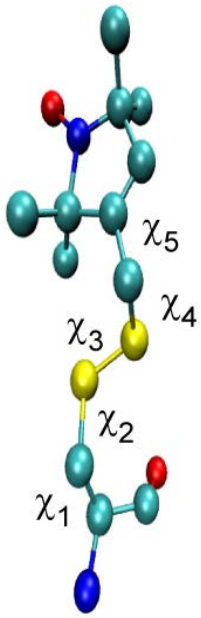

Figure 2-1. Methanethiosulfonate (MTS) spin label structure with the five defining dihedral angles, χ_1-χ_5.

Using the minima values from the torsional profiles, as well as steric constraints, 18 possible conformers of the spin label on a polyalanine α-helix were identified. Along these same lines, Hubbell and coworkers (*97*) recently utilized density functional theory (DFT) to calculate the lowest energy conformations (χ_1-χ_3) of the spin label on a peptide fragment. The conformers were then modeled on a polyglycine to identify the interactions that stabilize the conformers in a helical environment. This work differed from that of Freed and coworkers due to the inclusion of backbone atoms in the calculations. This enabled the observation of interactions between the S_δ of the spin label and backbone atoms of the peptide fragment.

Alternatively, several groups have utilized MD simulations to model spin-labeled systems comparing the simulated results to experimental CW (*101-105*) or DEER (*106-108*) results. One of the largest challenges in performing MD simulations to model the side chain conformation and dynamics is sufficient sampling. Different techniques have been employed to overcome this problem such as performing the simulations at high temperatures (*102, 107*) or in implicit solvent.(*109*) Such conditions, however, can be misrepresentative of the experimental conditions to which the simulations are compared. It has been shown by others that in order to effectively model the spin label, simulations must be performed for long timescales.(*98, 105-106*) For example, Roux and coworkers parameterized the MTS spin label and performed long MD simulations (101 ns) using 18 different starting orientations of the spin label on a polyalanine α-helix.(*98*)

As another means to ensure sufficient sampling of the spin label conformer space, Fajer and coworkers developed a Monte Carlo rotamer search technique.(*110-111*) The rotamer search used the Metropolis criterion to identify the lowest energy conformers at the spin-labeled site.(*113*) Subsequent MD simulations, using the lowest energy conformers as starting

orientations of the spin label, enabled sampling of rotamer minima in the potential energy landscape of the spin-labeled system.(*105*) This technique was subsequently expanded using a simulated scaling approach to enhance the conformational sampling of the spin label during the MD production run.(*114*) In this method the molecular dynamics trajectory is coupled to a potential scaling parameter. A walk through the potential scaling parameter space weights the potential energy surface of the spin-labeled region. In this way the potential energy barriers of different spin-labeled conformations could be crossed, enhancing the spin label sampling during the MD simulation.(*111*)

Significant insight has been gained on the preferred conformations and dynamics of the spin label from these studies. However, the majority of the in-depth analysis has been performed on spin-labeled α-helical structures. There exists less information on the behavior of the spin label on other secondary structures such as a β-strand or loop region. Using the cellular retinol-binding protein (CRBP), Hubbell and coworkers performed a thorough analysis of the spin label present on β-strands.(*31*) The dynamics of the spin label on interior and edge strands were investigated using CW-ESR. Allowed conformations of the spin label were derived from spectral analysis and a manual variation of the spin label side chain, which was built into the crystal structure of CRBP at the various spin-labeled sites. In addition, a recent crystal structure of the spin-labeled β-barrel membrane protein, BtuB, was published by Freed *et al.* which resolved the orientation of spin labels present on β-strands of the barrel in or adjacent to the lipid bilayer.(*95*) Furthermore, MD simulations of the spin label on β-strands have been used in conjunction with distance constraints to model protein structures through simulated annealing routines.(*59, 115-116*) However, a detailed analysis of the preferred spin label conformers was

not provided. Although these works provide initial insight, more analyses are required to further our understanding of the behavior of the spin label on β-strands.

Adding to the current understanding of the spin label conformers and dynamics may lead to general rules of packing that may enhance the ability to extract information about protein structure and function from ESR measurements. We can augment this knowledge by performing simulations on a spin-labeled protein that has been investigated experimentally. Accordingly, MD simulations were performed, and compared to experiment, to model the nitroxide spin label located on three different secondary structures of the spin-labeled EcoRI-DNA complex: 131 (loop), 180 (β-strand) and 249 (α-helix).

EcoRI is a 62 kDa homodimer restriction endonuclease that binds to and cleaves a specific six base pair sequence GAATTC in DNA. The crystal structure of the specific complex of EcoRI has been determined and many thermodynamic and kinetic studies have been done to understand the extreme binding specificity of this enzyme. For instance, EcoRI binds with an affinity of up to 96,000-fold greater to its specific sequence than to a sequence that differs by one base pair.(*117-118*) The structure of EcoRI consists of a large, stable main domain and two arms (inner and outer) that enfold the DNA.(*119-120*) These arms are highlighted in Figure 2-2 in blue (inner) and red (outer), the main domain and DNA are silver. This arm region is believed to play a role in the binding specificity of EcoRI due to key contacts made between the arms and the DNA backbone.(*118, 121*) To shed light on this region, structural constraints were obtained by performing several distance measurements using the DEER experiment on the specific EcoRI-DNA complex.(*54*) In this work we have leveraged these correlated distance constraints with MD simulations to learn about side chain packing and dynamics of the spin label as well as backbone details at three different spin-labeled sites in the EcoRI-DNA complex.

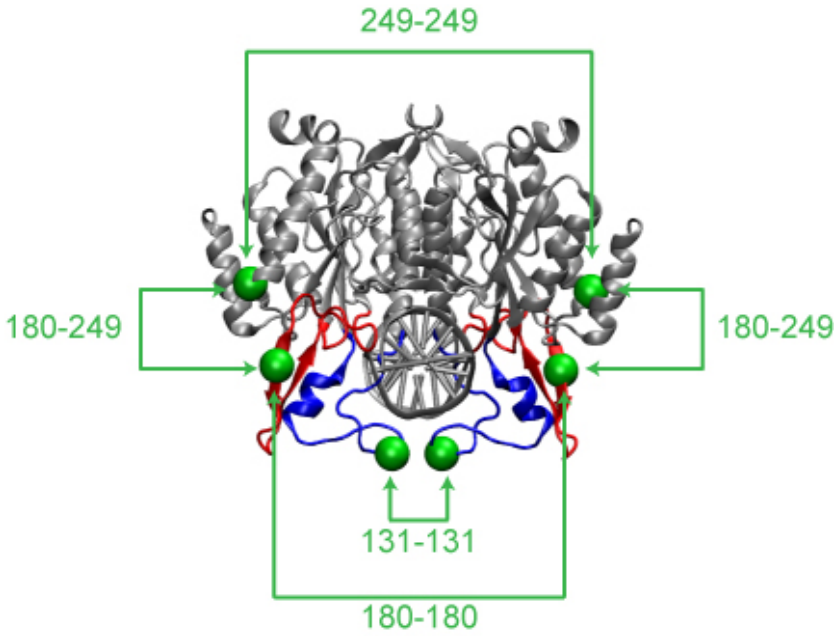

Figure 2-2. Crystal structure of the specific EcoRI-DNA complex (PDB 1CKQ) (*120*) with residues 131, 180 and 249 represented by green spheres. The distances measured experimentally are also shown by the arrowed brackets: 131-131, 180-180, 180-249 (*54*), and from this work 249-249.

2.3 METHODS

2.3.1 DEER Experiments

Distance measurements were previously published on the methanethiosulfonate spin-labeled (MTSSL) R131C (single), S180C (single) and S180C-K249C (double) mutant proteins in specific EcoRI-DNA complexes.(*54*) In the current study, the DEER experiment was performed on the MTSSL-K249C mutant protein using a Bruker EleXsys CW/FT X-band ESR spectrometer with the Bruker X-band ER-MD5 resonator. The MTSSL-K249C sample was prepared in 30% deuterated glycerol, 65% deuterated water, and 5% protonated water resulting in a final protein concentration of 180 μM. Appropriate salt concentrations (0.22 M) and pH as well as a 4:1 DNA:protein ratio was used to ensure that at least 99% of the sample existed as the protein-DNA complex.(*54*) The sample was flash frozen by plunging the capillary into liquid nitrogen cooled propane. The DEER experiment was performed at 40 K using an Oxford ITC 503 temperature controller and CF935 dynamic continuous flow cryostat. DEER experiments were performed using the four-pulse sequence: $(\pi/2)_{\upsilon 1}$-τ_1-$(\pi)_{\upsilon 1}$-T-$(\pi)_{\upsilon 2}$-τ_2-$(\pi)_{\upsilon 1}$-τ_2. The observer $(\pi/2)_{\upsilon 1}$ and $(\pi)_{\upsilon 1}$ pulses were 16 and 32 ns respectively, and the pump $(\pi)_{\upsilon 2}$ pulse was 32 ns. The pump pulse was located at the maximum of the nitroxide spectrum with the observer pulse applied at a frequency ~70 MHz higher. Deuteration of the solvent and glycerol resulted in a phase memory time of 2.5-3 μs, enabling the measurement of the long distance expected for the K249C mutant (C_α-C_α = 5.7 nm). A step size of 10 ns was used and the integrated echo intensity was collected for 512 points. A two-step phase cycling (+x, -x) was carried out on the first $\pi/2$ pulse. The pump pulse began 200 ns before the echo so that the zero time could accurately be determined. The data acquisition time was 75 hours.

2.3.2 MD Simulations

Sites 131, 180 and 249 on the crystal structure of the specific EcoRI-DNA complex (*119*-*120*) were mutated to nitroxide spin-labeled cysteines using the VMD program.(*122*) A Metropolis Monte Carlo minimization (MMCM) rotamer search was then performed in CHARMM (*123*) using the rotamer search program developed by Fajer *et al*.(*110*) Parameters describing the spin label force field were taken from the work of Sezer *et al*.(*98*) The CHARMM27 force field was used for the protein and DNA.(*124*) To ensure the full rotamer space of the spin label was accessed during the rotamer search, ten rotamer searches were performed starting with different initial orientations of the spin label. Each rotamer search was performed until ~1000-1500 conformers had been generated at each spin-labeled site. Ten of the lowest energy conformers were selected for each of the sites separately. Using these conformers, ten singly (131) and ten doubly labeled (180 and 249) specific EcoRI-DNA complexes were constructed for MD simulation.

All structures were solvated in an explicit water box and counter ions were added to neutralize the system and provide a salt concentration comparable to experiment ([NaCl] = 0.22 M). All MD simulations were performed using the NAMD program.(*125*) The structures were energy minimized using a conjugate gradient method. After heating the system to 300 K, the system was equilibrated for 1 ns in an NPT ensemble of 1 atm using a Langevin piston. During both the minimization and equilibration steps the protein backbone and DNA were restrained as well as the spin labels. Production runs were performed in an NVT ensemble for 30 ns using a 2 fs time step. Periodic boundary conditions were used and particle mesh Ewald summation was used to treat the electrostatic interactions. To ensure reliability in the simulated results, the last

20 ns of the simulation, where the protein backbone had fully equilibrated, were used for analysis. Visualizations were done using VMD.(*122*)

2.4 RESULTS AND DISCUSSION

2.4.1 EcoRI DEER Measurements

Distance measurements were previously published on the specific EcoRI-DNA complex to better understand the orientation and behavior of the arm region of this DNA-binding protein.(*54*) The EcoRI mutant proteins were generated as described previously (*126*) and spin-labeled at sites 131 (loop, inner arm), 180 (β-strand, outer arm) and 249 (α-helix, main domain). Due to the homodimeric nature of EcoRI, spin labeling of the protein with a single cysteine mutation results in two spin-labeled sites in the DNA-bound complex. The intermonomer (131-131, 180-180, and 249-249) and *intra*monomer (180-249) distances that were measured are overlaid on the crystal structure Figure 2-2 (green brackets). The distance measurements in the inner (131-131) and outer arms (180-180) were performed to observe changes in the arm region upon binding to different sequences of DNA. The outer arm to main domain *intra*monomer (180-249) distance measurement provides yet another point-to-point distance to better triangulate the location of the outer arm upon binding different sequences of DNA. In principle, multiple distances corresponding to the 180-180, 249-249, and 180-249 intermonomer distances could also be detected in the 180-249 double mutant. However, the C_α-C_α distances for these intermonomer constraints are on the order of 6.0 nm and a time domain of only 1.5 μs was collected, thus such long distances were not detected. The 180-180 and 180-249 distance measurements were

performed and published previously by Stone *et al*.(*54*) These distance constraints are augmented by the 249-249 intermonomer distance measured in this work. Site 249 resides in the main domain of EcoRI and has restricted motion. Thus the intersubunit distance between sites 249 was determined to serve as a reference for comparison to the distance information obtained for the arm region.

Both the 180-180 and 249-249 distance measurements were close to the upper limit of distances measurable by the DEER technique (C_α-C_α = 5.6 and 5.7 nm, respectively). Due to the low modulation frequency for such long distances, there is an inherent uncertainty in the background subtraction and subsequent fitting of the DEER data needed to extract distance distributions from the time domain data. Using the DeerAnalysis2009 (*127*) program, the previous fit to the 180-180 experimental data was refined. Both sets of data were fit using Gaussian distributions. The raw data and background fit for the 249-249 data is shown in Figure 2-3. The background correction was performed using the homogeneous background correction model. The background subtracted DEER time domain signal and corresponding distance distribution are shown in Figure 2-4. Unexpectedly, a bimodal distribution was observed for this distance measurement. A good L-curve could not be obtained using the Tikhonov regularization to fit the data, possibly due to the presence of the two long distances. A fit to two Gaussians was used instead to fit the time domain data and simulate the associated distance distribution. In this case successful fits to the time domain data could be achieved using an average distance of 7.1 and standard deviation of 0.14 nm.

Based on the C_α-C_α distance from the crystal structure of the specific EcoRI-DNA complex (5.7 nm), the longer distance acquired (7.1 nm) is reasonable taking into account the added length of the spin label. However, a shorter distance (5.1 nm), comprising ~40% of the

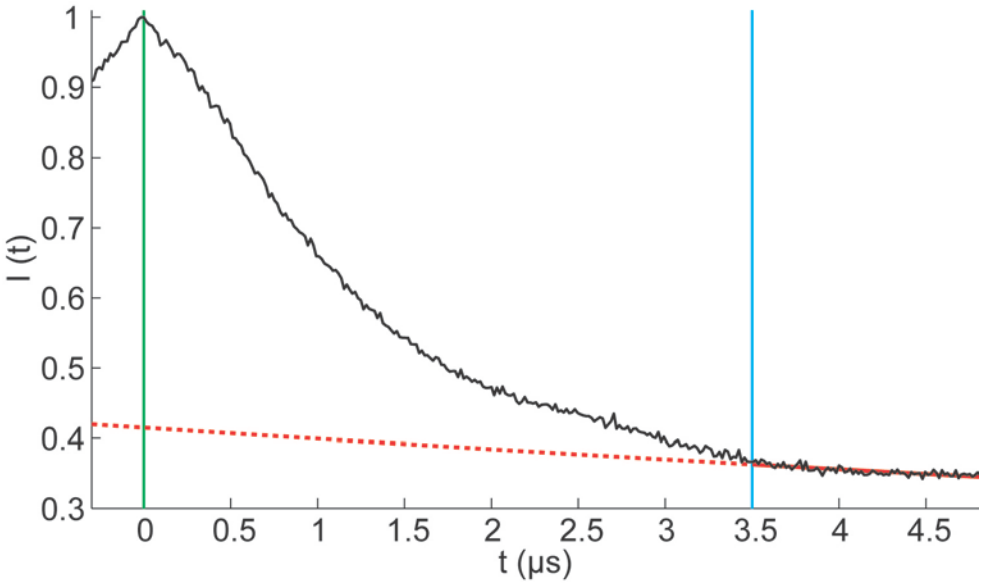

Figure 2-3. Raw 249-249 DEER data with background subtraction from DeerAnalysis2009 homogeneous background fitting. The green line indicates the zero time, the blue line indicates the starting time for the background fitting, and the red line is the background fit.

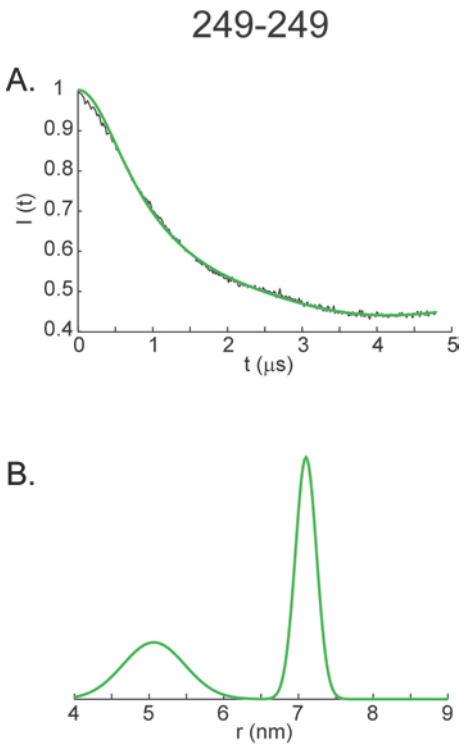

Figure 2-4. A. The background subtracted time domain signal for the 249-249 intermonomer distance measurement performed using the DEER experiment. B. The experimental distance distribution extracted from the time domain signal using DeerAnalysis2009.(*127*) The data was fit using two Gaussians.

distance distribution, was also observed. One reason for this bimodality could arise from different conformers sampled by the spin label resulting in two observed distances. Such an orientation of the spin label would be unlikely, however, as it would have to protrude into the protein to achieve such a distance. Additionally, two spin label conformers would likely result in a trimodal distribution due to the combination of the spin label conformations and the distances between them.

A second possibility is that oligomerization of the EcoRI complex occurs in solution, such that a second, shorter inter-complex distance of 5.1 nm would be detected in our experiments. Oligomerization of EcoRI into a trimer of dimers has been observed in the crystal structure of the complex. If such an oligomerization occurred in solution, it could position the 249 sites in close proximity such that a second, shorter, *inter*complex distance may be measured by experiment. Using the EcoRI crystal structure this trimer of dimers formation was modeled in Pymol. Six spin-labeled models of the trimer of dimers were constructed in VMD (*122*) using the six most populated conformers at site 249 from runs **i** and **ii**. Starting from the original crystal structure the nitroxide-nitroxide distance between the dimers was 2.3-3.5 nm, with an average from all six models of 2.8 nm (Figure 2-5, top). In solution, however, the orientation of the trimer of dimers would be more flexible, and the complex is likely to be less compact than in the crystal. By simply rotating the complexes by 20-30°, with respect to each other, the average intercomplex distance is 4.4-6.1 nm, depending on the spin label rotamer used (Figure 2-5, bottom). Thus, it is possible that if the trimer of dimers formed in solution, a slight change in the orientation of the complexes could result in a broad 5.1 nm distance as seen in the 249-249 DEER results. However, we do not know if oligomerization occurs in solution under these conditions, and we are currently testing this possibility experimentally.

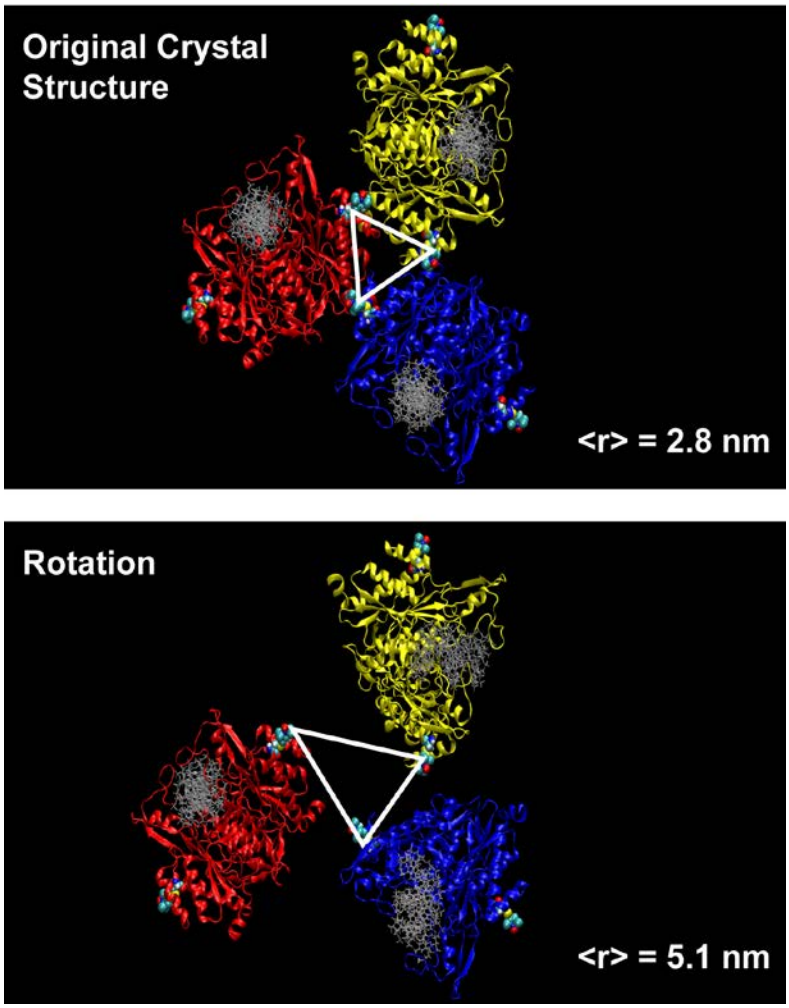

Figure 2-5. Models of the trimer of dimers formed by the EcoRI complexes (PDB 1CKQ).(*120*) Each of the complexes are highlighted in different colors with the DNA represented in silver. The spin labels at sites 249 are displayed in a VDW representation. The original crystal structure model (top) clearly shows the inter-dimer contacts that form the trimer of dimers. Rotation (bottom) of the complexes results in a larger intercomplex distance as can be seen in the white triangle highlighting the spin label – spin label distances.

The possibility of oligomerization occurring in solution is further supported by the fact that the 249-249 DEER signal possesses a larger modulation depth than expected (based on the theoretical modulation depth (*5*) and previous calibration experiments on a bilabeled peptide). This signifies a larger number of coupled spins than expected from just two spin-labeled 249 sites in the EcoRI-complex, suggesting that higher order oligomers may have formed in this sample. Indeed, the modulation depth (Δ) for the 249-249 results ($\Delta = 0.41$) is greater than that of the 180-180 results ($\Delta = 0.68$), even though the experiments were performed under similar conditions. Ultimately, the 7.1 nm distance was primarily considered when comparing the simulated and experimental distance distributions.

2.4.2 MD Simulated Distance Distributions

Although the DEER data provides structural constraints in the distances between the spin labels, the backbone C_α-C_α distances and distributions are more biologically relevant to understanding the backbone structure and dynamics of EcoRI. To this end, MD simulations were performed on the specific EcoRI-DNA complex to model the spin-labeled sites which were investigated experimentally: 131 (loop), 180 (β-strand), and 249 (α-helix). Ten independent runs with different starting spin label conformations were performed to effectively sample the spin label rotamer space and test for convergence of the individual structures to a common preferred conformer or conformers. To identify the relevant simulated data, distance distributions between the nitrogen atoms of the spin label were constructed from the MD trajectories and compared to those obtained from the DEER experiment. By using experimental results to validate the

simulations, they were not biased by experimental restraints which can perturb the simulated results.(*128*)

Distance distributions were constructed, from all 10 parallel runs, for each of the experimentally measured distances: 131-131 intermonomer, 180-180 intermonomer, 180-249 *intra*monomer, and 249-249 intermonomer, resulting in a total of 50 simulated distance distributions (two 180-249 *intra*monomer distances extracted from simulated results). MD runs, for which the simulated results reproduced those of the experiment, were used to draw conclusions about the backbone details of the specific EcoRI-DNA complex. Two criteria were used to compare the simulated and experimental results. First, agreement on the average distance and standard deviation of the experimental and simulated distance distributions was assessed. In the case of the 180-249 double mutant, agreement of all four distance distributions (180-180, 249-249, and *both* 180-249) with experiment was assessed simultaneously. The 180-249 *intra*monomer distance measurement was essential as it provides a correlation between the 180-180 and 249-249 experimental results. Because of this, the conformation of the spin label must be such that not only are the 180-180 and 249-249 distance distributions in agreement with experiment, but also the 180-249 in *both* monomers. Secondly, the local backbone root mean square deviations (RMSD) of the spin-labeled sites and ~30 surrounding residues were considered. The RMSD measures the magnitude of variation in the position of the backbone atoms from a reference point, in this case the backbone atom positions at the beginning of the 30 ns production run. Using this RMSD, the initial drift and eventual equilibration of the atom positions can be observed. Simulated results with RMSDs that are either high or continually increase throughout the simulation may depict artificial behavior of the system due to a lack of

equilibration or convergence near the spin-labeled site. Thus, only simulated results from stable, equilibrated runs were considered.

Although the simulated 131-131 distances were similar to experiment, the distributions were considerably broader. Therefore, although runs **i-vi** (Figure 2-6) possessed stable RMSD trajectories, they were still considered to be poor fits to the experimental 131 results. The remaining simulations (runs **vii-x**, Figure 2-7) possessed unstable RMSD trajectories, indicating a lack of system equilibration. Consequently, none of the simulations performed at the loop site 131 were used to extract backbone or conformer details. A possible reason for the discrepancy is that the dynamics of the loop region may be overestimated in the MD simulations, leading to a higher flexibility than is experimentally observed.

Of the 10 parallel simulations performed on the doubly labeled (180 and 249) system, two runs had excellent agreement with experiment (runs **i** and **ii**). In these runs, all four constraints (180-180, 249-249, and both 180-249) agreed with the respective experimental distance distributions and possessed stable local backbone RMSDs. The resultant distance distributions of these runs are presented in Figure 2-8 where the experimental distributions are shown in black and the simulated in red. In the case of the 180-249 *intra*monomer distance distributions two simulated results were measured, one within each monomer of the EcoRI-DNA complex. These are shown individually as solid or dashed red lines. The local backbone RMSD trajectories are also shown in gray for sites 180 and 249, respectively.

Two of the remaining 8 runs possessed unstable RMSDs even after 30 ns of simulation (runs **iii** and **iv**, Figure 2-9). Of the remaining 6 runs (runs **v-x**, Figure 2-10), the RMSDs were stable, however, only two or three of the simulated distributions agreed with experiment. Run **v** shows this partial agreement between the simulated and experimental results. In this run the

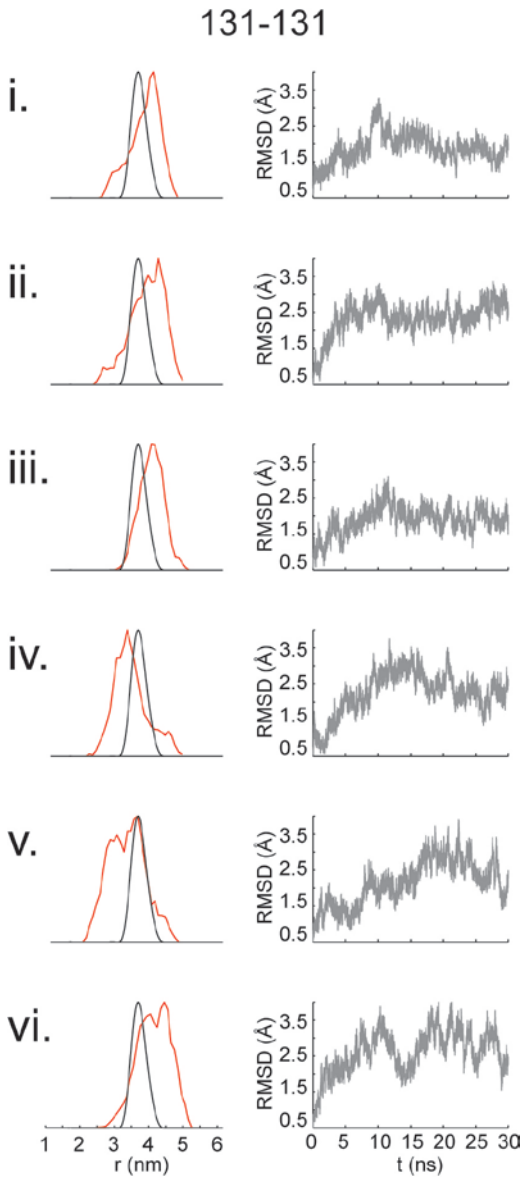

Figure 2-6. Comparison of the 131-131 experimental (*54*) (black) and simulated (red) distance distributions for runs **i-vi** which were found to possess stable RMSD trajectories. The local backbone RMSD trajectories are shown (gray).

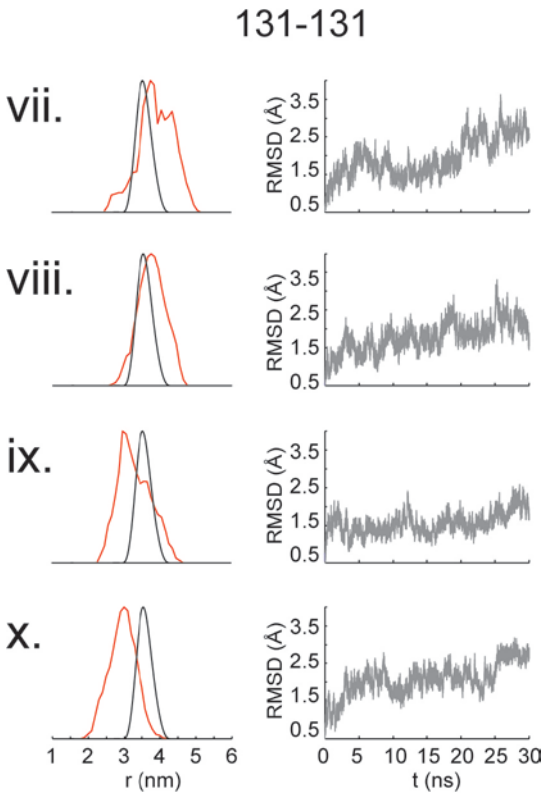

Figure 2-7. Comparison of the 131-131 experimental (*54*) (black) and simulated (red) distance distributions for runs **vii**-**x** which were found to possess high and unstable local backbone RMSDs as shown in gray.

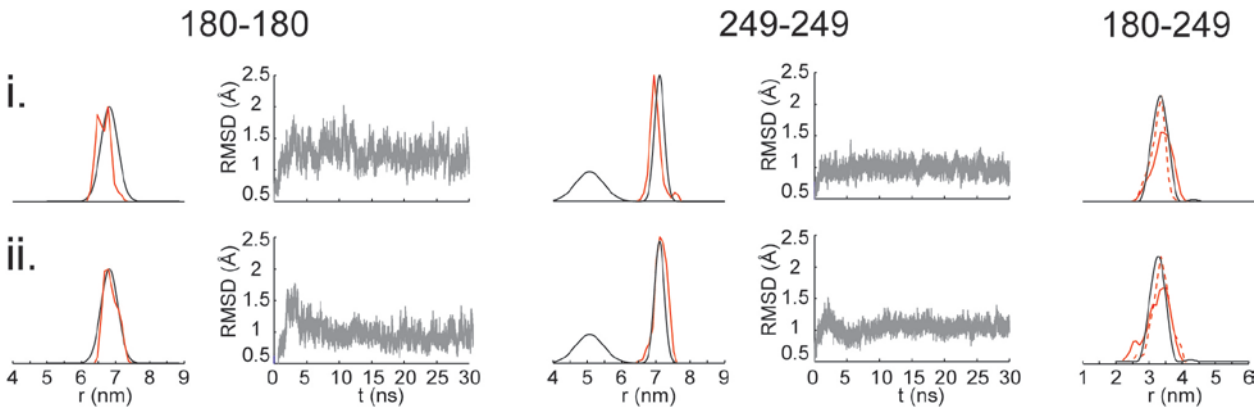

Figure 2-8. Comparison of the 180-180, 249-249, and 180-249 experimental (*54*) (black) and simulated (red) distance distributions for runs **i** and **ii** which were found to agree with all three experimental distance constraints. The local backbone RMSD trajectories are shown for both spin-labeled sites 180 and 249 (gray). The simulated 180-249 distances within the two monomers of EcoRI are shown as solid and dashed lines.

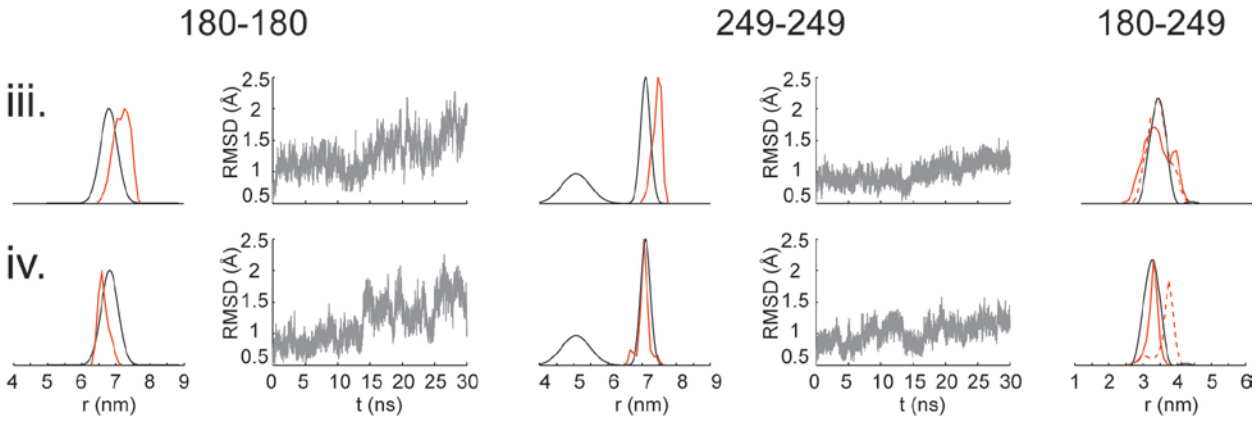

Figure 2-9. Comparison of the 180-180, 249-249, and 180-249 experimental (*54*) (black) and simulated (red) distance distributions for runs **iii** and **iv** which were found to possess high and unstable local backbone RMSDs as shown in gray for both spin-labeled sites 180 and 249.

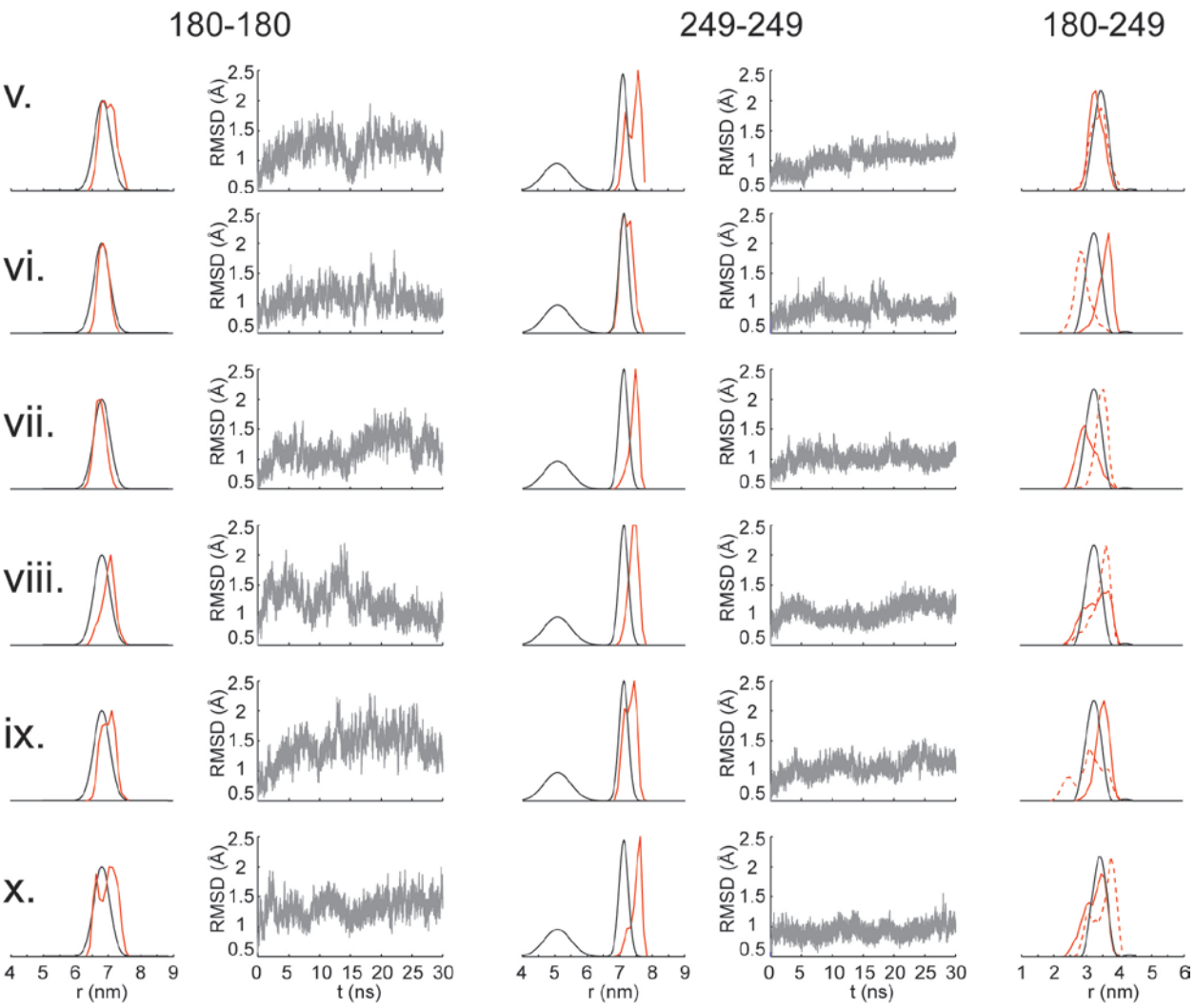

Figure 2-10. Comparison of the 180-180, 249-249, and 180-249 experimental (*54*) (black) and simulated (red) distance distributions for runs **v-x** which were found to not agree with at least one of the experimental distance distributions. The local backbone RMSD trajectories, which were stable in these runs, are shown for both spin-labeled sites 180 and 249 in gray.

180-180 and both of the 180-249 simulated distance distributions are found to compare well with that of the experimental distribution. The 249-249 distribution however does not, due to a bimodal distribution (within the 7.1 nm experimental distance measurement) and an average distance larger than experiment. Using such stringent criteria to identify the relevant simulation results increases the confidence in the data extracted from the simulations. It should be noted that in all 10 of the simulated 249-249 distance distributions, a distance corresponding to the shorter (5.1 nm) experimental distance was never observed. This supports the suggestion that a second conformation of the spin label is *not* the cause of the second, shorter experimental distance observed in the 249-249 DEER results.

MD runs that agreed with experimental data were used to extract backbone C_α-C_α distance distributions. Figure 2-11 shows simulated C_α-C_α distance distributions (blue) overlaid on the validated nitroxide-nitroxide (red) distributions. The gray dashed vertical line indicates the C_α-C_α distance obtained from the crystal structure of the specific EcoRI-DNA complex. The mean C_α-C_α 180-180, 180-249, and 249-249 distances from simulation were only 0.1-0.2 nm longer than that of the crystal structure. This small discrepancy may be attributed to the tighter packed structure of EcoRI in the crystalline state versus solution where the protein is more flexible and on average experiences larger C_α-C_α distances.

The standard deviations of the C_α-C_α distance distributions provided insight into the backbone mobility at the two spin-labeled sites. The standard deviations of the 180-180 C_α-C_α distance distributions were merely 0.02 nm larger than those of the 249-249 results, indicating that the backbone at site 180 (β-strand) is slightly more mobile than at site 249 (α-helix). This similarity may be due to both spin-labeled sites being located on stable secondary structural motifs, 180 on a β-strand and 249 on an α-helix. The slight increase in the backbone mobility at

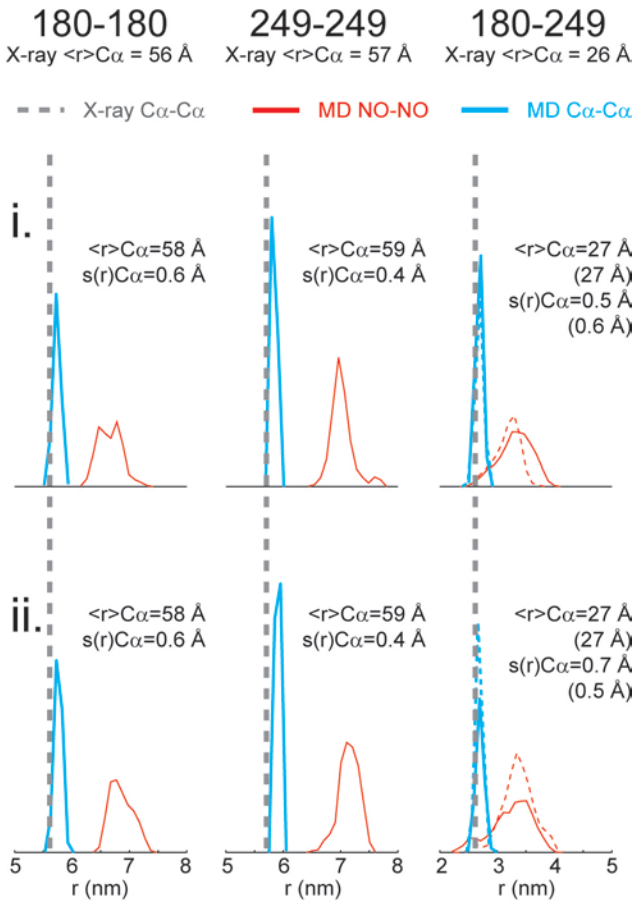

Figure 2-11. C_α-C_α distance distributions (blue) were extracted from the validated simulation results (red). The mean distances were compared to the C_α-C_α distance found in the crystal structure of the specific EcoRI-DNA complex (gray dashed line). The values from the crystal structure distances are listed above. The mean simulated C_α-C_α distance and standard deviation is listed by each distance distribution. The values in parentheses for the 180-249 distributions are those measured in the second monomer of EcoRI.

site 180 may arise from the β-strand being located on the outer arm of EcoRI. Indeed the RMSD values found at site 180 are slightly higher than those at site 249, contributing to the proposal that the arm region of EcoRI is slightly more mobile than the main domain. These results agree with the proposed order and rigidity of the main domain compared to the arm region in the crystal structure of the EcoRI apoenzyme.(*129*) CW experiments have been performed and analyses of this data are currently underway to further investigate the dynamics of these different spin-labeled sites in the EcoRI-DNA complex in solution.

Although there are clear differences in the nitroxide-nitroxide distributions between MD runs that agree with experiment and those that do not, the C_α-C_α distributions were fairly similar for all runs. The only exception to this occurred in runs that possessed an unstable RMSD and were found to have C_α-C_α distributions with larger standard deviations. This shows that MD simulations can distinguish spin label conformations even in the context of relatively invariant backbone distributions. Thus, favored spin label conformations can be extracted by comparing MD simulations with experimental data that provide multiple constraints.

Simulations were also carried out using the rotamer library approach implemented in the multiscale modeling of macromolecules (MMM) open-source package.(*99, 130*) Spin label scans were performed at sites 180 and 249 in the specific EcoRI-DNA complex. Although the program successfully replicated the 180-180 experimental distance distribution neither the 180-249 or 249-249 distributions agreed with experiment. The distance distributions comparing the experimental data and the distributions obtained from the rotamer library are shown in Figure 2-12. It can be seen in these fits that the 180-180 distribution agrees well with respect to the average distance as well as the standard deviation. However, the 249-249 distribution from the rotamer library possessed a lower average distance and a slightly broader distribution compared

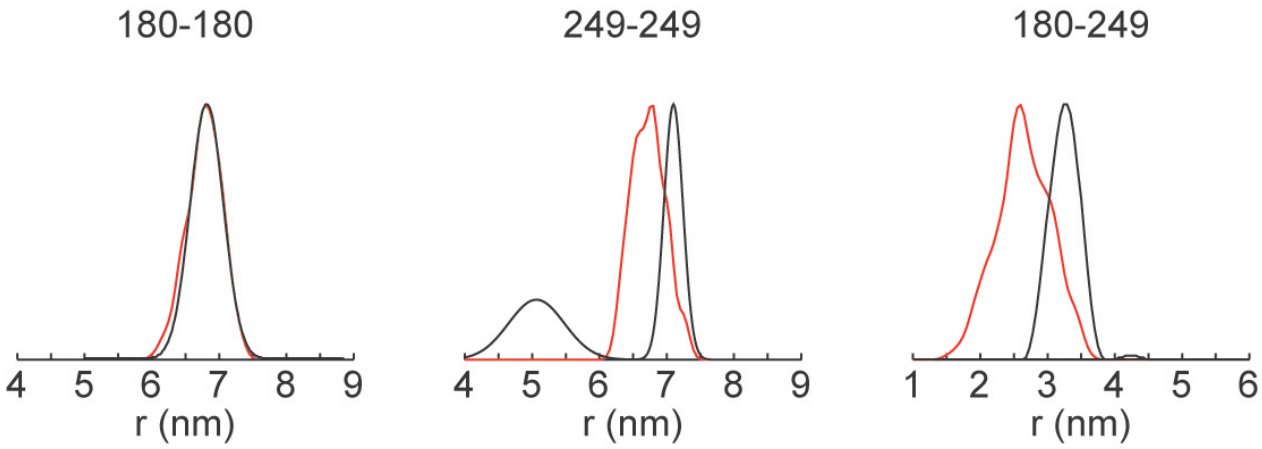

Figure 2-12. Distance distributions comparing the EcoRI 180-180, 249-249, and 180-249 DEER data (black) and the distributions constructed from the rotamer library approach (red).

to experiment. The most significant difference arises from that of the 180-249 distribution in which the rotamer library predicted an average distance 0.6 nm lower than the experimental distribution. This indicates that although the 180-180 simulation agreed with experiment, appropriate rotamers may not have been modeled which also agree with the 180-249 distribution.

2.4.3 Spin Label Dynamics and Conformers

In this work the MD results provided insight into the dynamics and conformers of the spin label located at sites in different secondary structures: 131 (loop), 180 (β-strand) and 249 (α-helix). Spin label dynamics and conformations were analyzed using those simulations that were determined to be consistent with the experimental distance distributions.

Polar plots, such as those used in previous works (*102-103, 105*), were constructed for each of the five dihedral angles that define the spin label side chain conformation (χ_1-χ_5). These plots are shown in Figure 2-13 for both sites 180 and 249. Each plot for a given dihedral angle displays the values sampled by that angle for both of the validated MD runs combined (runs **i** and **ii**). The radial distance from the center reflects the occupancy of that dihedral angle value throughout the portion of the simulation used for analysis (last 20 ns). In addition, the distribution about a value provides insight into the flexibility of that dihedral angle.

It can be seen from these polar plots that the dihedral angles sampled by sites 180 and 249 are similar to those found in the torsional potential energy surfaces constructed by Tombolato *et al.*(*96*) One exception to this is the value of χ_4 at site 180, where it samples a dihedral value of +110° in addition to the expected +75°. One can observe differences in the population of the dihedral angles sampled as well as the distribution about these angles between sites 180 and 249. The biggest difference arises between dihedral angles χ_1, χ_2, and χ_4. A

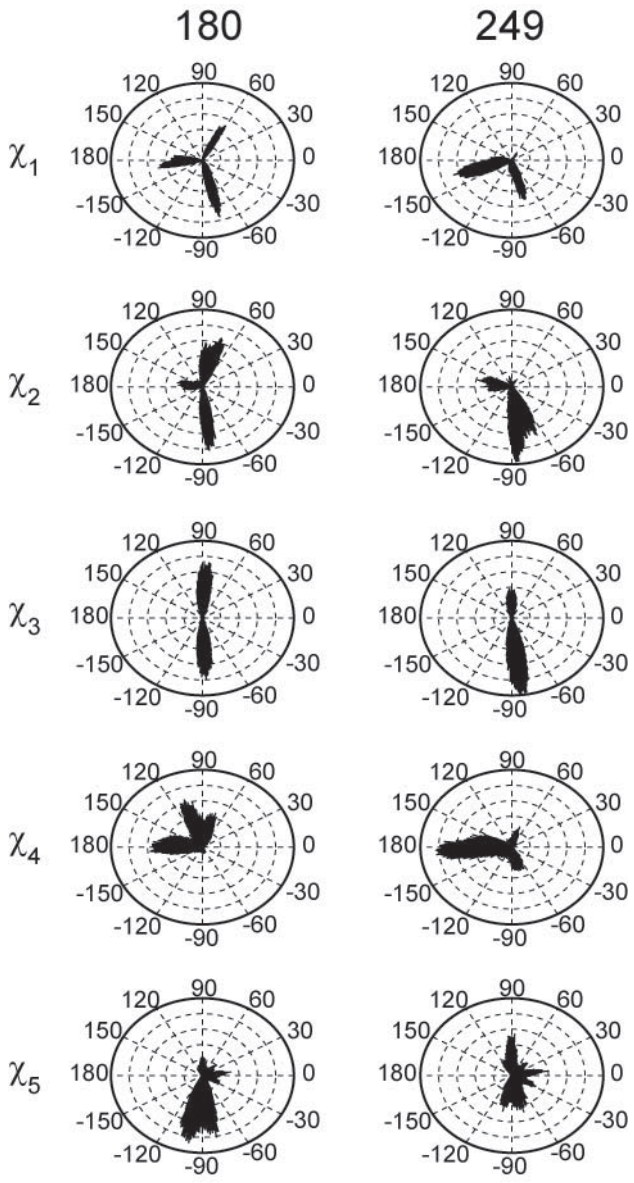

Figure 2-13. Polar plots illustrating the dihedral angle values sampled by the spin label at sites 180 and 249 for the simulations which agreed with experiment. The results of the two runs are combined in each of the plots for each site. The plots have been normalized with respect to the dihedral angle occupancy.

significant example is seen in the χ_1 occupancy of the +65° conformation. At site 180, which resides on an edge β-strand, this χ_1 conformation is significantly sampled. However at the α-helical site 249, this χ_1 conformation is infrequent. Similar trends are seen in values occupied by the χ_2 and χ_4 dihedral angles. Both the ±90° values of χ_3 are accessed at each site and χ_5 is equally flexible and samples a variety of values at both sites.

Similar polar plots were constructed for the 180-249 simulated results which did not agree with experiment (Figure 2-14). These plots show a different pattern in the dihedral angles that were sampled and their occupancy compared to the runs which were able to replicate the experimental distance distributions. The most significant difference at site 180 is the decrease in the χ_1 = +65° conformer and an increase in $\chi_2 = \chi_4$ = 180°. The spin label conformation is extended when $\chi_2 = \chi_4$, leading to an increase in the average nitroxide-nitroxide distance. This is true for any χ_1 or χ_3 orientation. Thus, conformations of the spin label at site 180 where $\chi_2 = \chi_4$ are more likely to not agree with experiment due to a larger average distance. At site 249 the polar plots which did not agree with experiment show a significant increase of $\chi_2 = \chi_4$ = 180° as well as χ_4 = +75°. Similar to site 180, an increase in $\chi_2 = \chi_4$ conformers at site 249 could lead to average nitroxide-nitroxide distances larger than experiment. There are also changes in the χ_3 profile for both sites, however, the occupancy of χ_3 is influenced by the initial assignment of the conformation and therefore no conclusions were drawn about changes in χ_3 between the different sets of fits. Comparison of the polar plots highlights the significance of identifying and analyzing the validated simulation results because it exposes conformers that are sampled in MD runs which are not experimentally relevant.

No correlation was found between the starting rotamer used for the spin label and agreement with experiment. However, starting with different rotamers of the spin label does

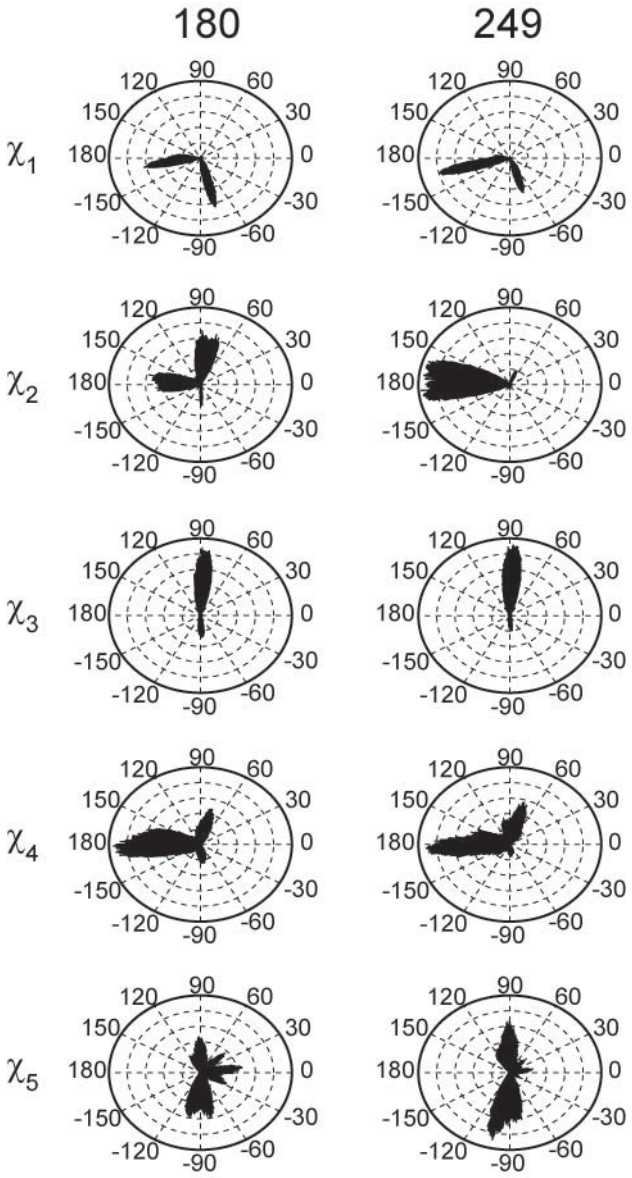

Figure 2-14. Polar plots illustrating the dihedral angle values sampled by the spin label at sites 180 and 249, for the simulations which did not agree with experiment. The results of runs **v** – **x** are combined in each of the plots for each site. The plots have been normalized with respect to the dihedral angle occupancy.

enhance the sampling of the spin-labeled location. For instance, although in each of the ten runs the starting orientation of the spin label was the same in both monomers of the EcoRI complex, the two spin labels still sampled different conformers. By enhancing the conformers sampled throughout the simulation, the chance of identifying conformers which agree with experiment is increased.

The distribution and jumps about these dihedral angles provides insight into the dynamics of the spin label. The χ_4 and χ_5 polar plots show several dihedral angles sampled as well as broad distributions about these values. This indicates increased torsional oscillations and jumps about the two terminal angles of the spin label. These oscillations and jumps are also evident in the time-dependent trajectories of χ_4 and χ_5 (Figure 2-15 and 2-16). The fast dynamics of χ_4 and χ_5 agrees with the previously proposed χ_4/χ_5 model of motion in which the main contributor to the spin label mobility has been proposed to arise from motion about the χ_4 and χ_5 dihedral angles.(*21, 25*)

Conformers found in runs **i** and **ii** of the validated results were identified at sites 180 and 249, allowing comparison of the conformers sampled by the spin label at different secondary structures. To identify the conformers sampled from the simulated results, the dihedral angles were rounded to those found in the torsional potential energy profiles of the spin label.(*96*) The conformers identified are listed in Figure 2-17 along with a pictorial representation to visually demonstrate the difference in the conformers at each site. The conformers shown in Figure 2-17 were the highest occupied in runs **i** and **ii**. Due to the flexibility in the χ_5 angle, all possible values of χ_5 were considered when identifying the conformers.

Using the cellular retinol-binding protein (CRBP), Lietzow and Hubbell suggested preferred geometries of several spin-labeled sites on interior and edge β-strands by CW-ESR

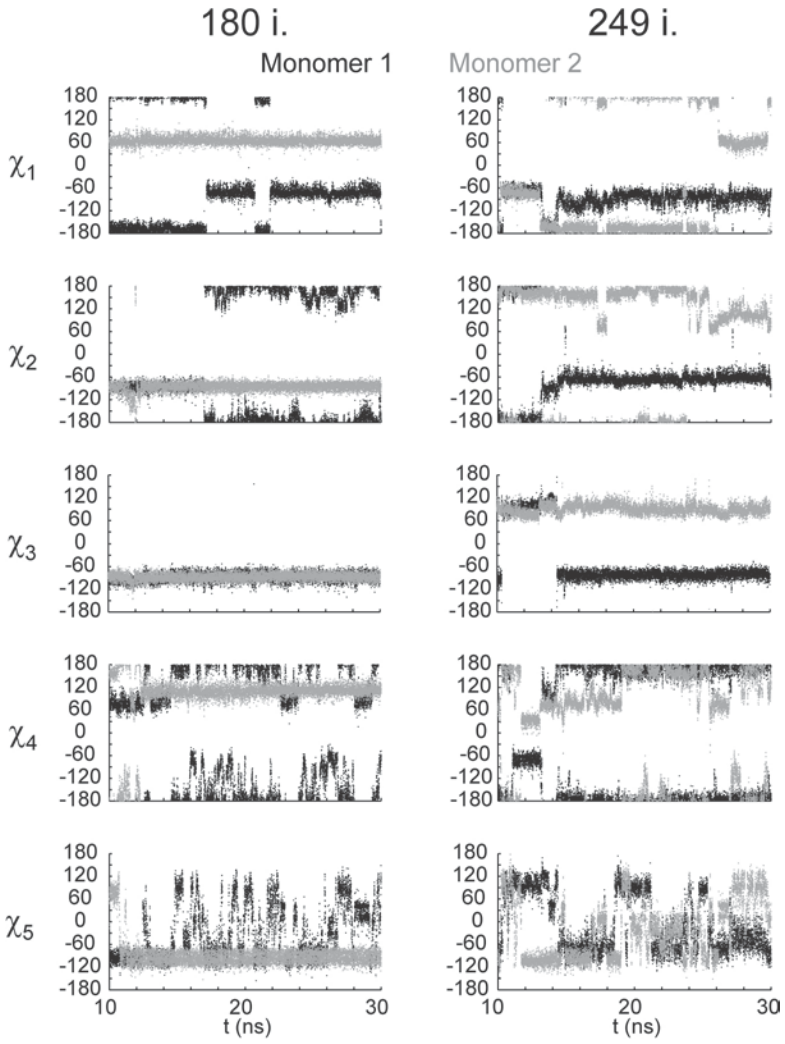

Figure 2-15. Time dependent trajectories of the five defining dihedral angles of the spin label at sites 180 and 249 for run **i**. The results are shown for each spin label on monomer 1 (black) and monomer 2 (gray).

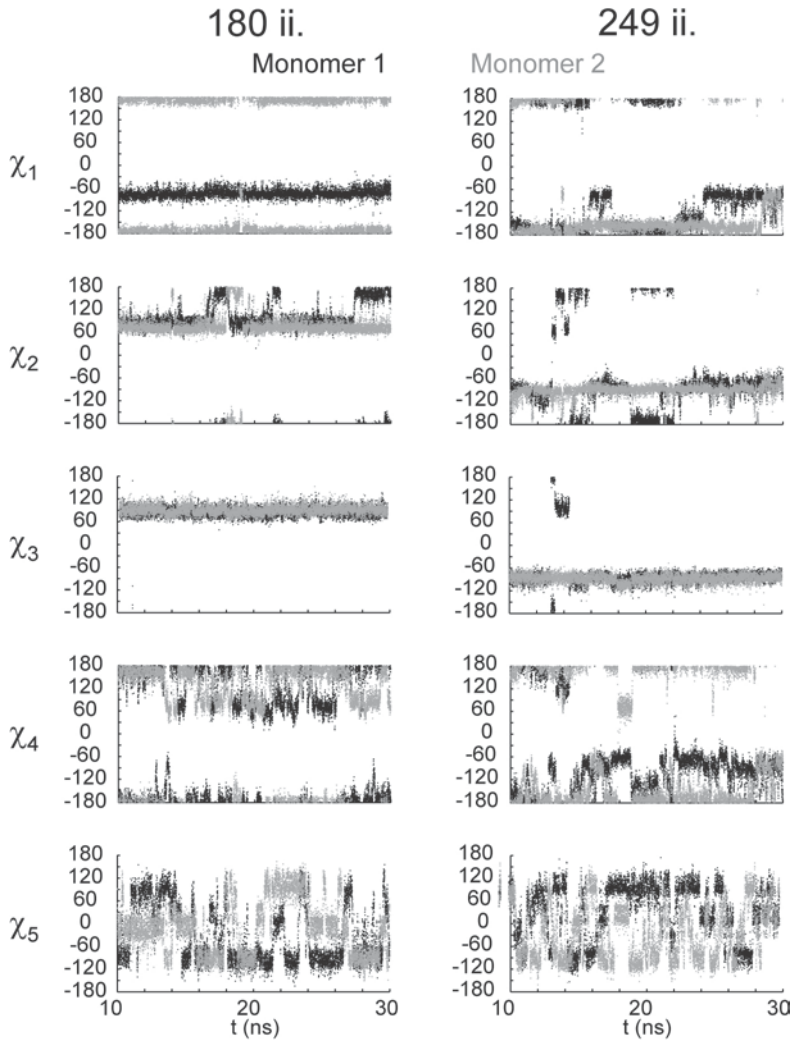

Figure 2-16. Time dependent trajectories of the five defining dihedral angles of the spin label at sites 180 and 249 for run **ii**. The results are shown for each spin label on monomer 1 (black) and monomer 2 (gray).

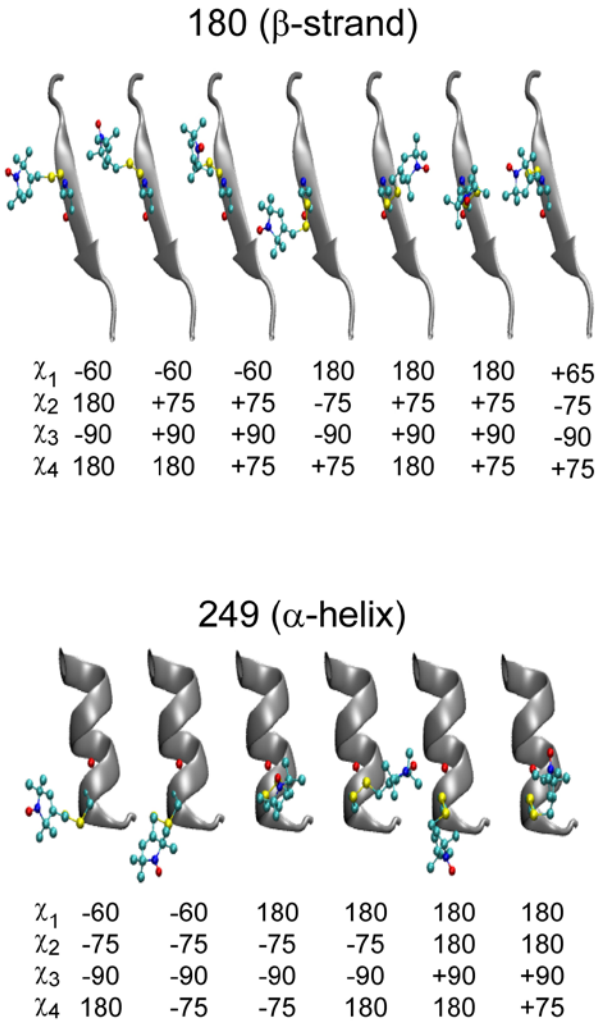

Figure 2-17. The significantly sampled conformers present in the validated simulations are shown for sites 180 and 249. Below the pictorial representations are the rounded dihedral angle values (χ_1-χ_4) for each conformation. All possible χ_5 values were considered in the identified conformers.

analysis and manual variation of the spin label conformation built into the CRBP crystal structure. From this work they proposed that edge strands, such as where 180 is located, favor [χ_1, χ_2] conformations of [+60, -60] and [+60, 180] (dihedral values as used by Hubbell and coworkers).(*31*) This is due to the non-hydrogen bonding (NHB) neighbor of the β-strand lying close to the spin label and therefore preventing the commonly observed [-60, -60] conformation. Indeed, the [-60, -60] conformer was rarely occupied in the validated MD results at site 180, but neither was the [+60, 180] conformation. The [+65, -75] conformer *was* observed, however. Other conformers were also observed such as [-60, +75], [-60, 180] and $\chi_1 = 180^o$ conformers.

These conformers may arise from the degree of strand twist in the β-strand or local side chain interactions at site 180. It was proposed that when the degree of strand twist increases the residues will spread out and reduce side chain - spin label interactions.(*31*) In addition, different conformers of the spin label at 180 reside in close proximity to residues in the outer arm of EcoRI. For example, the [180, +75] conformer is positioned in close proximity to an asparagine residue on the adjacent β-strand, which is the NHB neighbor of site 180. As pointed out by Lietzow and Hubbell (*31*), spin labels present on β-strands are expected to interact more with NHB neighbors that are β-branched residues, such as valine or isoleucine. It can be reasoned that due to the fact that the NHB neighbor of site 180 is not β-branched there exists little interaction between the two residues. Taken together with the strand twist present in the β-strand at site 180, alternative conformations of the spin label are possible.

As noted previously, most studies that have investigated spin label conformations and dynamics have been performed on α-helical sites. Although site 180 provides insight into the behavior of the spin label on a different secondary structure such as a β-strand, modeling on an α-helical motif, such as at site 249, provides a reference to compare these MD simulations with

the work of others. Using X-ray crystallography, several preferred spin label conformers have been identified on solvent accessible α-helical sites in T4 lysozyme. From these structures the most preferred [χ_1, χ_2] conformations were found to be: [-60, -60], [180, +60], and to a lesser extent [180, -60]. These conformers are also found to be energetically favorable in the DFT calculations performed by Warshaviak *et al.* (*97*) The [-60, -60] and [180, +60] spin label conformers are believed to be stabilized by the $S_\delta \cdots H\text{-}C_\alpha$ interaction of the spin label with the protein backbone.(*89, 97*) In the [180, -60] conformation the S_δ apparently interacts with the backbone C=O.(*97*) At site 249 two of these three preferred conformers were significantly sampled in the validated simulations: [-60, -75] and [180, -75]. Tombolato *et al.* and Sezer *et al.* both found the [-60, 180] conformer to be the most probable in their simulations on a polyalanine α-helix.(*96, 98*) The [-60, 180] conformation was observed at site 249, however, not as significantly as in the works of Tombolato *et al.* and Sezer *et al.* Lastly, the [180, 180] conformer was also sampled at site 249. The [-60, -75], [180, -75] and [180, 180] were also observed in the work of both Tombolato *et al.* and Sezer *et al.*, however to a lesser extent.

Hubbell and co-workers have shown that the [-60, 180] and [180, 180] conformers are sterically allowed at α-helical sites (i.e. those modeled in T4 lysozyme), but are rarely observed in the crystal structures. For example, the [-60, 180] conformer has been observed only once, and that at a crystal contact site.(*92*) It is proposed that these conformers are not stabilized by the $S_\delta \cdots H\text{-}C_\alpha$ interaction, and thus their χ_2 angles are less constrained, so that mobility or distribution among conformers produces weak crystallographic electron densities. Such disorder is not observed in the solution CW spectra.(*89*) Additionally, the [-60,180] conformation was found to possess the highest relative energy in the recent DFT calculations.(*97*) The MD force field used in this work lacks the appropriate details, such as polarizability, to observe the

possible lone pair interaction between the spin label S_δ atom and the hydrogen from the backbone H-C_α. Thus, these conformers may be less probable in experiment due to the stabilization of other conformers, i.e. [-60, -60], [180, +60], and [180, -60], by this interaction. Such discrepancies between simulation and experiment expose the limitations of the current simulation techniques. Even if the simulations are extended or general sampling is increased, the spin label may still sample conformers that are less likely to be observed experimentally. Thus, agreement between the MD results and experiment may not always be plausible even if the simulations are carried out for much longer timescales. Ultimately, only the conformers that agree with the experimental constraints should be considered.

Different preferred conformers were occupied by the spin label present on different secondary structures. Site 180, present on an edge β-strand, was the only site where the χ_1 = +65° conformer was significantly sampled. It has been mentioned that such a conformation of the χ_1 dihedral angle is sterically forbidden in nearly all α-helical sites(*89*), and in fact this conformer was rarely occupied at the 249 site. Interestingly, no one preferred conformer was the same for site 180 and 249. This underscores the sensitivity of the spin label to the secondary structural location.

2.4.4 Broad Utility of Approach

We have shown in this work the value of using MD simulations to model the spin label conformer and dynamics at two different secondary structures. Insight gained into the behavior of the spin label on a β-strand is significant due to the limited amount of information that exists on the behavior of the spin label in β-strands or β-sheets. In addition, we have demonstrated the need to extend MD simulations to longer timescales (> 10 ns) to ensure backbone equilibration

of the system as well as to effectively sample the spin label conformers. We have also shown that the use of correlated experimental distance constraints can provide strict criteria for agreement between simulation and experiment, and thus for identifying the most probable conformers in solution. Since the favored conformations of the spin label are likely to depend primarily on highly local features of its secondary structure environment, these favored conformations can then be used to deconvolute positional distributions of the spin label from positional distributions of the backbone. The potential utility of our approach is thus in establishing the favored spin label conformation for a particular location in a protein. This information can then be used to extract differences in backbone distributions when comparing complexes of the same protein (whose secondary structure should often be conserved) with different ligands or under different solution conditions. This work underscores the need for new methods to simulate spin label packing and conformations in different systems and at different secondary structures. Methods such as the rotamer search (*110-111, 114*) and rotamer library (*63, 99-100*) provide alternative means to account for spin label conformational distributions.

2.5 CONCLUSIONS

ESR-DEER experiments on proteins yield distance distributions which convolute the effects of backbone positions and motions with preferred conformations and dynamics of the spin label moieties. These factors can be deconvoluted by MD simulation, provided that the simulations accurately reproduce the experimental ESR-DEER data. This we have done successfully for spin-labeled sites 180 and 249 of the specific EcoRI-DNA complex, also allowing us to compare spin label behaviors when located on a β-strand or an α-helix. These simulation studies enhance

our understanding of the behavior of spin labels in proteins and thus expand the ability of ESR spectroscopy to contribute to knowledge of protein structure and function.

2.6 ACKNOWLEDGEMENTS

The MD and ESR studies were supported by National Science Foundation (MCB 0842956) grant to S. S. and L. J-J. Generation of mutant proteins and spin labeling were supported by National Institutes of Health MERIT (5R37-GM029207) grant to L. J-J. The simulations were also supported by the NSF through TeraGrid resources provided by the Pittsburgh Supercomputing Center under grant number TG-CHE100114 and the University of Pittsburgh Center for Simulation and Modeling. J. L. S. thanks Mike Yonkunas for helpful instruction on the MD simulations and Dan Zuckerman for his insight on the manuscript.

3.0 ELECTRON SPIN RESONANCE REVEALS THAT THE PROTEIN-DNA INTERFACE IS SENSITIVE TO DIFFERENT CLASSES OF A PROTEIN-DNA COMPLEX

3.1 ABSTRACT

Protein dynamics and order may play a role in the specificity with which some DNA-binding proteins recognize their specific DNA sites. In this work, the potential of site-directed spin labeling to resolve changes in dynamics of EcoRI bound to its specific, miscognate (one base pair mismatch), and nonspecific ($\geq$ 2 base pair mismatch) DNA sites was investigated. Continuous wave (CW) spectra were analyzed for spin-labeled sites at various positions in a region of the protein that has previously been implicated to play a role in the binding specificity. Quantitative information on dynamics was obtained by simulating the X-band CW spectra based on the stochastic Liouville equation. The protein-DNA interface was found to be most sensitive to the changes between the complexes, demonstrating clear differences in the spin label dynamics and order. CW spectra for the spin-labeled sites located further away from the DNA showed little variation in dynamics between the complexes. However, a possible conformational transition in the EcoRI-DNA complexes was detected at these surface-accessible sites. This work localizes the area of the protein that is most sensitive to conformational-vibrational changes

between the different EcoRI complexes. This work also demonstrates the ability of ESR to differentiate between dynamics in a set of related complexes.

3.2 INTRODUCTION

Protein-DNA interactions play an important role in many biological processes such as transcription and genome repair, where recognizing and binding to the correct DNA sequence is critical. Such is the case for restriction endonucleases, a group of enzymes that bind to and cleave foreign DNA at specific sites. Cleavage of the wrong DNA sequence can have fatal consequences. For this reason, restriction endonucleases possess a high affinity for their correct DNA binding site.

The restriction endonuclease, EcoRI, has been the subject of extensive genetic, biochemical, and biophysical research.(*119, 131*) EcoRI has been shown to bind to its specific recognition site (GAATTC) with a binding affinity that is ~50,000-90,000-fold greater than to a site that differs by one base pair (miscognate sites).(*117-118*) For nonspecific sites, where the DNA sequence differs from the specific by two or more base pairs, the binding affinity is as poor as for the weakest miscognate site.

This binding specificity makes EcoRI an ideal model to investigate the protein-DNA interactions that are responsible for specific DNA recognition and binding. To gain a full understanding of how EcoRI discriminates between different DNA sequences, thermodynamic profiles ($\Delta G°$, $\Delta H°$, $T\Delta S°$, $\Delta C_p°$) of each of the complexes has been measured.(*131-132*) The heat capacity change ($\Delta C_p°$) was found to differ most between the three EcoRI complexes (specific, miscognate, and nonspecific). A strongly negative $\Delta C_p°$ is the hallmark of the

formation of a specific protein-DNA complex. A negative $\Delta C_p°$ for a specific protein-DNA complex arises due to the hydrophobic effect and restriction of conformational and vibrational freedom of the protein, DNA, and interfacial waters. These factors are all present in the specific EcoRI complex, giving rise to a largely negative $\Delta C_p°$. The $\Delta C_p°$ for the miscognate complex is only moderately negative and near zero for the nonspecific complex. For this reason, it is believed that the noncognate complexes (i.e., miscognate and nonspecific) form looser complexes with the DNA and have more freedom of motion than the specific complex.(*129, 132*)

EcoRI is a 62 kDa homodimer that consists of a large, stable main domain and an arm domain. Each arm consists of an inner and outer segment. Crystal structures are available for the free enzyme and the enzyme in complex with specific DNA. The arms are invisible in the free complex, but become partially ordered and enfold the DNA in the specific complex.(*129*) The structure of the specific complex is shown in Figure 3-1A where the main domain is shown in silver, the DNA yellow, and the inner and outer arms highlighted in blue and red, respectively.(*119-120*)

Crystal structures of the specific complex as well as ethylation interference (DNA phosphate) footprinting of the specific and miscognate complexes indicate that the arms may play a role in the binding specificity of EcoRI. In particular, the arms have been found to provide important phosphate contacts that stabilize the DNA conformation in the specific complex.(*117, 120, 133*) Footprinting results indicate that some key phosphate contacts are missing in the miscognate complex. Other than these footprinting results there is virtually no residue level structural information on EcoRI bound to a noncognate sequence. This is a common problem for endonucleases where for the ~3600 known restriction endonucleases, only four structures of miscognate and nonspecific complexes have been determined.(*134-137*)

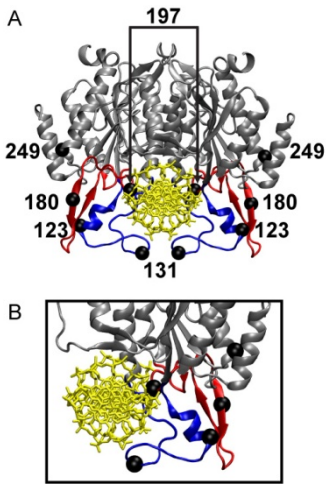

Figure 3-1. A. The crystal structure of the specific EcoRI-DNA complex (PDB: 1CKQ) (*120*). The main domain is highlighted in silver and the DNA in yellow. The inner and outer arms are shown in blue and red, respectively. The spin-labeled residues are shown as black spheres. B. One monomer of EcoRI with the DNA is shown at a closer view. Here it can be seen that sites 123, 131, and 197 are located on the inner arm and site 180 is located on the outer arm. Site 249 resides in the main domain of the complex.

To probe the behavior of the EcoRI arm region upon binding different sequences of DNA, double electron-electron resonance (DEER) experiments were previously performed on the specific, miscognate, and nonspecific EcoRI complexes. The three sequences used in the previous and current work are shown in Figure 3-2. The specific, miscognate, and nonspecific sites are highlighted and base pair changes are indicated in red. In the previous work, distance measurements were made across the inner and outer arms and from the outer arm to the main domain of EcoRI. For each of the measurements, similar average distances were obtained between the three complexes. It was thus concluded that the arms envelop the DNA in each of the complexes and are similarly oriented on average, suggesting that the DNA resides in the same binding cleft of EcoRI in the different complexes. Furthermore, in two of the measurements the noncognate complexes were found to have broader distance distributions than the specific complex. This may indicate that the arms of EcoRI may have more conformational freedom in the noncognate complexes.(*54*)

The goal of the current work is to identify regions of the EcoRI-DNA complex that display changes in dynamics and/or order between different complexes. Site-directed spin labeling in conjunction with electron spin resonance (ESR) is an ideal candidate for probing the change in dynamics of the EcoRI complexes. Continuous wave (CW) ESR has proved to be an effective method to resolve the dynamics of spin-labeled proteins.(*4, 18, 25-28*)

Qualitative measures such as spectral breadth and the inverse central line width (δ^{-1}) have been previously employed to probe nitroxide mobility.(*4, 21, 138*) Alternatively, quantitative dynamical information can be extracted from the CW spectra through simulation based on the stochastic Liouville equation.(*15-16*) The CW line shape is sensitive to reorientational rates

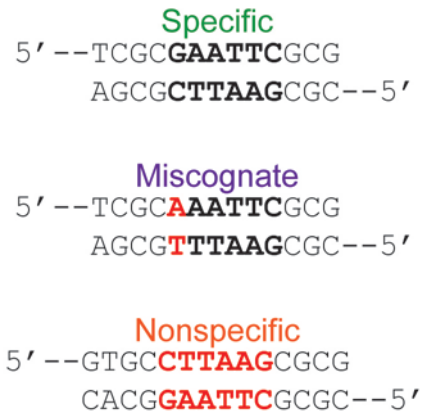

Figure 3-2. Full sequences for the specific, miscognate, and nonspecific DNA used to construct the mutant EcoRI-DNA complexes. The significant binding sequences are highlighted in bold. The base pairs which differ from the specific sequence are also highlighted in red.

as well as molecular ordering of the spin label. The reorientational rates of the spin label contain contributions from the internal motion of the side chain, backbone motions, and overall rotational motions of the protein. However, for soluble proteins with a molecular weight $\geq$ 50 kDa the contributions of the overall protein reorientational diffusion is negligible.(*27*) The ordering of the spin label reflects the restriction in its amplitude of motion due to interactions with the protein as well as backbone motions. Often the term mobility is used to describe the combined effects of the reorientational rates and ordering on the CW spectrum. Using the simulation technique several CW-ESR dynamics analyses have been used to investigate spin-labeled sites in T4-lysozyme (*25, 30, 32, 89-91*) as well as other soluble (*27, 31*) and membrane proteins (*94-95, 139*) and nucleic acids (*33, 140*). To date, however, CW-ESR has not been used to probe the difference in dynamics and order between classes of a system.

One of the most thoroughly investigated protein systems using CW simulation is T4 lysozyme. A vast amount of work has been done using T4 lysozyme to better understand the change in rotational rates and molecular ordering at different spin-labeled sites and how these parameters reflect the change in protein backbone dynamics. (*25, 30, 32, 89-91*) Using this model system, the χ_4/χ_5 model was developed to describe the motion of the spin label at solvent-accessible, non-interacting helical sites. In this model the internal motion of the spin label is believed to be dominated by rotations about the terminal χ_4 and χ_5 dihedral angles. This arises due to a hydrogen bond interaction between the spin label and protein backbone which stabilizes the orientations of the χ_1 and χ_2 dihedral angles.(*21, 25*) The majority of the work concerning the χ_4/χ_5 model has revolved around spin-labeled sites on α-helices. The relevance of this model at other secondary structures, however, is of interest. It has recently been shown that orientations

of the spin label are possible on a β-sheet for which the hydrogen bond interaction between the spin label and backbone is absent.(*95*)

Site 72 in T4 lysozyme, located on a long, stable, α-helix has been viewed as a model spin-labeled site to describe the internal motions of the spin label. This is due to the fact that the backbone mobility at this site is low. In addition, the spin label is not involved in any tertiary interactions or interactions with nearby residues at this site. Thus, the motion of the spin label is dominated by the internal motions of the spin label. The rotational rate and order parameter, which quantifies the restricted motion of the spin label, were found to be 8.3×10^7 s^{-1} and S_{20} = 0.47, respectively, at site 72. By comparing to site 72, the variation in order and rotational rates at different spin-labeled sites in T4 lysozyme has been investigated to understand the contribution of backbone motions and local interactions to the CW spectrum.(*25*, *89*) For example, spectra for site 131 in T4 lysozyme, located on a short α-helix were fit using the same rotational rates as at site 72, however, a lower order parameter was needed (S_{20} = 0.35). The difference between the two sites was attributed to the increase in backbone mobility at site 131 reducing the restriction of spin label motion at this site. These results concur with those of the crystal structure of T4 lysozyme where site 131 was found to possess higher Debye-Waller factors compared to site 72.(*25*)

As mentioned previously, order describes the restriction of motion of the spin label due to local interactions with the protein side chains or backbone, as well as, the extent of protein backbone motion. Using T4 lysozyme, a physical interpretation of the order parameter was explained in terms of the χ_4/χ_5 model. In this system, the restriction of the spin label motion arises not only from the S_δ interaction with the protein backbone, but also from interactions between the S_δ and a hydrogen or methyl group in the nitroxide ring of the spin label.(*25*) These

interactions restrict the rotation about the χ_5 dihedral angle of the spin label. The order parameter has also been shown to have physical relevance in the backbone mobility of a DNA-binding peptide, GCN4-58 bZip. Work on this system was found to agree with previous NMR relaxation experiments. Although defined differently, the change in order parameters for both NMR and ESR both indicated a gradient of backbone mobility along the DNA-binding region of this peptide.(*27*)

In this work, X- and W-band CW spectra were collected for five mutated sites in EcoRI, in three different complexes: specific (GAATTC), miscognate (AAATTC), and nonspecific (CTTAAG). Sites 123, 131, and 180 were chosen to probe the change in dynamics of the inner and outer arms upon binding different sequences of DNA. Site 197, which also lies on an arm, was chosen because it is closer to the protein-DNA interface. The DEER experiment was also performed at this site to measure the 197-197 distance in the three EcoRI complexes. Lastly, site 249 was chosen to be used as a reference in the stable, main domain of the EcoRI complex. These sites are shown in Figure 3-1. In this way, changes between the different EcoRI complexes were probed as a function of spin label site. Comparisons were made among the different spin-labeled sites to provide insight into the locations of the EcoRI-DNA complex which are most sensitive to the changes in the conformational-vibrational freedom of the complexes.

3.3 METHODS

3.3.1 Construction of EcoRI Mutants

Mutants of EcoRI were generated as described previously (*126*) and spin-labeled at sites 123, 131, 180, 197 and 249 (Figure 3-1A) using the methanethiosulfonate (MTS) spin label. A protein concentration of 60-180 μM was achieved for each of the samples. Appropriate salt concentrations (0.22 M) and pH (7.3) as well as excess DNA were used to ensure that nearly all the sample existed as the protein-DNA complex. All of the samples were prepared in 10% glycerol with the exception of the 30% Ficoll 70 samples that were also prepared for the 123 and 197 spectra.

3.3.2 ESR Measurements

The 9 GHz continuous wave ESR spectra were collected using a Bruker EleXsys CW/FT X-band ESR spectrometer with the Bruker Super High Sensitivity CW resonator (room temperature) or X-band ER-MD5 resonator (low temperature). The X-band spectra were collected using a 1 G modulation amplitude and a modulation frequency of 100 kHz. The temperatures were maintained using an Oxford ITC 503 temperature controller and CF935 dynamic continuous flow cryostat. For temperatures of 293 K and below the temperatures were maintained using liquid nitrogen. The 95 GHz spectra were collected using a Bruker ElexSys E680 FT/CW W-band ESR spectrometer with a Bruker W-band EN600-1021H resonator. Spectra were collected at the Bruker Biospin facility in Billerica, MA. Samples of less than 1 μL were loaded in a 0.1 mm ID quartz capillary tube and analyzed under a microscope to ensure there were no air

bubbles in the capillary. The temperature was maintained at 293 K using nitrogen gas flowing through a copper coil which was cooled by an ice bath. The W-band spectra were collected using a 4 G modulation amplitude and a modulation frequency of 100 kHz.

In addition to the other published distance measurements on the EcoRI-DNA complexes, the 197-197 distance was also measured.(*54*) In this work, the DEER experiment was performed using a Bruker EleXsys CW/FT X-band ESR spectrometer with the Bruker X-band ER-MD5 resonator. Each of the 197 DEER samples was prepared in 30% deuterated glycerol, 65% deuterated water, and 5% protonated water. Appropriate salt concentrations (0.22 M) and pH as well as an excess of DNA was used to ensure that at least 99% of the sample existed as the protein-DNA complex.(*141*) The samples were flash frozen by plunging the capillaries into liquid nitrogen cooled propane. The DEER experiments were performed at 40 K using an Oxford ITC 503 temperature controller and CF935 dynamic continuous flow cryostat. DEER experiments were performed using the four-pulse sequence: $(\pi/2)_{\upsilon 1}$-τ_1-$(\pi)_{\upsilon 1}$-T-$(\pi)_{\upsilon 2}$-τ_2-$(\pi)_{\upsilon 1}$-τ_2. The observer $(\pi/2)_{\upsilon 1}$ and $(\pi)_{\upsilon 1}$ pulses were 16 and 32 ns respectively, and the pump $(\pi)_{\upsilon 2}$ pulse was 12 ns for both peptide samples. The pump pulse was located at the maximum of the nitroxide spectrum with the observer pulse applied at a frequency ~70 MHz higher. A step size of 8 ns was used and the integrated echo intensity was collected for 256 points. A two-step phase cycling (+x, -x) was carried out on the first $\pi/2$ pulse. The pump pulse began 40 ns before the echo so that the zero time could accurately be determined.

3.3.3 Spectral Fitting

The hyperfine (A) tensor and g-tensor (g) parameters were obtained by fitting low temperature rigid limit spectra using the solid-state (pepper) model in EasySpin.(*142*) These parameters,

shown in Table 3-1, were then held fixed when fitting the room temperature spectra. The fits to the low temperature spectra are shown in Figure 3-3. The values found for both the g and A-tensors are similar to those found at other solvent-exposed α-helical sites.(*25, 27, 30*)

Non-linear least-squares fits to the room temperature spectra were performed using the anisotropic Brownian diffusion and microscopic order macroscopic disorder (MOMD) models present in the NLSL program developed by Freed and coworkers.(*15-16*) The anisotropic Brownian diffusion model mimics diffusive motion using an infinitesimal number of reorientational steps. In the MOMD model, the motion of the spin label is constrained by an ordering potential that represents the ordering of the spin label due to its local environment.

In each of these simulation models the local rotational motion of the spin label and backbone were fit using the average rotational rate constant ($\overline{R}$) and the anisotropy parameter (N) where (*15*):

$$\overline{R} = \sqrt[3]{R_{\perp}^{2} R_{\parallel}}$$
$$N = \frac{R_{\parallel}}{R_{\perp}} \qquad (3\text{-}1)$$

The rotational rate constant can be described in terms of the mean rotational correlation time which is defined as $\tau = 1/6\,\overline{R}$. The rotational diffusion tensor described by these rotational parameters is transformed into the nitroxide magnetic axis system by three Euler angles (α_D, β_D, γ_D). In this work only β_D was used as a fitting parameter, $\alpha_D = \gamma_D = 0$ as is usual for an axially symmetric rotational tensor.(*30-31*) The ordering potential coefficient, c_{20}, was also used in the simulations which were done using the MOMD model. The ordering potential U(Ω) in the MOMD model can be expanded into a series of spherical harmonics (*14*):

Table 3-1. g and A-tensor Values from Low Temperature Spectra

Mutant Complex	g_{xx}	g_{yy}	g_{zz}	A_{xx}	A_{yy}	A_{zz}
197 Specific	2.0082	2.0064	2.0020	6.2	6.2	35.7
197 Miscognate	2.0082	2.0064	2.0020	6.2	6.2	35.7
197 Nonspecific	2.0082	2.0064	2.0020	6.2	6.2	35.7
123 Specific	2.0082	2.0064	2.0022	6.2	5.1	35.9
123 Miscognate	2.0082	2.0064	2.0022	6.2	5.1	35.9
123 Nonspecific	2.0082	2.0063	2.0022	6.2	5.1	35.6
131 Specific	2.0083	2.0061	2.0020	6.2	5.1	36.3
131 Miscognate	2.0083	2.0062	2.0020	6.2	5.1	36.3
131 Nonspecific	2.0083	2.0064	2.0023	6.2	5.1	36.3
180 Specific	2.0081	2.0062	2.0020	5.7	5.3	36.3
180 Miscognate	2.0083	2.0063	2.0022	6.1	5.4	36.0
180 Nonspecific	2.0083	2.0062	2.0020	6.1	5.7	36.8
249 Specific	2.0084	2.0066	2.0022	6.2	5.1	35.6
249 Miscognate	2.0084	2.0063	2.0020	6.2	5.1	35.6
249 Nonspecific	2.0084	2.0063	2.0020	6.2	5.1	35.6

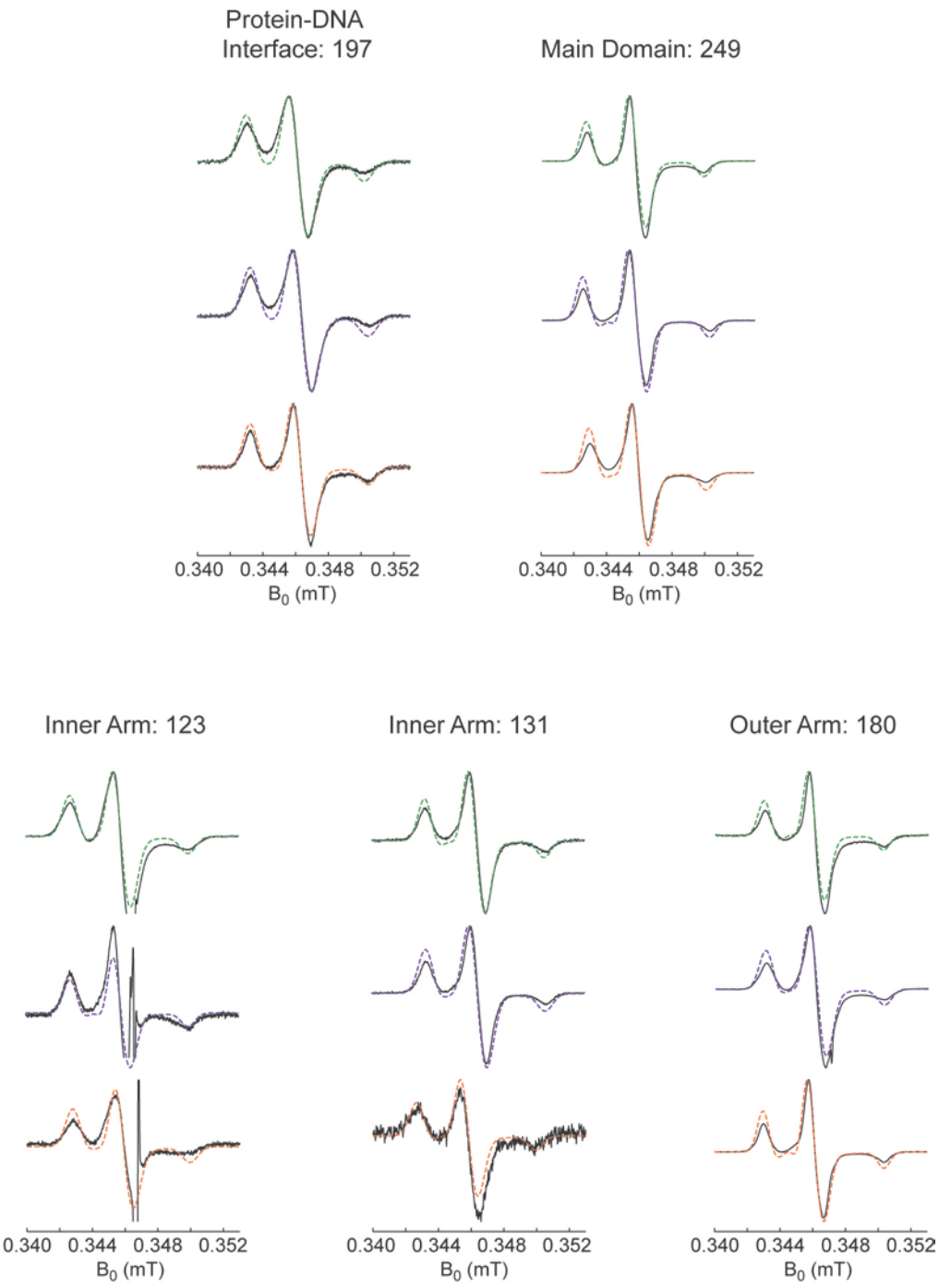

Figure 3-3. Simulated fits to the low temperature CW spectra. The fits provided the g and A-tensor values used for the subsequent room temperature simulations.

$$U(\Omega) = -k_B T \sum_{L,K} c_{LK} D_K^L(\Omega) \tag{3-2}$$

where $\Omega = (\alpha, \beta, \gamma)$ are the Euler angles between the rotational diffusion tensor and the local director frame (fixed on the protein) which reflects the ordering of the spin label due to local structural features of the protein environment. The order parameter, S_{20} is defined as:

$$S_{20} = \left\langle D_0^2 \right\rangle = \left\langle \frac{1}{2}(3\cos^2\beta - 1) \right\rangle \tag{3-3}$$

This parameter can be calculated from the ordering potential coefficient, c_{20}.(*14, 143*) Lastly, all spectra were fit using the isotropic inhomogeneous line-broadening parameter, W.

In order to reduce the number of parameters, the fits were initially performed using the anisotropic diffusion model. Order was introduced into the simulations which could not be successfully fit using just the diffusion model. The initial search for parameters was performed by reducing the χ^2 which was also used at first to measure the quality of fit. However, χ^2 is biased towards the quality of fit to the central line of the CW spectrum; therefore it was not always reliable or appropriate. Therefore, the final quality of fit to the data was assessed by focusing on the low-field region of the spectrum which was found to show the biggest difference between the complexes.

3.3.4 MD Simulations

Sites 131, 197, 180 and 249 on the crystal structure of the specific EcoRI-DNA complex (*119-120*) were mutated to nitroxide spin-labeled cysteines using the VMD program.(*122*) A Metropolis Monte Carlo minimization (MMCM) rotamer search was then performed in CHARMM (*123*) using the rotamer search program developed by Fajer *et al*.(*110*) Parameters

describing the spin label force field were taken from the work of Sezer *et al*.(*98*) The CHARMM27 force field was used for the protein and DNA.(*124*) Two singly (131 and 197) and one doubly labeled (180 and 249) specific EcoRI-DNA complexes were constructed for MD simulation.

All structures were solvated in an explicit water box and counter ions were added to neutralize the system and provide a salt concentration comparable to experiment ([NaCl] = 0.22 M). All MD simulations were performed using the NAMD program.(*125*) The structures were energy minimized using a conjugate gradient method. After heating the system to 300 K, the system was equilibrated for 1 ns in an NPT ensemble of 1 atm using a Langevin piston. During both the minimization and equilibration steps the protein backbone and DNA were restrained as well as the spin labels. Production runs were performed in an NVT ensemble for 60 ns using a 2 fs time step. Periodic boundary conditions were used and particle mesh Ewald summation was used to treat the electrostatic interactions. Visualizations were done using VMD.(*122*)

3.4 RESULTS

Five EcoRI mutants were constructed with the MTS spin label introduced at sites 123, 131, 180, 197 and 249. Sites 123 and 131 were chosen to probe the dynamics at the inner arm of EcoRI. Site 123 resides on an α-helix in the "hinge" of the inner arm whereas 131 is located on a loop at the end of the inner arm. The outer arm was also investigated at site 180 which resides on an edge β-strand. Site 197 resides on a loop sight in the inner arm of EcoRI and was chosen to probe the protein-DNA interface of EcoRI. Lastly, 249, which resides on an α-helix, was chosen

as a reference spin-labeled site as it is located in the main domain of EcoRI and should not be sensitive to changes in the arm dynamics with change in the DNA sequence. The mutants were bound to the specific (GAATTC), a miscognate (AAATTC), and a nonspecific (CTTAAG) sequence of DNA, resulting in a total of 15 spin-labeled EcoRI-DNA complexes. In all cases, excess DNA, and appropriate salt concentrations and pH were used to ensure that at least 99% of the sample exists as the protein-DNA complex.(*141*) In addition, the functionality of all the spin-labeled mutants was confirmed as described previously.(*54*)

Room temperature (293 K) X- and W-band CW spectra were collected on the complexes. The X-band spectra were further used for simulation. Variable temperature X-band spectra were collected on the mutants in the arm region to probe changes in the dynamics of these spin-labeled sites as the temperature is decreased. Additionally, variable viscosity X-band spectra were collected on the complexes spin-labeled at sites 123 and 197 to investigate the contribution of the protein global tumbling on the spectra. Room temperature spectra were collected on these samples in the presence of 10% glycerol (as all the other samples) or 30% Ficoll 70. These spectra are shown in Figure 3-4 where the solid line represents the spectra in 10% glycerol and the dashed line the spectra in 30% Ficoll 70. In the case of 197, the spectra at different viscosities are nearly identical. This indicates that the global tumbling of the EcoRI-DNA complex is on a slow enough time scale that it has a minimal effect on the X-band spectra. Indeed work on smaller systems, such as the DNA-bound GNC4-58 dimer, have shown little effect from global mobility.(*27*) In the case of the DNA-bound GNC4-58 dimer the total molecular weight of the complex was 50 kDa; however, the EcoRI dimer alone possesses a molecular weight of 62 kDa. In the 123 spectra the specific complex does show a small variation with change in sample viscosity. The spectra are slightly broader in the noncognate complexes

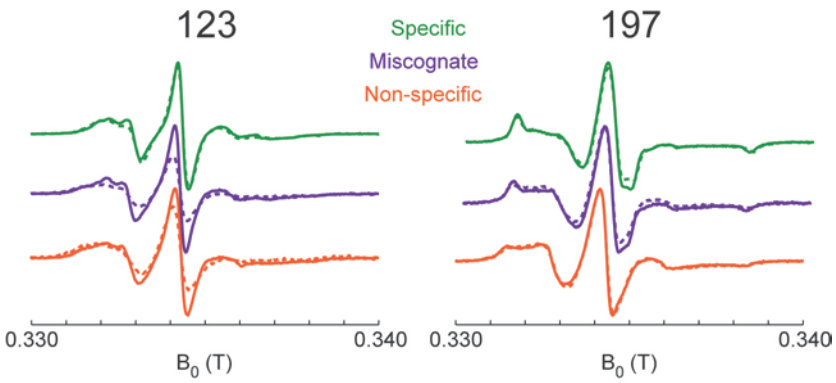

Figure 3-4. Room temperature X-band spectra of sites 123 and 197 in the specific (green), miscognate (purple), and nonspecific (orange) complexes in 10% glycerol (solid line) or 30% Ficoll 70 (dashed line).

in the presence of 30% Ficoll 70. Given that the global tumbling is believed to contribute very little to the CW spectra, these changes could arise from viscosity effects on possible rotameric or conformational exchange in the complex.

3.4.1 Comparison between Spin-labeled Sites of the Specific Complex

Changes are evident between the spectra of the different spin-labeled sites, indicating that the spectra are sensitive to the spin-labeled location and backbone motions. Using the δ^{-1} as a semi-quantitative measure, the relative differences between the spin-labeled sites of the specific complexes was compared. It has been shown that δ^{-1} depends primarily on the rotational rate of the spin-labeled site.(*27*) Figure 3-5 illustrates the δ^{-1} for the spectra of each of the spin-labeled sites in the specific complex.

The spectra at site 131 possessed the highest δ^{-1} values. This is not surprising, however as this site is located on a loop region and is not entirely resolved in the crystal structure of the specific EcoRI complex.(*129*) Interestingly, the second most mobile spectra were obtained at site 180 which resides on the middle of an edge β-strand. Although site 180 is located on a more stable secondary structure (β-strand as opposed to a loop), previous work on the cellular retinol binding protein has shown that spin labels on edge β-strands possess very low order due to the fact that the strand is flanked by only one hydrogen-bonding neighbor.(*31*) Moreover, twisting of the β-strand as well as possible interactions with the neighboring amino acids contributes to the extent of order experienced by the spin label.

The spectra for sites 123 and 249 had similar δ^{-1} values, indicating that the mobility at each of these sites is similar. Sites 123 and 249 reside at different locations in EcoRI (arm versus main domain, respectively), however, they are both located on α-helices. The similarity

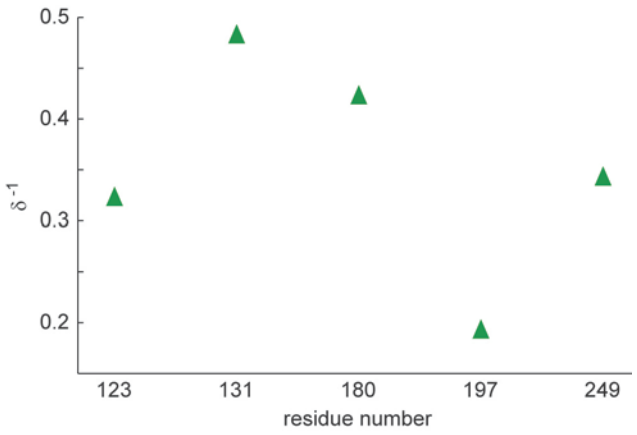

Figure 3-5. Inverse central line widths measured from the X-band spectra at the different spin-labeled sites in the specific EcoRI-DNA complex.

in δ^{-1} values between the two sites highlights the comparable behavior of the spin label and backbone dynamics at surface-accessible α-helical sites. The δ^{-1} values are also in agreement with those for helical surface sites of T4 lysozyme.(*21*) Lastly, site 197, located at the protein-DNA interface, possessed the smallest δ^{-1} value, indicating that the spin label is more immobile at this site than at any of the other sites.

3.4.2 Protein-DNA Interface: *Site 197*

The X- and W-band spectra for the three complexes at site 197 are shown in Figure 3-6. At this site there are clear differences between the spectra of the three complexes at both frequencies. The spectrum of the specific complex is indicative of an immobilized state. This immobility is evident in the g_{xx} and g_{zz} regions of the W-band spectra where in the specific complex each of the g-tensor peaks are resolved. This region is highlighted in gray in the W-band spectra of Figure 3-6. The spectra indicate an increase in mobility as one goes from the specific to miscognate to nonspecific complex.

To quantify the changes in the dynamics between the three complexes, the X-band spectra were simulated using the NLSL program of Freed and coworkers.(*15-16*) The simulations are overlaid on the experimental spectra in Figure 3-6 (simulated – dashed line). The parameters for the best fits to the spectra are presented in Table 3-2. The spectra were fit with two components, a mobile component with low order and an immobile, higher ordered component.

The mobile component is characterized by a rotational rate which increases from the specific to the nonspecific spectra. This component was fit using a rotational rate of 2.40×10^{7} s^{-1} in the specific complex spectrum. On the other hand, in the miscognate and nonspecific spectra

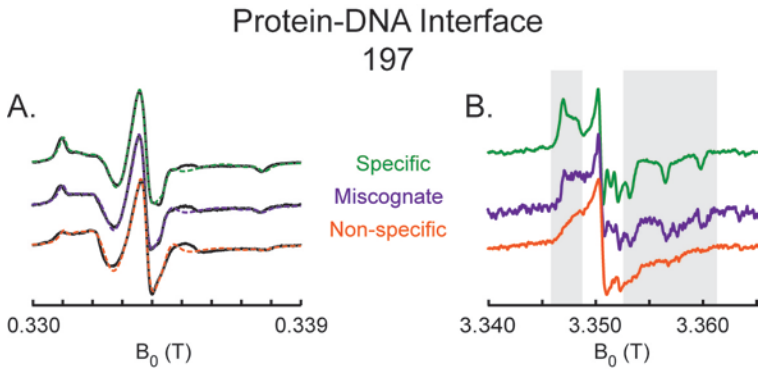

Figure 3-6. Room temperature X- and W-band spectra at site 197 in the specific (green), miscognate (purple), and nonspecific (orange) complexes. A. The X-band spectra were fit to simulation (dashed). B. The gray boxes in the W-band spectra highlight the g_{xx} and g_{zz} regions of the spectra which demonstrate changes in the different complexes for a particular spin-labeled location.

Table 3-2. NLSL Simulation Parameters

Mutant Complex	Comp.	$\overline{R}$ (s^{-1})	N	S_{20}	W (G)	β_D	%
197 Specific	1	2.40×10^7	14.5	0.26	1.04	30	67.9 ± 0.2
	2	3.31×10^6	6.6	0.80			32.1 ± 0.2
197 Miscognate	1	3.24×10^7		0.27	0.98	28	72.1 ± 0.2
	2	3.31×10^6		0.69			27.9 ± 0.4
197 Nonspecific	1	3.72×10^7		0.27	0.89	28	81.9 ± 0.2
	2	3.16×10^6		0.66			18.1 ± 0.6
123 Specific	1	4.27×10^7	105	0.45	1.11	39	64.8 ± 0.1
	2	1.70×10^7	11.0	0.45			35.2 ± 0.2
123 Miscognate*	1				1.28		58.3 ± 0.3
	2						41.7 ± 0.5
123 Nonspecific*	1				1.45		43.8 ± 0.3
	2						56.2 ± 0.4
131 Specific	1	7.76×10^8	38.9	0.30	0.20	12	19.3 ± 0.4
	2	6.17×10^8	47.9	0.30			80.7 ± 0.2
131 Miscognate*	1				0.20		20.6 ± 0.7
	2						79.4 ± 0.4
131 Nonspecific*	1				0.57		18.8 ± 0.6
	2						81.2 ± 0.3
180 Specific	1	3.09×10^7	72.4	0.00	0.21	45	80.5 ± 0.1
	2	1.00×10^7	89.1	0.00			19.5 ± 0.6
180 Miscognate*	1				0.34		86.6 ± 0.5
	2						13.4 ± 2.7
180 Nonspecific*	1				0.70		57.9 ± 0.7
	2						42.1 ± 1.3
249 Specific	1	2.51×10^7	112	0.26	0.79	41	79.1 ± 0.5
	2	1.07×10^7	30.2	0.00			20.9 ± 1.8
249 Miscognate*	1				0.92		68.4 ± 0.3
	2						31.6 ± 0.9
249 Nonspecific*	1				0.92		49.0 ± 0.1
	2						51.0 ± 0.2

*Parameters the same as for the specific complex (with the exception of line width and component populations.)

this mobile component was fit with a faster rotational rate of 3.24×10^{7} s^{-1} and 3.72×10^{7} s^{-1}, respectively. In addition to the rate increasing, the population of this component also increases from the specific to the nonspecific spectra. Order was needed to appropriately fit the spectra for all three complexes. The order of the mobile component did not vary significantly between the three complexes. The specific complex spectrum was fit with $S_{20} = 0.26$ and the noncognate spectra with $S_{20} = 0.27$.

To probe the correlation between the rotational rate and order parameter in the fitting procedure, the spectra were fit using a set of rotational rates and varying the order parameter for the best fit. Fits were also done using a set of order parameters and varying the rotational rate for the best fit. Through this procedure it was found that the change in the rotational rates of the mobile component between the three complexes is significant. The best fits were achieved using the same order parameter and letting the rotational rate vary between the spectra of the three complexes.

The second, immobile component at site 197 was less populated in all three complexes. The specific complex spectrum possessed the highest population of this component, which gradually decreased in the miscognate and nonspecific spectra. The spectra for the specific and miscognate complexes were fit using the same rotational rate of 3.31×10^{6} s^{-1} for this component. The nonspecific spectrum was fit with a slightly slower rotational rate of 3.16×10^{6} s^{-1}. Alternatively, the order parameter was the lowest in the nonspecific spectrum ($S_{20} = 0.66$). The order parameter then gradually increased from the miscognate ($S_{20} = 0.69$) to the specific complex spectrum ($S_{20} = 0.80$).

The correlation between the rotational rates and order parameter was also analyzed for the second component using the same fitting procedure as described above. The result of this

analysis was not as straightforward as for the first component. In particular, the immobile component could be fit using the same rotational rates, but different order parameters for the three complexes. However, successful fits were also found by varying the rotational rate and holding the order parameter constant. Subtle changes in the spectra, due to different rotational rates and order, as well as the correlation between these two parameters convolutes the analysis of the immobile component. For this reason, future work will involve simulating fits to variable temperature CW spectra. In this way the contributions of the rotational rate and order to the change in the spectra of the three complexes can be probed.

The spectra and values used for the correlation analysis of the $\overline{R}$ and S_{20} parameters are shown in Figure 3-7 for both components 1 and 2. The best fits for each set (i.e., $\overline{R}$ constant and S_{20} varied for component 1) are boxed. The correlation between $\overline{R}$ and S_{20} can be seen from the fact that decent fits can be obtained for different combinations of the two parameters.

Attempts were also made to fit the 197 data by keeping ordering and rotational rates the same and changing the populations. Satisfactory fits to the X-band spectra were not obtained as shown in Figure 3-8. Here, the experimental spectrum for all three complexes are shown in black (specific - top, miscognate - middle, nonspecific - bottom). Overlaid onto each of these spectra are simulated fits (dashed), using the best fit parameters from the specific (green), miscognate (purple), or nonspecific (orange) simulations. Only the line width and populations of the components was allowed to vary in the fits. It can be seen in this figure that as the spectra change from the specific to the nonspecific complex the fits become increasingly worse.

In addition to performing CW analyses at site 197, the DEER experiment was performed to extract distance constraints across the protein-DNA interface region in all three complexes. The background subtracted DEER time domain signal and corresponding distance distributions

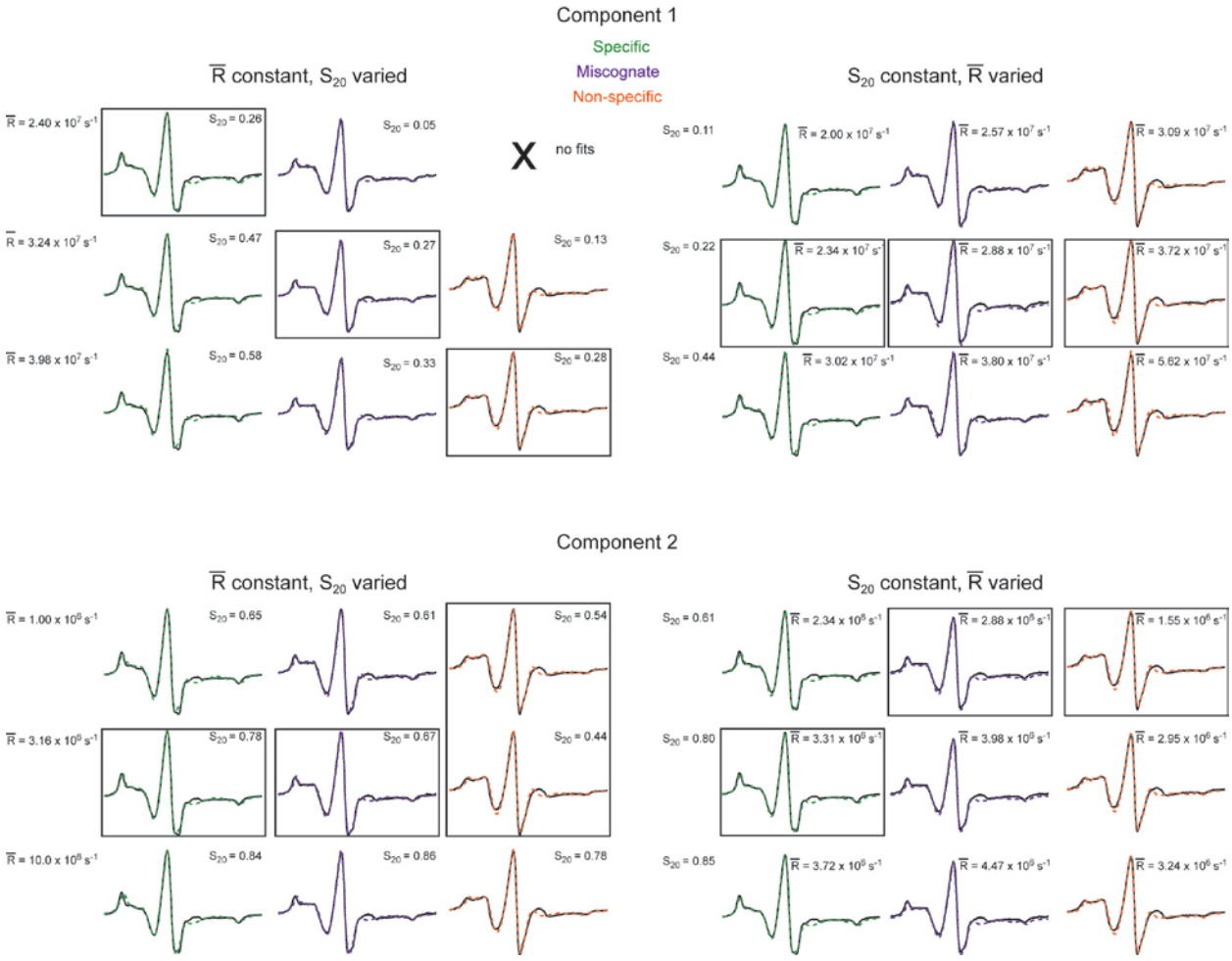

Figure 3-7. Correlation analysis of the $\overline{R}$ and S_{20} parameters for components 1 (top) and 2 (bottom) for the 197 spectra. The simulated results (dashed) are overlaid on the experimental spectra. The correlation of the two parameters is evident in the fact that reasonable fits could be obtained using different combinations of $\overline{R}$ and S_{20}. The best fits within a set are boxed.

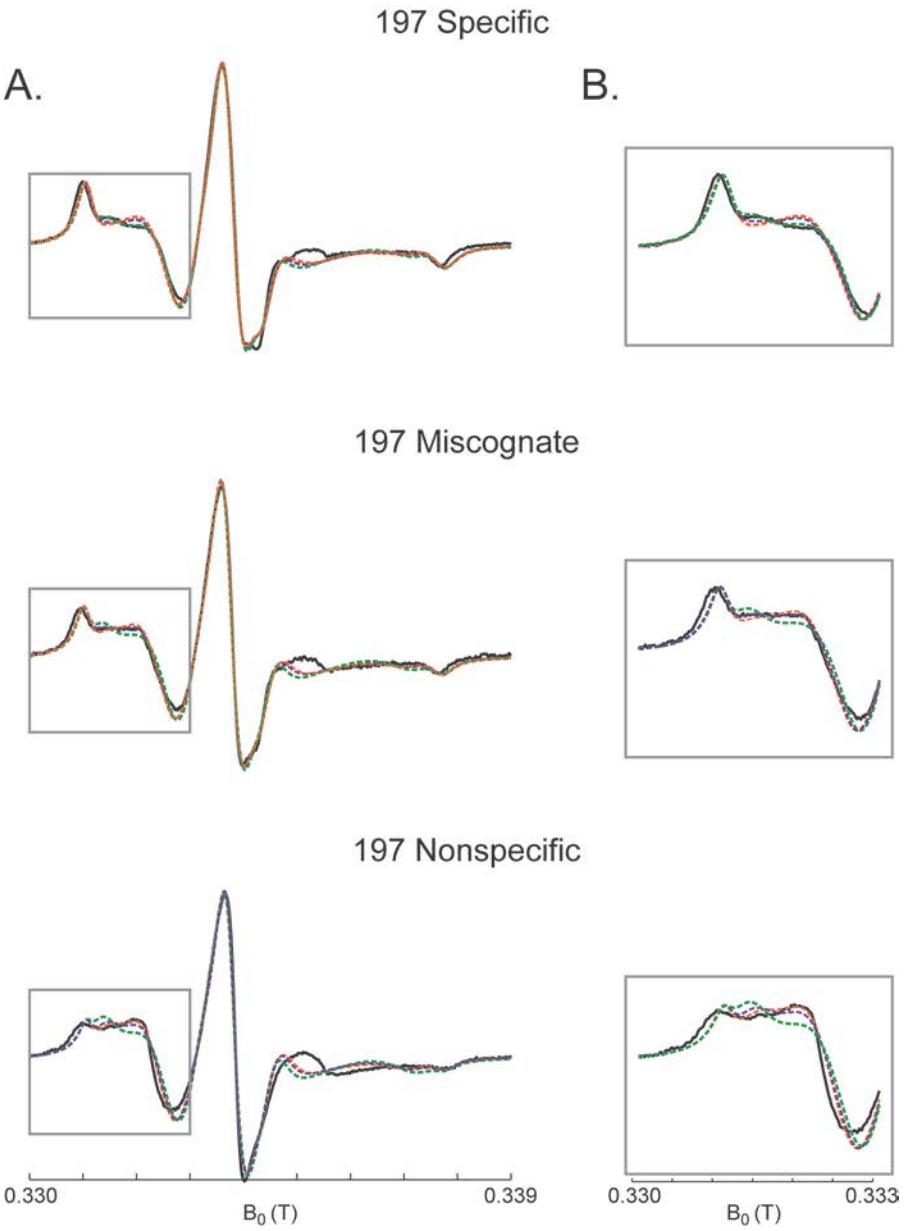

Figure 3-8. A. Experimental spectra for the specific (top), miscognate (middle) and nonspecific (bottom) complexes are shown in solid black. Simulations were performed using the best fit parameters from the specific (green) , miscognate (purple), and nonspecific (orange) fits for each of the three sets of experimental spectra allowing only the line width and percentage of the components to vary (dashed lines). B. To highlight the changes between the fits, the low field portion of the spectra has been expanded.

are shown in Figure 3-9. As observed in the distance measurements at other spin-labeled sites the average distance is the same for all three complexes. In this case, the average distance is 4.0 nm for all three distance measurements. Additionally, although the specific and miscognate complexes possess distance distributions with similar standard deviations, the nonspecific distance distribution is significantly broader. This is also evident in the DEER time domain for the nonspecific complex which shows a damping of the modulation signal due to this increased distribution of distances.

3.4.3 Surface-Accessible Sites: *Arm Region (Sites 123, 131, 180)*

The X- and W-band experimental and simulated X-band spectra for sites 123, 131, and 180 in the three complexes are shown in Figure 3-10. The sets of spectra (specific, miscognate, nonspecific) for each spin-labeled site are visibly different, indicating that the spectra are sensitive to the local environment and secondary structure of the spin-labeled site. However, differences between the spectra of the three complexes at a given spin-labeled site are smaller. Slight differences are present, however, they are not as drastic as at site 197, nor do they follow the same trend within the complexes.

At site 123, the X-band spectra were fit with two components, a mobile and an immobile component. The immobile component is evident in the low-field shoulder of the spectra (highlighted by a dashed line). Significantly, the spectra for all three complexes were fit using the same parameters. The only parameters that varied between the fits were the line width and population of the two components. The mobile and immobile components were fit with rotational rates of 4.27×10^{7} s^{-1} and 1.70×10^{7} s^{-1}, respectively. An ordering potential of 0.45 was used to fit both components.

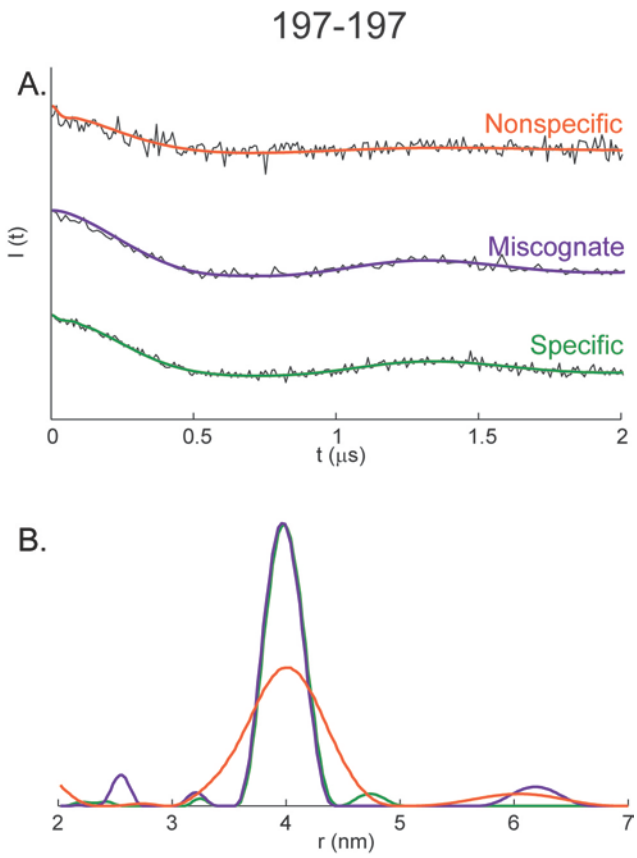

Figure 3-9. A. The background subtracted time domain signal for the 197-197 intermonomer distance measurement performed using the DEER experiment. B. The experimental distance distribution extracted from the time domain signal using DeerAnalysis2009.(*127*) The data was fit using Tikhonov regularization.

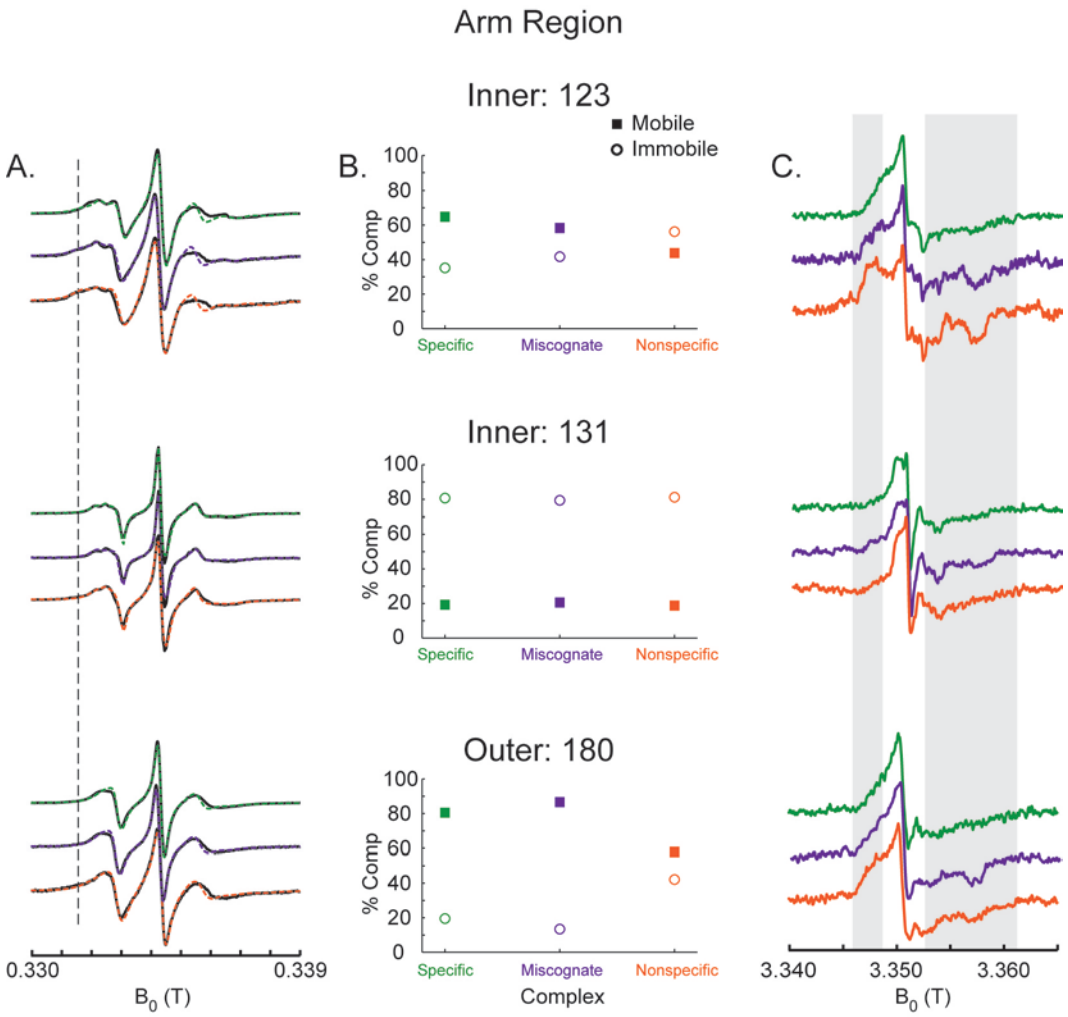

Figure 3-10. Room temperature X- and W-band spectra at sites 123, 131, and 180 in the specific (green), miscognate (purple), and nonspecific (orange) complexes. A. The X-band spectra were fit to simulation (dashed). The dashed vertical line in the X-band spectra is used to guide the eye to the immobile component that is present in each of the spectra. B. The populations of the mobile (solid squares) and immobile components (open circles) are plotted for each of the three complexes at each site. C. The gray boxes in the W-band spectra highlight the g_{xx} and g_{zz} regions of the spectra which demonstrate changes in the different complexes for a particular spin-labeled location.

Two components were also evident at site 180 and like at site 123, the X-band spectra for all three complexes could be fit with the same set of parameters. The dynamics of the two components are slightly slower at site 180, possessing rotational rates of 3.09×10^{7} s^{-1} and 1.00×10^{7} s^{-1} for the mobile and immobile component, respectively. Attempts were made to fit the spectra with order; however, this did not improve the quality of fit. Thus, the spectra were fit using the anisotropic Brownian diffusion model in which no ordering potential is needed.

At both sites 123 and 180 the population of the immobile component in the spectra increased from the specific to the nonspecific complex. This trend can be seen in the center panel of Figure 3-10 where the populations of the mobile (solid squares) and immobile components (open circles) have been plotted. Compared to the height of the symbols in Figure 3-10, the error bars for the individual populations are negligible; therefore they are excluded from the plots. Additionally, in the W-band spectra of the nonspecific complexes, the g_{xx} and g_{zz} regions (highlighted in gray in Figure 3-10) are more resolved, indicative of an increase in the immobile component in these complexes.

The dynamics at site 131 were slightly different compared to sites 123 and 180. As at the other arm sites there are two components at site 131, however, the significant difference between these components arises from a change in the polarity in the local environment. This is observed in the increase of the hyperfine splitting between the two components based on the X-band spectral simulation. The order parameter is the same for both components, and although the rotational rates differ slightly it is not significant (7.76×10^{8} s^{-1} versus 6.17×10^{8} s^{-1}). Additionally, the populations of the two components are the same in all three complexes, within the error of the populations as provided by the fitting program. A possible third component is evident in the high-field shoulder of the spectra (mainly in the nonspecific complex). However,

fitting one spectrum with three components is complicated and can result in large errors in the fitting parameters. Even for simple systems, such as T4 lysozyme, it has been shown that to thoroughly investigate the dynamics and order at spin-labeled sites, experimental spectra at multiple frequencies was needed. In addition, successful simulated fits to the CW spectra required multiple components.(*30, 32*) The origin of these components is convoluted due to the possibility of rotameric exchange of the spin label or conformational exchange of the system. The presence of an immobile component in the W-band data is difficult to observe at site 131 due to the high mobility at this site.

Interestingly, although site 131 resides on a loop and site 180 on a β-strand, order was needed to fit the 131 CW data, but not for 180. Although the rotational rates of the spin label are significantly faster at site 131, the presence of charged local side chains (i.e. K130, D133, and Q134) as well as the proximity to the DNA may induce a larger restriction on the spin label at site 131. Indeed the fact that two components were present with differing polarities indicates that perhaps the spin label is sampling different environments of the surrounding side chains.

In the case of 180 its nearest neighbor residue is a non-hydrogen bonding neighbor (NHB). As shown in the work based on CRBP the side chain of a NHB neighbor will tend to orient itself towards the spin label, with beta-branched amino acids providing more of a crowding effect. However, the NHB neighbor of 180 is an asparagine residue, therefore less interaction between the NHB neighbor and the spin label are expected, resulting in a less restricted environment.

X-band CW spectra were also collected at lower temperatures to probe the behavior of the two components as the temperature is decreased. In addition to the 293 K data, spectra were collected from 283-253 K in 10 K increments for the sites in the arm region in all three

complexes. These variable temperature spectra are shown in Figure 3-11. As the temperature was decreased the population of the immobile component increased at all sites. The immobile component is highlighted in Figure 3-11 by a dashed vertical line in each spectral set. The immobile component is clearly more populated in the lower temperature spectra of the noncognate complexes as compared to those of the specific complex.

3.4.3.1 *Main Domain (Site 249)*

The X- and W-band experimental and simulated X-band spectra for the three complexes spin-labeled at site 249 in the main domain are shown in Figure 3-12. Similar to the spin-labeled sites in the arm region, the spectra for the three complexes at site 249 vary only slightly. The only major difference is that the noncognate spectra possess more of an immobile component as shown by the dashed vertical line in the X-band spectra and gray region in the W-band spectra. This is similar to the trend seen at the other sites.

As at sites 123 and 180, the 249 X-band spectra could be fit using the same parameters for all three complexes and varying only the line width and populations of the components. The 249 spectra were fit with two components possessing rotational rates of 2.51×10^{7} s^{-1} and 1.07×10^{7} s^{-1}. The mobile component was fit using an order parameter of 0.26; however, the order parameter had a negligible effect on the fit to the immobile component, thus no order parameter was used. The S_{20} value for the mobile component is smaller than for site 72 on T4 lysozyme (S_{20} = 0.47). For this site it resides on the middle of an α-helix, however, site 249 of EcoRI is on the N-terminus of the helix. Thus, the reduced order for the mobile component at 249 may be attributed to the increase in backbone fluctuations at the end of the helix as opposed to the center. Again, the population of the immobile component increased as the complexes

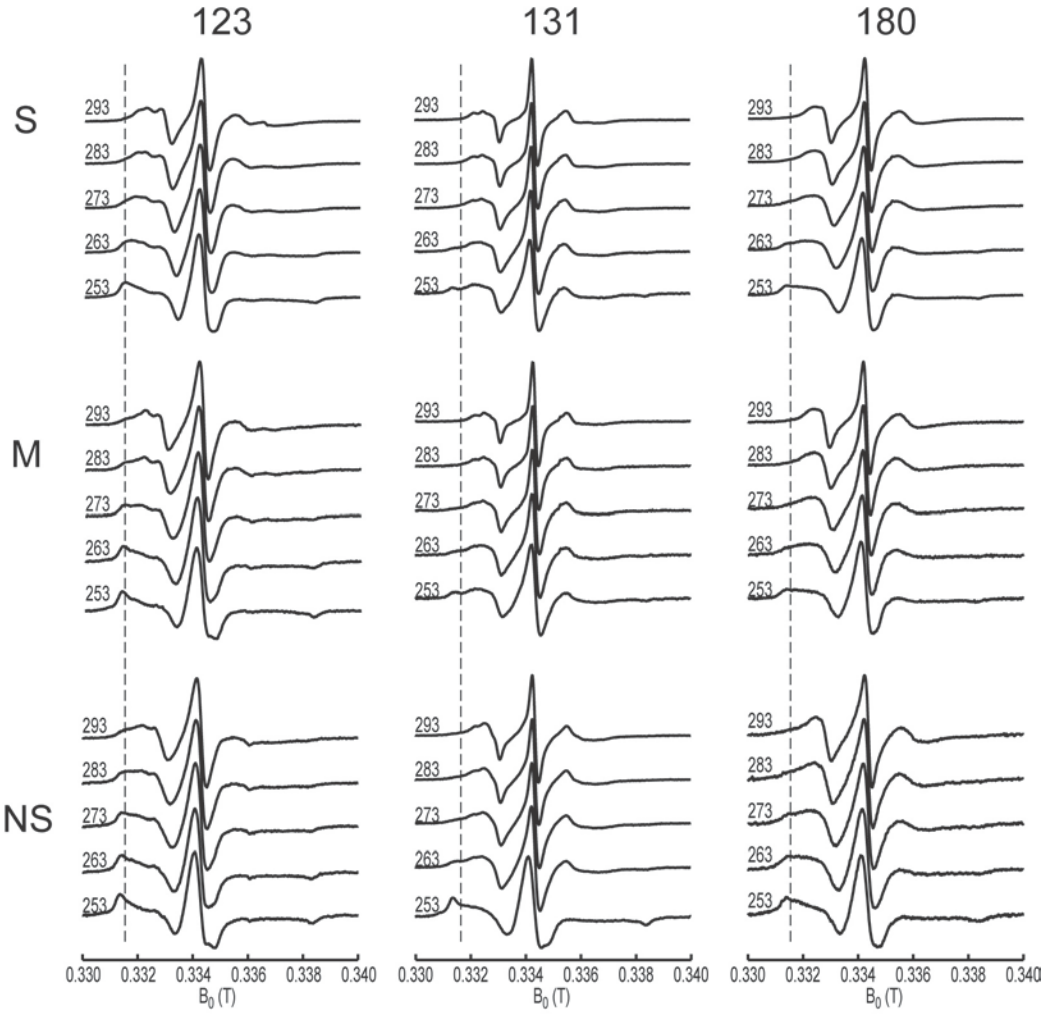

Figure 3-11. Variable temperature (253 – 293 K) spectra for each of the spin-labeled sites in the arm region in the three EcoRI complexes. The dashed vertical lines are used to guide the eye to the immobile component that is present in each of the spectra and increases as the temperature is decreased.

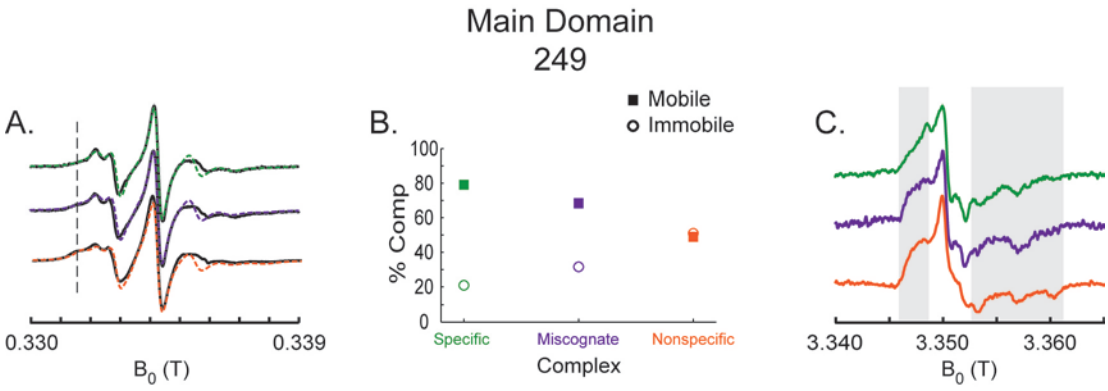

Figure 3-12. Room temperature X- and W-band spectra at site 249 in the specific (green), miscognate (purple), and nonspecific (orange) complexes. A. The X-band spectra were fit to simulation (dashed). The dashed vertical line in the X-band spectra is used to guide the eye to the immobile component that is present in each of the spectra. B. The populations of the mobile (solid squares) and immobile components (open circles) are plotted for each of the three complexes at each site. C. The gray boxes in the W-band spectra highlight the g_{xx} and g_{zz} regions of the spectra which demonstrate changes in the different complexes for a particular spin-labeled location.

changed from specific to nonspecific, this variation in population is shown in the center panel of Figure 3-12.

Attempts were made to fit the X and W-band data for site 249 simultaneously using the slowly relaxing local structure or SRSL model. This model takes into account the slow reorientation of the ordering potential due to slower motions on the ESR timescale such as backbone motions. Although reasonable fits could be obtained at X-band, the fits to the W-band data were not successful. By using different fractions of the two components present in the spectra, the quality of fit to the W-band data could be improved, however, the quality of fit to the X-band data decreased. Ultimately, successful fits to both the X- and W-band data using the same set of parameters and component populations could not be achieved. This issue was also observed for T4 lysozyme using multifrequency CW spectra collected at 9 and 250 GHz frequencies.(*32*) Only until experiments were analyzed at four frequencies (9, 95, 250 GHz) and using three components could the T4 lysozyme spectra be fit successfully using the same fractions for each of the components at all frequencies.(*30*)

3.5 DISCUSSION

In this work multifrequency CW-ESR was used to probe the subtle changes between related EcoRI-DNA complexes. The $\Delta C_p°$ values indicate that the noncognate complexes form "looser" complexes. In addition, phosphate contacts formed between EcoRI and the DNA backbone form a different pattern in the miscognate complex, missing key contacts that contribute to the high binding affinity of the specific complex.(*117, 120, 129, 132-133*) As the residues involved in these contacts reside in the arm region of EcoRI it is believed that these arms play a role in the

binding specificity of the endonuclease. Previous DEER experiments have shown that although the arms are oriented similarly in the all three complexes, they may be more flexible in the noncognate complexes due to a broader distance distribution.(*54*) The goal of this work was to identify the region that is most sensitive to changes in the complexes by analyzing the change in dynamics at the various spin-labeled sites.

3.5.1 Changes between Complexes Most Sensitive at the Protein-DNA Interface

Differences in dynamics and order as a function of DNA sequence was observed for site 197 only. The simulated fits to the 197 X-band spectra were performed using two components. The mobile component present in all three complexes possessed a rotational rate that increased from the specific to the nonspecific spectra. Similar order parameters were used to fit this component in all three complexes. Together, this indicates that as the complexes change from the specific to the nonspecific, the dynamics of the mobile component of the spin label increases.

An immobile component was also present in the spectra of the three complexes at site 197. The change in dynamics and order between the spectra of the three complexes are more convoluted for this component. Similar rotational rates were used to fit all three spectra; however, the rotational rate used to fit the nonspecific spectrum was slightly slower. Alternatively, the order parameter used to fit this component decreased from the specific to the nonspecific spectrum. From these fits it would appear that the order of the spin label environment changes within the three complexes. However, these results are convoluted due to the correlation of the rotational rates and order parameter. Therefore, future work will be done to probe the change in dynamics and order of this component between the three complexes.

At site 197 the spin label is in close contact with the second and third flanking residues cytosine and guanine, respectively. Although the DNA backbone is hydrophilic, the bases of DNA are hydrophobic. These bases in combination with the surrounding hydrophobic residues (L136, M137, A138, and A139) all contribute to a hydrophobic pocket surrounding the spin-labeled site. This pocket could give rise to the restricted immobile component due to interactions between the nitroxide moiety and these side chains and bases. Possible wagging of the spin label due to rotations about χ_2 would move the spin label away from the hydrophobic pocket thereby giving rise to the second, mobile component also seen in the CW spectra.

The increase in the dynamics and population of the mobile component in the noncognate complexes may indicate a partial increase in the conformational freedom of the spin label in these complexes. This would correlate with the $\Delta C_p°$ as well as the previous and current DEER results. In the case of the 197-197 DEER distance measurements performed here, the specific and miscognate complexes possessed similar distributions; however the nonspecific distribution was significantly broader.

At the sites in the surface-accessible arm region and main domain, the only significant difference among the spectra of different complexes arose in the population of the mobile and immobile components in the spectra. In particular, the noncognate complexes possessed a higher population of the immobile component as indicated by the simulations of the room temperature X-band spectra as well as visually in the variable temperature spectra. Indeed, each of the sets of data was fit using the same dynamics and order for all three complexes, varying only the line width and populations of the components. Due to the presence of multiple components and the fast dynamics at site 131, less information could be extracted about similar mobile and immobile components at this site.

The CW comparison between the different EcoRI complexes indicates that although there are indeed differences between the complexes at the protein-DNA interface, the surface-accessible arm and main domain regions are not as sensitive to the changes in the conformational freedom of the complexes. This could be due to the fact that the dynamics of the surface-accessible spin-labeled sites is so mobile initially, that changes of the complex upon binding different DNA sequences are not significantly detected. At site 197 the spin-labeled site is so restricted (from the immobilization of the spin label due to interactions with local side chains and the DNA), that changes in the dynamics upon binding different sequences of DNA are significant and detectable.

3.5.2 Origin of the Immobile Component in the Arm and Main Domain

The origin of the different components in the EcoRI-DNA spectra could arise from different rotamers of the spin label.(*90-91*) However, it could also arise from different conformations of the EcoRI-DNA complex in solution. Hubbell and coworkers have recently demonstrated that the two possibilities can be distinguished using osmolytes and high pressure.(*144-146*) This is a matter of future research. However, 60 ns molecular dynamics (MD) simulations of the spin-labeled specific EcoRI-DNA complex indicate that the spin labels at sites 131, 180, 197, and 249 sample a variety of orientations. Figure 3-13 shows a snapshot from one of the simulations for each of the spin-labeled sites. The snapshots are shown for every 20 ps of a 3 ns trajectory. It can be seen from these snapshots that the spin label samples a wide variety of local environments. However, the simulations show no indication of two distinct orientations that might give rise to the two components observed in the CW spectra. It should be noted, however,

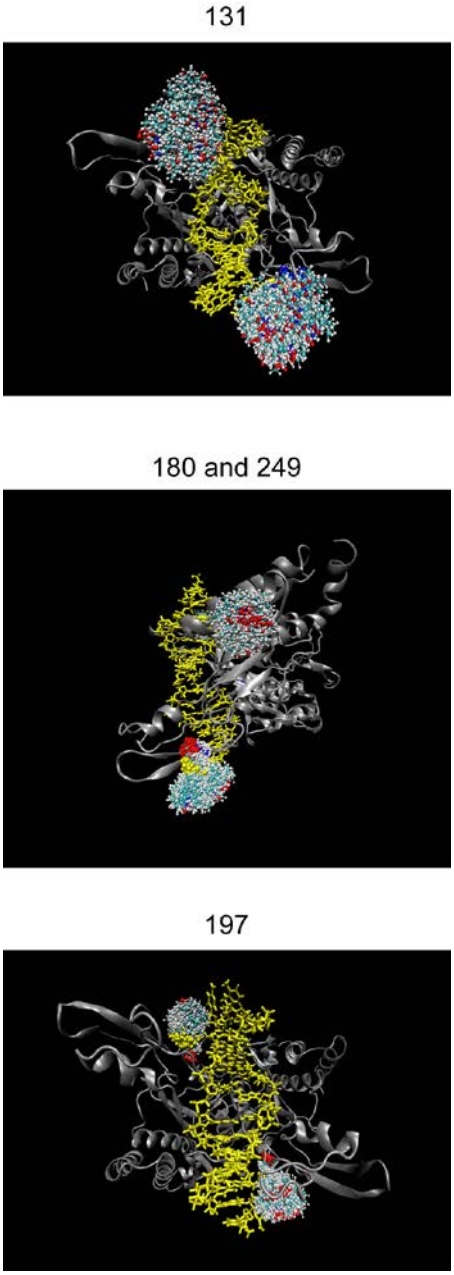

Figure 3-13. Snapshots of the MD simulations of the specific EcoRI-DNA complex with spin labels located at 131, 180 and 249, and 197. A side-view of the 180-249 system is shown.

that these simulations were performed at 300 K. Although no distinct groups of conformers are resolved at this temperature, this may not be the case as the temperature is decreased.

The trend of an increased population of the immobile component in the noncognate complexes at the surface accessible spin-labeled sites could be due to a conformational exchange within each of the three complexes. Being that the immobile component was more highly populated in the noncognate complexes, these complexes may sample a larger number of conformational substates than the specific complex. This conformational exchange may also be reflected in the increase in the standard deviation of the noncognate distance distributions from the DEER experiment.

In summary, measuring the dynamics and order of different spin-labeled sites in the EcoRI-DNA complex has shed light on the localized region of interest for probing the conformational-vibrational changes that occur between the different EcoRI complexes. Indeed, the changes observed in both the X- and W-band spectra at the protein-DNA interface (site 197), indicates that this region is most sensitive to the changes that occur between the protein-DNA complexes. This work demonstrates that sensitivity to the changes between complexes may lie in the intrinsic dynamics of the spin label and the backbone at the spin-labeled site.

3.6 ACKNOWLEDGMENTS

The MD and ESR studies were supported by National Science Foundation (MCB 0842956) grant to S. S. and L. J-J. Generation of mutant proteins and spin labeling were supported by National Institutes of Health MERIT (5R37-GM029207) grant to L. J-J. The simulations were also supported by the NSF through TeraGrid resources provided by the Pittsburgh Supercomputing

Center under grant number TG-CHE100114 and the University of Pittsburgh Center for Simulation and Modeling. J. L. S. thanks Ralph Weber and the Bruker Biospin facility for the use of and instruction on their W-band spectrometer.

4.0 MEASURING CU^{2+}-NITROXIDE DISTANCES USING DOUBLE ELECTRON-ELECTRON RESONANCE AND SATURATION RECOVERY

4.1 ABSTRACT

In this work, distance measurements were obtained between a bound Cu^{2+} and a spin label on two polypeptides of differing length. The distance measurements were performed using both the double electron-electron resonance (DEER) and saturation recovery experiments. Distance distributions obtained from the DEER results provided the average distance and distribution of distances for each peptide. An average distance was also obtained for each peptide using the relaxation-based saturation recovery experiment. Predicted average distances for the relaxation-based method, $<r_{ESR}>$, were calculated using the distance distributions from the DEER experiment. The predicted $<r_{ESR}>$ values were found to be similar to the average distances measured by saturation recovery, both of which were biased to shorter values compared to the DEER results. The standard deviations of the distance distributions were found to have a significant effect on the average distance measured by saturation recovery. This work highlights the advantage of using the DEER experiment to measure metal-nitroxide distances in that the average distances measured are less biased than in relaxation-based techniques.

4.2 INTRODUCTION

Recently, Cu^{2+} has been highly investigated by electron spin resonance (ESR) due to its importance in the folding/misfolding of many peptides. It has been suggested, through ESR studies, that Cu^{2+} plays a role in the structure and aggregation of several amyloid-forming peptides such as Aβ (*147-151*), α-synuclein (*152-153*), tau (*154*), amylin (*155*) and the prion protein.(*156-158*) Additionally, the inhibitory effect of Cu^{2+} on ligand-gated ion channels such as the glycine receptor has been probed. The role that Cu^{2+} plays as an enzymatic cofactor has also been investigated using ESR. (*159-164*)

Cu^{2+}-Cu^{2+} distance constraints have been utilized to pinpoint metal binding sites in a protein-DNA complex.(*165*) This was done using Cu^{2+}-Cu^{2+} distance measurements based on the double electron-electron resonance (DEER) experiment.(*5, 8, 166-171*) Cu^{2+}-nitroxide measurements are possible as well, where the distance between a Cu^{2+}-bound center and a spin-labeled site is measured.(*167, 169, 172-173*) The presence of the nitroxide spin label is advantageous because it enables several distance measurements to be made as the spin-labeled site can be altered. A limitation of this method, however, is that the spin-labeled site must not perturb the structure or function of the system.

Relaxation-based experiments, such as inversion or saturation recovery, can also be used to measure distances between a metal center and spin label. In these experiments, the relaxation rate of the slower relaxing spin (spin label) is enhanced by the faster relaxing spin (metal) to which it is coupled.(*13*) This affect is exploited to measure the average distance between the two electron spins. This distance measurement technique may prove beneficial in metal-binding systems where the ESR signal of the metal is broader and thus weaker. In the past several years, saturation recovery experiments have been primarily used to measure distances in Fe-containing

systems.(*81-85*) However, as pointed out previously, there are many biologically relevant systems that bind Cu^{2+}, making the use of saturation recovery experiments in these systems of interest.

The DEER experiment is advantageous in that it not only provides an average distance between the electron spins, but a distance *distribution* can also be measured from the experimental results. These distributions provide insight into the mobility of the system based on the broadness of the distribution, as well as show any bias in the distribution towards shorter or longer distances. Indeed previous works on model peptide systems have shown the DEER experiment to be sensitive to the change in length as well as flexibility of the peptide.(*66-67*) In the case of relaxation-based experiments, only the average distance between the two coupled spins is measured. Additionally, the average distance is likely to be biased towards shorter distances as the relaxation-based distance measurements go as r^{-6}.(*174*) Therefore, it is of interest to compare the DEER and saturation recovery techniques to probe the affect the distance distribution has on the average distance measured by the saturation recovery experiment. Also, the applicability of a Cu^{2+}-based saturation recovery experiment versus the DEER experiment should be investigated for distances longer than 20 Å.

In this work, two polyalanine peptides (3AK and 4AK) were constructed with a Cu^{2+}-binding center (PHGGGW) and a spin-labeled residue on each peptide. The two peptides differed by the number of residues separating the bound Cu^{2+} and the spin label. Distance measurements were performed on the peptides using the DEER and saturation recovery experiments at low temperatures. A comparison was made between the two methods on the average distances obtained for the two peptides. Also, the effect of the distance distribution on the average distance obtained by the relaxation-based technique was assessed.

4.3 METHODS

4.3.1 Sample Preparation

Two polyalanine peptides: PPHGGGWPXXXCXA (3AK) and PHGGGWPXXXXCXA (4AK) where X=AAAAK, were synthesized, spin-labeled, and purified at the University of Pittsburgh peptide synthesis facility. In these peptides the PHGGGW sequence is a Cu^{2+} binding site.(*157-158*) In both peptides the methanethiosulfonate spin label was covalently attached to the cysteine residue using site-directed spin labeling.

For the DEER experiments 1-1.5 mM solutions of each peptide was prepared in 30 mM N-Ethylmaleimide (NEM) buffer. An excess of isotopically enriched $^{63}CuCl_2$ was added to the solutions for a 3:1 Cu^{2+}:peptide ratio to ensure sufficient binding of the Cu^{2+}. Saturation recovery experiments samples were prepared in a buffer of 10 mM KCl and 25 mM NEM solution at pH 7.6 resulting in a peptide concentration of 1 mM. The relaxation experiments were performed in the presence and absence of coordinated Cu^{2+}. In the absence of Cu^{2+}, Zn^{2+} was bound to provide a diamagnetic metal-bound peptide complex. In each case a 3 molar excess of $^{63}CuCl_2$ or $ZnCl_2$ was added to each of the samples. The samples were degassed to 5.5 x 10^{-4} Torr and flame sealed in quartz 3 mm (O.D.) tubes. The DEER and saturation recovery samples were prepared in 30% glycerol to form a glass upon freezing.

4.3.2 ESR Spectroscopy

All ESR experiments were performed on a Bruker EleXsys CW/FT X-band ESR spectrometer using both the Bruker MD5 (DEER and saturation recovery) or MS3 (saturation recovery)

resonators. Temperatures were maintained using an Oxford ITC 503 temperature controller and CF935 dynamic continuous flow cryostat. Liquid helium was used to maintain temperatures below 80 K while liquid nitrogen was used for experiments at 80 K.

DEER experiments were performed at 20 K using the four-pulse sequence: $(\pi/2)_{\upsilon 1}$-τ_1-$(\pi)_{\upsilon 1}$-T-$(\pi)_{\upsilon 2}$-τ_2-$(\pi)_{\upsilon 1}$-τ_2. The observer $(\pi/2)_{\upsilon 1}$ and $(\pi)_{\upsilon 1}$ pulses were 8 and 16 ns respectively, and the pump $(\pi)_{\upsilon 2}$ pulse was 12 ns for both peptide samples. A step size of 8 ns was used and the integrated echo intensity was collected for 256 points. A two-step phase cycling (+x, -x) was carried out on the first $\pi/2$ pulse. Proton modulation was averaged by adding traces at four different τ_1 values, starting at 160 ns and incrementing by 18 ns. The pump pulse began 40 ns before the echo so the zero time could accurately be determined. The pump pulse was located at the maximum of the nitroxide spectrum with the observer pulse applied at three different frequency offsets in the Cu^{2+} spectrum of 280, 364, and 448 MHz higher.

Echo-based saturation recovery experiments were performed at 80 K. A picket fence pulse sequence was used to detect the nitroxide T_1: $\pi/2$-τ_1-$\pi/2$-τ_1-$\pi/2$-τ_2-$\pi/2$-τ_2-π, with 4 ns $\pi/2$ and 8 ns π pulse lengths. A pulse separation of 40 ns was used for τ_1 and 300 ns for τ_2. The echo-forming pulses were stepped out by 10000 ns for 256 points. The 3AK Cu^{2+} T_m values were measured using the echo decay experiment. The $\pi/2$ and π pulses were 32 and 64 ns in length, respectively, to reduce the ESEEM contribution to the decay. A 32 ns step size was used and the decay was collected for 128 points. The recovery and echo decay signals were fit using the curve fitting toolbox in Matlab (The Mathworks Inc.).

4.4 RESULTS

4.4.1 Double Electron-Electron Resonance Experiments

Cu^{2+}-nitroxide distance measurements were performed on the two polyalanine peptides, 3AK and 4AK, using the DEER experiment. Short pulses were used in the experiment to increase the excitation bandwidth and thus reduce the orientational effects from Cu^{2+}. To verify that the orientational effects were sufficiently reduced, three DEER experiments were performed for each peptide with the observer pulse positioned at three different frequency offsets from the pump pulse. In each experiment, the pump pulse was applied at the center of the nitroxide spectrum. The observer pulse was applied at different magnetic fields in the Cu^{2+} spectrum for the three experiments.

The raw DEER data is shown in Figure 4-1A for both 3AK (top) and 4AK (bottom). For the 3AK peptide, the background subtracted time domain signals possess nearly identical modulation frequencies irrespective of the frequency offset. Similar results are seen for the 4AK sample (Figure 4-1B). As expected, the modulation depth decreases as the observer pulse is positioned further into the $g_{||}$ region of the Cu^{2+} spectrum. The modulation depth of the 280 MHz offset data was 0.86 while the 448 MHz offset data possessed a modulation depth of only 0.95. This is due to a smaller population of spins being excited by the observer pulse in the $g_{||}$ region of the Cu^{2+} spectrum.

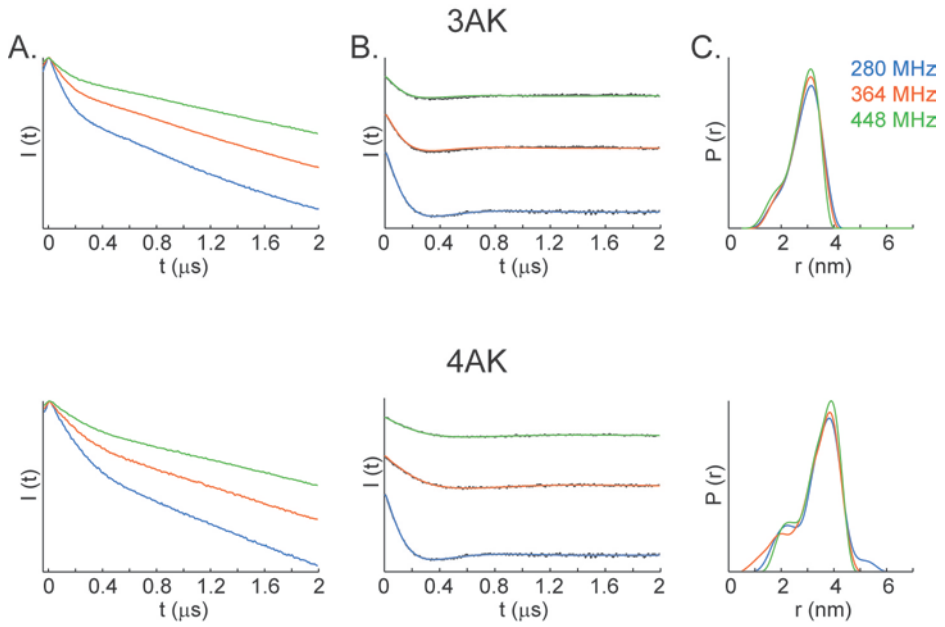

Figure 4-1. Cu^{2+}-nitroxide DEER data collected for 3AK and 4AK at three different frequency offsets of the observer and pump pulse: 280 MHz (blue), 364 MHz (orange), 448 MHz (green). A. Raw DEER data. B. Background subtracted time domain signals; background subtraction was done using DeerAnalysis2009. C. Distance distributions were constructed using the Tikhonov regularization method.

The orientational selectivity of these experiments is expected to be low due to the inherent mobility of Cu^{2+} as well as the spin label.(*167, 169*) Indeed, Cu^{2+}-nitroxide 3AK DEER simulations, based on the model developed by Yang *et al.*, show little orientational selectivity. These simulations (red dashed line) are shown in Figure 4-2 where they are compared to the experimental time domain data (black solid line). Starting with the same relative orientation of the Cu^{2+} and nitroxide g-tensors, the best fits were achieved using similar average distance and standard deviation values for all frequency offsets.

The Cu^{2+}-nitroxide distance distributions were extracted using the Tikhonov regularization approach in DeerAnalysis2009, shown in Figure 4-1C.(*80*) As expected for experiments lacking orientational effects, similar distance distributions were obtained at each of the frequency offsets for 3AK results as well as for the 4AK results. The 280 MHz frequency offset DEER data was used for further analysis due to the higher signal to noise ratio achieved in this experiment (observer pulse position at the maximum of the Cu^{2+} spectrum or the $g_{\perp}$ region). The best fit for the 3AK time domain signal yielded a distance distribution with an average distance of 29 Å and standard deviation of 6 Å. The 4AK distance distribution possessed a longer average distance (34 Å) and significantly broader distribution (standard deviation = 8 Å). The increase in average distance and distribution reflects the increased length and flexibility of the longer 4AK peptide chain. The distance increase between 3AK and 4AK is consistent with the expected pitch of an α-helix (5.4 Å).(*175*)

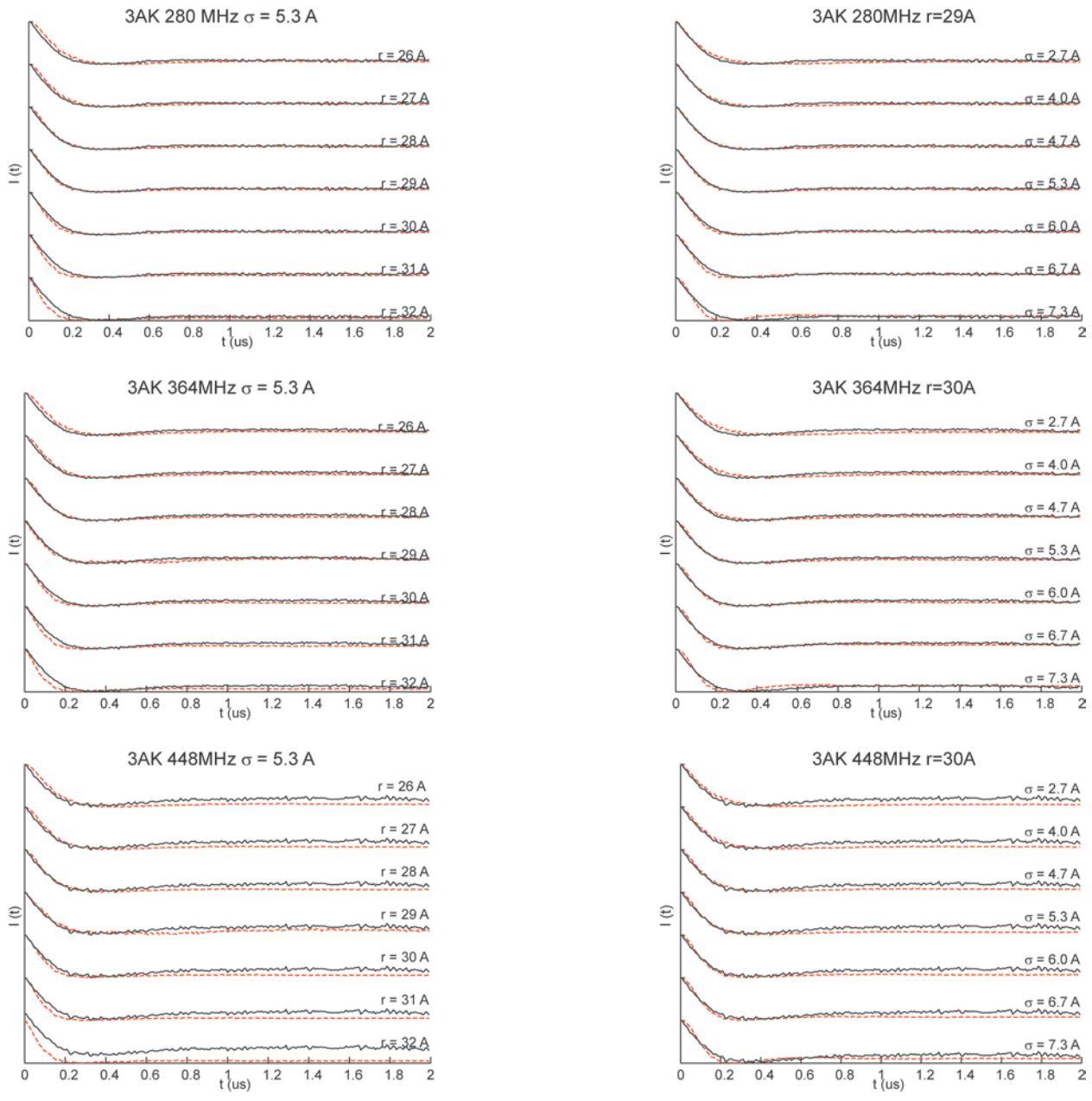

Figure 4-2. Cu^{2+}-nitroxide DEER simulations (red dashed line) for the 3AK peptide based on the model developed by Yang *et al.* The data were simulated using the same orientation between the g-tensors of the Cu^{2+} and spin label. The best fits were achieved at each frequency offset using similar average distances (r) and standard deviations (σ).

4.4.2 Saturation Recovery Experiments

Saturation recovery experiments were also performed on the two polypeptides to measure the difference in the nitroxide T_1 with Cu^{2+} and without Cu^{2+}. Several mechanisms contribute to the nitroxide T_1. These include spin-rotation interactions, electron-nuclear dipolar interactions, spin diffusion, and Heisenberg spin exchange.(*176*) In the presence of Cu^{2+} the electron-electron dipolar interaction provides yet another mechanism. If the contributions to T_1 from the former mechanisms are the same in the absence and presence of Cu^{2+}, the difference in T_{1s} and T_{1s}^0 is a measure of the electron-electron dipolar interaction. The contribution to this electron-electron dipolar relaxation can arise from the fast relaxation of the Cu^{2+} or the global tumbling of the peptide. The saturation recovery experiments were performed at low temperatures, therefore the contribution of global tumbling to the nitroxide T_1 is negligible. Thus, the major contributor to the relaxation of the spin label is from the fast relaxation of the Cu^{2+}. Lastly, the binding site of the diamagnetic Zn^{2+} is believed to be the same as that of the Cu^{2+}.

The average distance, r, between the bound Cu^{2+} and spin label may be obtained using the Bloembergen theory as modified by Kulikov and Likhtenshtein (*9-12*):

$$< r^6 >= \frac{S(S+1)g_s^2 g_f^2 \beta_e^4}{\hbar^2}\left[\frac{1}{6}B + 3C + \frac{3}{2}E\right]\left[\frac{1}{T_{1s}} - \frac{1}{T_{1s}^0}\right]^{-1}$$

$$B = \frac{T_{2f}}{1+(\omega_s - \omega_f)^2 T_{2f}^2}(3\cos^2\theta - 1)^2$$

$$C = \frac{T_{1f}}{1+\omega_s^2 T_{1f}^2}\sin^2\theta\cos^2\theta \qquad (4\text{-}1)$$

$$E = \frac{T_{2f}}{1+(\omega_s + \omega_f)^2 T_{2f}^2}\sin^4\theta$$

where r is the average Cu^{2+}-nitroxide interspin distance, and f and s represent the Cu^{2+} and nitroxide electron spins, respectively. T_{1s} and T_{1s}^0 represent the nitroxide longitudinal relaxation in the presence and absence of Cu^{2+}, respectively. The parameters T_{1f} and T_{2f} are the longitudinal and transverse relaxation rates of the Cu^{2+} electron spin. The values of g_f and g_s, which represent the Cu^{2+} and nitroxide electron spin isotropic g values, are 2.1166 and 2.0061, respectively.(*174*) The resonant frequencies for Cu^{2+} and nitroxide are represented by ω_f and ω_s. Finally, β_e is the Bohr magneton, $\hbar$ is the reduced Planck constant, and θ is the angle between the interspin vector and the external magnetic field.

It has been shown previously that if the following inequalities hold true (*84*, *177*):

$$\omega_f^2 T_{1f}^2, (\omega_s + \omega_f)^2 T_{2f}^2, and\ (\omega_s - \omega_f)^2 T_{2f}^2 \gg 1 \quad \text{and} \quad (1 - \frac{g_f}{g_s})^2 \ll 1$$

the B-term in equation (4-1) will dominate. If the T_{1s} and T_{1s}^0 values are measured at the center of the nitroxide spectrum, where many orientations contribute to the signal, equation (4-1) can be rewritten as:

$$< r^6 >= \frac{g_s^2 g_f^2 \beta_e^4}{10\hbar^2} \left[\frac{1}{(\omega_s - \omega_f)^2 T_{2f}} \right] \left[\frac{1}{T_{1s}} - \frac{1}{T_{1s}^0} \right]^{-1} \qquad (4\text{-}2)$$

By using this equation, only the Cu^{2+} T_{2f} values are needed to solve for the average distance. This reduces the error in the average distance determination as any error in the T_{1f} value is eliminated.

To provide an estimate of T_{2f}, echo decay experiments were performed on the 3AK peptide at 80 K to measure the Cu^{2+} T_m. The echo decays were fit using a stretched exponential (*13*):

$$I(t) = I(0)\exp[-(2t/T_m)^x] \quad (4\text{-}3)$$

where x depends on the rate and mechanism of the dephasing process. In fitting the decays the exponent x was allowed to vary, however, fits were achieved with x = 0.9-1.3, indicative of instantaneous diffusion dominating the dephasing mechanism.(*13*) Using the Cu^{2+} T_m value to calculate the Cu^{2+}-nitroxide distance may introduce error into the distance measurement. However it provides an upper estimate of the average distance as T_m is typically smaller than T_{2f}.(*13*)

Nitroxide saturation recovery curves were collected in the presence of Cu^{2+} or Zn^{2+} at 80 K. These curves are shown in Figure 4-3 where the curve in the presence of Cu^{2+} is shown in black and in the presence of Zn^{2+} in gray. The T_{1s} and T_{1s}^{0} values were obtained by fitting these curves to a biexponential function. These values were then used to calculate the average Cu^{2+}-nitroxide distance using equation (4-2). The average distance for the 3AK and 4AK peptides was found to be 21 ± 1 Å and 26 ± 1Å, respectively. The error in the average distances is due to error in the fits to the recovery curves.

4.5 DISCUSSION

In this work, distance measurements were performed on two polyalanine peptides of differing length (3AK and 4AK) using both the DEER and saturation recovery techniques. DEER experiments provide distance distributions from which the average distance and standard

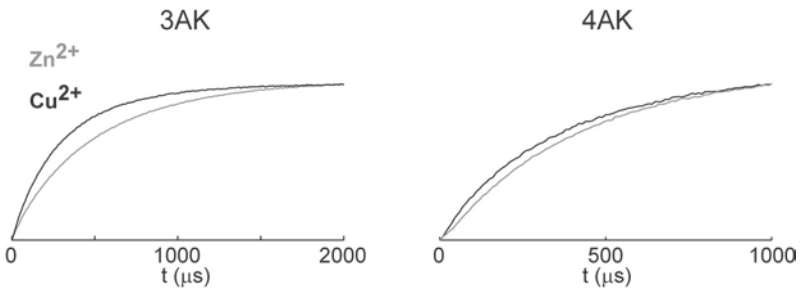

Figure 4-3. Nitroxide saturation recovery curves for the 3AK and 4AK peptides. The recovery curves collected in the presence of Cu^{2+} and Zn^{2+} are shown in black and gray, respectively.

deviation can be obtained. On the other hand, saturation recovery experiments only provide an average distance. This average distance may be biased towards shorter distances compared to the DEER results due to the r^{-6} nature of the relaxation-based measurements. The goal of this work was to compare the average distance obtained for the two peptides using both the DEER and saturation recovery methods. In addition, the effect of the distance distribution on the average distance obtained from the saturation recovery experiment was assessed.

Using a shorter version of the polyalanine peptide (2AK - shorter by one AAAAK sequence of amino acids, or one helical turn) distance measurements were performed previously.(*167, 174*) In the work of Jun *et al.* the average distance between the Cu^{2+} and spin label was determined using inversion recovery experiments at room temperature. The average distance from this work was found to be 25 Å. This average peptide distance agreed with the distance measured from molecular dynamics simulations.(*174*) Work by Yang *et al.* used the DEER experiment to measure the distance between the bound Cu^{2+} and the spin label. In this case an average distance of 27 Å was obtained, indicating a bias of the relaxation-based measurements towards shorter distances.(*167*) Taken together these works demonstrate the need for comparing the average distances measured using DEER and relaxation-based techniques for peptides of differing lengths.

Based on the r^{-6} dependence of relaxation-based experiments, we can expect the average distance to be biased to shorter distances. Using equation (1), the change in $1/T_{1s}$ upon addition of Cu^{2+} can be calculated for different r values in a distance distribution, P(r). The expected average distance, $\langle r_{ESR} \rangle$, can then be calculated using the following equations:

$$\kappa = \frac{g_s^2 g_f^2 \beta_e^4}{10\hbar^2}\left[\frac{1}{(\omega_f - \omega_s)^2 T_{2f}}\right] \tag{4-4}$$

$$< r_{ESR} > = \kappa^{1/6} \cdot \left[\left\{ \sum_{r_2}^{r_1} P(r) \cdot \left(\frac{\kappa}{r^6} + \frac{1}{T_{1s}^0} \right) \right\} - \frac{1}{T_{1s}^0} \right]^{-1/6} \quad (4\text{-}5)$$

where P(r) is the distance distribution obtained from the DEER experiment.(*174*)

$<r_{ESR}>$ was calculated from the 3AK and 4AK distance distributions (280 MHz offset), using the T_m value for 3AK and the T_{1s}^0 values for 3AK and 4AK at 80K. The value of $<r_{ESR}>$ was calculated to be 22 Å for the 3AK peptide, and 24 Å for 4AK. Both values are less than the average distances measured in the DEER experiment: 29 Å for 3AK and 34 Å for 4AK. Figure 4-4 shows the distance distributions for 3AK and 4AK as well as their respective predicted $<r_{ESR}>$ values (filled circles). The 4AK $<r_{ESR}>$ value is similar to that of 3AK, although the average distance for these two peptides differed significantly in the DEER distributions. The reason for this is due to the larger standard deviation of the 4AK DEER distance distribution. Due to the r^{-6} nature of relaxation-based measurements favoring shorter distances, broader distance distributions will shift the $<r_{ESR}>$ to shorter distances.

Also shown in Figure 4-4 are the average distances measured for 3AK and 4AK using the saturation recovery experiment (open circles). As expected, these values are similar to $<r_{ESR}>$ and shorter than the average distances measured in the DEER experiment. There is a significant difference between the average distance measured for 3AK versus 4AK using the saturation recovery experiment. Indeed, the percent change of the recovery curves was 38% and 11% for the 3AK and 4AK peptides, respectively. However, the distance distribution has a strong effect on the average distance measured by saturation recovery. As the distribution becomes broader, the measured average distances become smaller, increasing the error of the measurement.

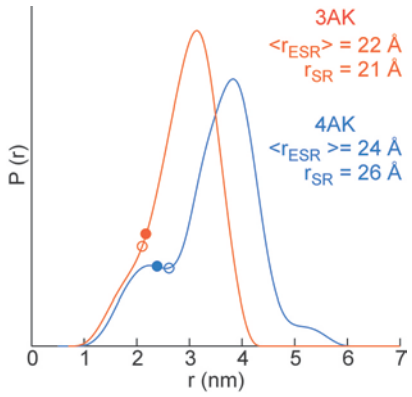

Figure 4-4. Distance distributions from the 280 MHz offset DEER data collected for 3AK (orange) and 4AK (blue). The distributions were used to calculate the expected average distance, $\langle r_{ESR} \rangle$, for the relaxation-based measurements (filled circles). The average distances obtained from the saturation recovery experiments are also shown (open circles).

4.6 CONCLUSIONS

In this work we have shown that the average distance obtained by saturation recovery measurements is significantly affected by the distance distribution. As the standard deviation of the distribution increases, the average distance shifts to shorter distances. Due to this effect, the accuracy and precision of the relaxation-based experiments is reduced. This work has shown that the DEER experiment provides the most reliable results for a Cu^{2+}-coordinated system. This is particularly true for Cu^{2+}-nitroxide systems where the orientational effects are negligible.

4.7 ACKNOWLEDGEMENTS

This work was supported by a National Science Foundation (MCB 0842956) grant to S. S. The simulations were supported by the University of Pittsburgh Center for Simulation and Modeling.

5.0 OVERVIEW OF MAJOR ACHIEVEMENTS

EcoRI has been the subject of extensive genetic, biochemical, and biophysical research. Thermodynamic profiles ($\Delta G°$, $\Delta H°$, $T\Delta S°$, $\Delta C_p°$) differ for each EcoRI complex: specific, miscognate, and nonspecific. In order to better understand the binding affinity of EcoRI towards its specific sequence the structure and dynamics of these three classes of complexes must be understood.

The arm region of EcoRI is believed to play a major role in the binding specificity of the enzyme due to key contacts that are made between this region and the DNA. Although it is known how the binding affinity and contacts differ between the three complexes, there is little to no structural information on the miscognate and nonspecific complexes. For this reason, previous work by Stone *et al.* was performed to obtain distance constraints in the arm region of the EcoRI bound to the different sequences of DNA. Through this work they found that the arms enfold the DNA similarly in the three complexes. In addition, the noncognate complexes showed broader distance distributions indicating an increase in mobility of the arms in these complexes.

To gain biologically relevant information from these distance measurements, further details about the side chain packing and orientations of the spin label is needed. For this reason, parallel MD simulations were performed on the specific EcoRI-DNA complex at the spin-labeled sites which were measured in the DEER experiments. Using correlated distance constraints to

validate the simulations, preferred orientations of the spin label present on an α-helix and a β-strand were determined. In addition, the C_α-C_α distance distributions were obtained from the simulation providing insight into the changes of the backbone dynamics at each of the spin-labeled sites. This work provided insight into the preferred conformations of the spin label at different secondary structures. This is particularly important for the spin-labeled sites on β-strand structures as less is known about the behavior of the spin label at these sites. It also highlighted the significance of using correlated distance constraints to compare simulated results to experiment. By identifying the preferred conformers at these spin-labeled sites, the contribution of spin label flexibility and length to the distance distribution measured by the DEER experiment can be delineated. In this way, the C_α-C_α distance distribution can be estimated. This would be beneficial not only for resolving the backbone distances in the specific complex, but also to compare to the distances measured in the miscognate and nonspecific complexes.

In addition to obtaining structural constraints, we were interested in probing the change in dynamics and order between the three EcoRI complexes. In particular, it was of interest to probe the region which is sensitive to the changes between the complexes as has been shown through thermodynamic profiles. The noncognate complexes are believed to form looser protein-DNA complexes. Indeed, the DEER results indicated that the arm region of EcoRI may possess higher mobility or span more conformational states in the noncognate complexes compared to the specific complex. Room temperature CW spectra were collected on various spin-labeled sites in the arm region and one in the main domain of EcoRI in the specific, miscognate, and nonspecific complex. Quantitative analysis through simulation found that the site labeled at the protein-DNA interface was most sensitive to the changes in dynamics and order between the three

complexes. Spin-labeled sites further from the DNA showed little difference in the dynamics between the three complexes. This work contributes not only to the understanding of site-specific changes in the classes of the EcoRI complex, but provides insight into the behavior of spin-labeled sites for protein-DNA complexes as a whole.

In the future this project could explore several avenues. MD simulation of the miscognate and nonspecific complexes would shed light on possible changes of the protein-DNA interface using the distance distributions obtained from the DEER experiment to validate the simulated results. Additionally, it would be interesting to observe the change in distance constraints and dynamics and order of the spin-labeled sites highlighted in this thesis when a promiscuous mutation is also present in EcoRI. Promiscuous mutants have been found to bind to miscognate sites more readily than wild-type EcoRI. It would be interesting to see the change in the arm orientation and backbone mobility for these mutants. Lastly, there are several classes of other restriction endonucleases that are of interest such as EcoRV and BamHI that would be interesting to study and compare to the trends observed in the EcoRI system using ESR.

In addition to this research we have helped other researchers by providing meaningful ESR data. The published and submitted papers are listed below.

List of Papers

Stone, K. M., Townsend, J. E., Sarver, J., Sapienza, P. J., Saxena, S., and Jen-Jacobson, L. (2008) Electron spin resonance shows common structural features for different classes of EcoRI-DNA complexes, *Angew Chem, Int Ed, 47,* 10192-10194.

Sarver, J. L., Townsend, J. E., Rajapakse, Jen-Jacobson, L. and Saxena, S. (2012) Simulating the dynamics and orientations of spin-labeled side chains in the restriction endonuclease EcoRI, *J. Phys. Chem. B., 2012, 116,* 4024-4033.

Mamonov, A. B., Lettieri, S., Ding, Y., Sarver, J. L., Palli, R., Cunningham, T., Saxena S., Zuckerman, D. M. (2012) Tunable mixed-resolution modeling using library-based Monte Carlo and graphics processing units. *J. Chem. Theory Comp.,* Submitted.

Sarver, J. L., Townsend, J. E., Saxena, S., Jen-Jacobson, L. (2012) Electron Spin Resonance Reveals That the Protein-DNA Interface is Sensitive to Different Classes of a Protein-DNA Complex. *Biochemistry,* In Preparation.

Sarver, J. L., Saxena, S. (2012) Measuring Cu^{2+}-Nitroxide Distances Using Double Electron-Electron Resonance and Saturation-Recovery. *Applied Magnetic Resonance,* In preparation.

BIBLIOGRAPHY

1. Fanucci, G. E., and Cafiso, D. S. (2006) Recent advances and applications of site-directed spin labeling, *Curr. Opin. Struct. Biol. 16*, 644-653.
2. Altenbach, C., Flitsch, S. L., Khorana, H. G., and Hubbell, W. L. (1989) Structural Studies on Transmembrane Proteins. 2. Spin Labeling of Bacteriorhodopsin Mutants at Unique Cysteines, *Biochemistry 28*, 7806-7812.
3. Hubbell, W. L., and Altenbach, C. (1994) Investigation of structure and dynamics in membrane proteins using site-directed spin labeling, *Curr. Opin. Struct. Biol. 4*, 566-573.
4. Columbus, L., and Hubbell, W. L. (2002) A new spin on protein dynamics, *Trends Biochem. Sci. 27*, 288-295.
5. Milov, A. D., Ponomarev, A. B., and Tsvetkov, Y. D. (1984) Electron-Electron Double Resonance in Electron Spin Echo: Model Biradical Systems and the Sensitized Photolysis of Decalin, *Chem. Phys. Lett. 110*, 67-72.
6. Milov, A. D., Salikhov, K. M., and Shirov, M. D. (1981) Application of endor in electron-spin echo for paramagnetic center distribution in solids, *Fiz. Tverd. Tela 23*, 975-982.
7. Martin, R. E., Pannier, M., Diederich, F., Gramlich, V., Hubrich, M., and Spiess, H. W. (1998) Determination of End-to-End Distances in a Series of TEMPO Diradicals of up to 2.8 nm Length with a New Four-Pulse Double Electron Electron Resonance Experiment, *Angew. Chem., Int. Ed. 37*, 2833-2837.
8. Pannier, M., Veit, S., Godt, A., Jeschke, G., and Spiess, H. W. (2000) Dead-Time Free Measurement of Dipole-Dipole Interactions between Electron Spins, *J. Magn. Reson. 142*, 331-340.
9. Bloembergen, N., Shapiro, S., Pershan, P. S., and Artman, J. O. (1959) Cross-Relaxation in Spin Systems, *Physical Review 114*, 445-459.
10. Bloembergen, N. (1949) On the interaction of nuclear spins in a crystalline lattice, *Physica 15*, 386-426.
11. Bloembergen, N., Purcell, E. M., and Pound, R. V. (1948) Relaxation Effects in Nuclear Magnetic Resonance Absorption, *Physical Review 73*, 679-712.
12. Kulikov, A. V., and Likhtenstein, G. I. (1977) The use of spin relaxation phenomena in the investigation of the structure of model and biological systems by the method of spin labels, *Advances in Molecular Relaxation and Interaction Processes 10*, 47-79.
13. Eaton, S. S., and Eaton, G. R. (2000) Biological Magnetic Resonance, In *Distance Measurements in Biological Systems by EPR* (Berliner, L. J., Eaton, S. S., and Eaton, G. R., Eds.), Kluwer Academic, New York.

14. Earle, K. A., and Budil, D. E. (2006) Calculating Slow-Motion ESR Spectra of Spin-Labeled Polymers, In *Advanced ESR Methods in Polymer Research* (Schlick, S., Ed.), John Wiley & Sons, Hoboken.
15. Budil, D. E., Lee, S., Saxena, S., and Freed, J. H. (1996) Nonlinear-Least-Squares Analysis of Slow-Motion EPR Spectra in One and Two Dimensions Using a Modified Levenberg-Marquardt Algorithm, *J. Magn. Reson. 120*, 155-189.
16. Schneider, D. J., and Freed, J. H., (Eds.) (1989), Vol. 8, Plenum Publishing Corporation, New York.
17. Piton, N., Mu, Y., Stock, G., Prisner, T. F., Schiemann, O., and Engels, J. W. (2007) Base-specific spin-labeling of RNA for structure determination, *Nucleic Acids Res. 35*, 3128 - 3143.
18. Hubbell, W. L., McHaourab, H. S., Altenbach, C., and Lietzow, M. A. (1996) Watching proteins move using site-directed spin labeling, *Structure 4*, 779-783.
19. Cai, Q., Kusnetzow, A. K., Hubbell, W. L., Haworth, I. S., Gacho, G. P. C., Eps, N. V., Hideg, K., Chambers, E. J., and Qin, P. Z. (2006) Site-directed spin labeling measurements of nanometer distances in nucleic acids using a sequence-independent nitroxide probe, *Nucleic Acids Res. 34*, 4722-4730.
20. Todd, A. P., Cong, J., Levinthal, F., Levinthal, C., and Hubbell, W. L. (1989) Site-Directed Mutagenesis of Colicin E1 Provides Specific Attachment Sites for Spin Labels Whose Spectra Are Sensitive to Local Conformation, *Proteins: Struct., Funct., Genet. 6*, 294 - 305.
21. Mchaourab, H. S., Lietzow, M. A., Hideg, K., and Hubbell, W. L. (1996) Motion of Spin-Labeled Side Chains in T4 Lysozyme. Correlation with Protein Structure and Dynamics, *Biochemistry 35*, 7692-7704.
22. Ding, Z., Gulla, A. F., and Budil, D. E. (2001) Ab initio calculations of electric field effects on the g-tensor of a nitroxide radical, *J. Chem. Phys. 115*, 10685-10693.
23. Brustolon, M., Maniero, A. L., and Corvaja, C. (1984) *Mol. Phys. 51*, 1269.
24. Schreier, S., Polnaszek, C. F., and Smith, I. C. (1978) Spin labels in membranes. Problems in practice., *Biochim. Biophys. Acta 515*, 395-436.
25. Columbus, L., Kálai, T., Jekö, J., Hideg, K., and Hubbell, W. L. (2001) Molecular Motion of Spin Labeled Side Chains in α-Helices: Analysis by Variation of Side Chain Structure†, *Biochemistry 40*, 3828-3846.
26. Hubbell, W. L., Cafiso, D. S., and Altenbach, C. (2000) Identifying conformational changes with site-directed spin labeling, *Nat. Struct. Mol. Biol. 7*, 735-739.
27. Columbus, L., and Hubbell, W. L. (2004) Mapping Backbone Dynamics in Solution with Site-Directed Spin Labeling: GCN4−58 bZip Free and Bound to DNA†, *Biochemistry 43*, 7273-7287.
28. Borbat, P. P., Costa-Filho, A. J., Earle, K. A., Moscicki, J. K., and Freed, J. H. (2001) Electron Spin Resonance in Studies of Membranes and Proteins, *Science 291*, 266-269.
29. (2007) ESR Spectroscopy in Membrane Biophysics, In *Biological Magnetic Resonance* (Hemminga, M. A., and Berliner, L. J., Eds.), p 379, Springer, New York.
30. Zhang, Z., Fleissner, M. R., Tipikin, D. S., Liang, Z., Moscicki, J. K., Earle, K. A., Hubbell, W. L., and Freed, J. H. (2010) Multifrequency Electron Spin Resonance Study of the Dynamics of Spin Labeled T4 Lysozyme, *Journal of Physical Chemistry B 114*, 5503-5521.

31. Lietzow, M. A., and Hubbell, W. L. (2004) Motion of Spin Label Side Chains in Cellular Retinol-Binding Protein: Correlation with Structure and Nearest-Neighbor Interactions in an Antiparallel β-Sheet†, *Biochemistry 43*, 3137-3151.
32. Liang, Z., Lou, Y., Freed, J. H., Columbus, L., and Hubbell, W. L. (2004) A Multifrequency Electron Spin Resonance Study of T4 Lysozyme Dynamics Using the Slowly Relaxing Local Structure Model, *J. Phys. Chem. B 108*, 17649-17659.
33. Liang, Z., Freed, J. H., Keyes, R. S., and Bobst, A. M. (2000) An Electron Spin Resonance Study of DNA Dynamics Using the Slowly Relaxing Local Structure Model, *J. Phys. Chem. B 104*, 5372-5381.
34. Liang, Z., and Freed, J. H. (1999) An Assessment of the Applicability of Multifrequency ESR to Study the Complex Dynamics of Biomolecules, *J. Phys. Chem. B 103*, 6384 - 6396.
35. Barnes, J. P., Liang, Z., McHaourab, H. S., Freed, J. H., and Hubbell, W. L. (1999) A Multifrequency Electron Spin Resonance Study of T4 Lysozyme Dynamics, *Biophys. J. 76*, 3298-3306.
36. Möbius, K., Savitsky, A., Wegener, C., Plato, M., Fuchs, M., Schnegg, A., Dubinskii, A. A., Grishin, Y. A., Grigor'ev, I. A., Kühn, M., Duché, D., Zimmermann, H., and Steinhoff, H. J. (2005) Combining high-field EPR with site-directed spin labeling reveals unique information on proteins in action, *Magn. Reson. Chem. 43*, S4-S19.
37. Nesmelov, Y., and Thomas, D. (2010) Protein structural dynamics revealed by site-directed spin labeling and multifrequency EPR, *Biophysical Reviews 2*, 91-99.
38. Nesmelov, Y. E., Agafonov, R. V., Burr, A. R., Weber, R. T., and Thomas, D. D. (2008) Structure and Dynamics of the Force-Generating Domain of Myosin Probed by Multifrequency Electron Paramagnetic Resonance, *Biophys. J. 95*, 247-256.
39. Nesmelov, Y. E., Karim, C. B., Song, L., Fajer, P. G., and Thomas, D. D. (2007) Rotational Dynamics of Phospholamban Determined by Multifrequency Electron Paramagnetic Resonance, *Biophys. J. 93*, 2805-2812.
40. White, G. F., Ottignon, L., Georgiou, T., Kleanthous, C., Moore, G. R., Thomson, A. J., and Oganesyan, V. S. (2007) Analysis of nitroxide spin label motion in a protein–protein complex using multiple frequency EPR spectroscopy, *J. Magn. Reson. 185*, 191-203.
41. Sung, T.-C., and Chiang, Y.-W. (2010) Identification of complex dynamic modes on prion protein peptides using multifrequency ESR with mesoporous materials, *Phys. Chem. Chem. Phys. 12*.
42. Schiemann, O., and Prisner, T. F. (2007) Long-range distance determinations in biomacromolecules by EPR spectroscopy, *Q. Rev. Biophys. 40*, 1-53.
43. Eaton, S. S., More, K. M., Sawant, B. M., and Eaton, G. R. (1983) Use of the ESR half-field transition to determine the interspin distance and the orientation of the interspin vector in systems with two unpaired electrons, *J. Am. Chem. Soc. 105*, 6560-6567.
44. Persson, M., Harbridge, J. R., Hammarström, P., Mitri, R., Mårtensson, L.-G., Carlsson, U., Eaton, G. R., and Eaton, S. S. (2001) Comparison of Electron Paramagnetic Resonance Methods to Determine Distances between Spin Labels on Human Carbonic Anhydrase II, *Biophys. J. 80*, 2886-2897.
45. Hustedt, E. J., Stein, R. A., Sethaphong, L., Brandon, S., Zhou, Z., and DeSensi, S. C. (2006) Dipolar Coupling between Nitroxide Spin Labels: The Development and Application of a Tether-in-a-Cone Model, *Biophys. J. 90*, 340-356.

46. Rabenstein, M. D., and Shin, Y. K. (1995) Determination of the distance between two spin labels attached to a macromolecule, *Proc. Natl. Acad. Sci. U. S. A. 92*, 8239-8243.
47. Larsen, R. G., and Singel, D. J. (1993) Double electron--electron resonance spin--echo modulation: Spectroscopic measurement of electron spin pair separations in orientationally disordered solids, *J. Chem. Phys. 98*, 5134-5146.
48. Saxena, S., and Freed, J. H. (1997) Theory of double quantum two-dimensional electron spin resonance with application to distance measurements, *J. Chem. Phys. 107*, 1317-1340.
49. Borbat, P. P., and Freed, J. H. (1999) Multiple quantum ESR and distance measurements, *Chem. Phys. Lett. 313*, 145-154.
50. Saxena, S., and Freed, J. H. (1996) Double quantum two-dimensional Fourier transform electron spin resonance: Distance measurements, *Chem. Phys. Lett. 251*, 102-110.
51. Borbat, P. P., McHaourab, H. S., and Freed, J. H. (2002) Protein Structure Determination Using Long-Distance Constraints from Double-Quantum Coherence ESR: Study of T4 Lysozyme, *J. Am. Chem. Soc. 124*, 5304-5314.
52. Jeschke, G. (2002) Distance Measurements in the Nanometer Range by Pulse EPR, *ChemPhysChem 3*, 927-932.
53. Reginsson, G. W., and Schiemann, O. (2011) Pulsed electron–electron double resonance: beyond nanometre distance measurements on biomacromolecules, *Biochem. J. 434*, 353-363.
54. Stone, K. M., Townsend, J. E., Sarver, J., Sapienza, P. J., Saxena, S., and Jen-Jacobson, L. (2008) Electron spin resonance shows common structural features for different classes of EcoRI-DNA complexes, *Angew. Chem., Int. Ed. 47*, 10192-10194.
55. Kear, J. L., Blackburn, M. E., Veloro, A. M., Dunn, B. M., and Fanucci, G. E. (2009) Subtype Polymorphisms Among HIV-1 Protease Variants Confer Altered Flap Conformations and Flexibility, *J. Am. Chem. Soc. 131*, 14650-14651.
56. Vileno, B., Chamoun, J., Liang, H., Brewer, P., Haldeman, B. D., Facemyer, K. C., Salzameda, B., Song, L., Li, H.-C., Cremo, C. R., and Fajer, P. G. (2011) Broad disorder and the allosteric mechanism of myosin II regulation by phosphorylation, *Proc. Natl. Acad. Sci. U. S. A. 108*, 8218-8223.
57. Galiano, L., Ding, F., Veloro, A. M., Blackburn, M. E., Simmerling, C., and Fanucci, G. E. (2009) Drug Pressure Selected Mutations in HIV-1 Protease Alter Flap Conformations, *J. Am. Chem. Soc. 131*, 430-431.
58. Boura, E., Różycki, B., Herrick, D. Z., Chung, H. S., Vecer, J., Eaton, W. A., Cafiso, D. S., Hummer, G., and Hurley, J. H. (2011) Solution structure of the ESCRT-I complex by small-angle X-ray scattering, EPR, and FRET spectroscopy, *Proc. Natl. Acad. Sci. U. S. A. 108*, 9437-9442.
59. Lai, A. L., Huang, H., Herrick, D. Z., Epp, N., and Cafiso, D. S. (2011) Synaptotagmin 1 and SNAREs Form a Complex That Is Structurally Heterogeneous, *J. Mol. Biol. 405*, 696-706.
60. Altenbach, C., Kusnetzow, A. K., Ernst, O. P., Hofmann, K. P., and Hubbell, W. L. (2008) High resolution distance mapping in rhodopsin reveals the pattern of helix movment due to activation, *Proc. Natl. Acad. Sci. U. S. A. 105*, 7439-7444.
61. Dockter, C., Volkov, A., Bauer, C., Polyhach, Y., Joly-Lopez, Z., Jeschke, G., and Paulsen, H. (2009) Refolding of the integral membrane protein light-harvesting complex II monitored by pulse EPR, *Proc. Natl. Acad. Sci. U. S. A. 106*, 18485-18490.

62. Zou, P., Bortolus, M., and Mchaourab, H. S. (2009) Conformational cycle of the ABC transporter MsbA in liposomes:detailed analysis using double electron electron resonance spectroscopy, *J. Mol. Biol. 393*, 586-597.
63. Hilger, D., Polyhach, Y., Jung, H., and Jeschke, G. (2009) Backbone Structure of Transmembrane Domain IX of the Na^+/Proline Transporter PutP of *Escherichia coli*, *Biophys. J. 96*, 217-225.
64. Endeward, B., Butterwick, J. A., MacKinnon, R., and Prisner, T. F. (2009) Pulsed Electron−Electron Double-Resonance Determination of Spin-Label Distances and Orientations on the Tetrameric Potassium Ion Channel KcsA, *J. Am. Chem. Soc. 131*, 15246-15250.
65. Hagelueken, G., Ingledew, W. J., Huang, H., Petrovic-Stojanovska, B., Whitfield, C., ElMkami, H., Schiemann, O., and Naismith, J. H. (2009) PELDOR Spectroscopy Distance Fingerprinting of the Octameric Outer-Membrane Protein Wza from Escherichia coli, *Angew. Chem., Int. Ed. 48*, 2904-2906.
66. Pornsuwan, S., Schafmeister, C. E., and Saxena, S. (2008) Analysis of the Dynamical Flexibility of Bis-peptide Nanostructures, *J. Phys. Chem. C 112*, 1377-1384.
67. Pornsuwan, S., Bird, G., Schafmeister, C. E., and Saxena, S. (2006) Flexibility and lengths of bis-peptide nanostructures by electron spin resonance, *J. Am. Chem. Soc. 128*, 3876-3877.
68. Jeschke, G., Sajid, M., Schulte, M., Ramezanian, N., Volkov, A., Zimmermann, H., and Godt, A. (2010) Flexibility of Shape-Persistent Molecular Building Blocks Composed of p-Phenylene and Ethynylene Units, *J. Am. Chem. Soc. 132*, 10107-10117.
69. Godt, A., Schulte, M., Zimmermann, H., and Jeschke, G. (2006) How Flexible Are Poly(*para*-phenyleneethynylene)s?, *Angew. Chem. Int. Ed. 45*, 7560 - 7564.
70. Milov, A., Samoilova, R., Tsvetkov, Y., Peggion, C., Formaggio, F., Toniolo, C., and Raap, J. (2006) Aggregation of spin-labeled alamethicin in low-polarity solutions as studied by PELDOR spectroscopy, *Doklady Physical Chemistry 406*, 21-25.
71. Salnikov, E. S., Erilov, D. A., Milov, A. D., Tsvetkov, Y. D., Peggion, C., Formaggio, F., Toniolo, C., Raap, J., and Dzuba, S. A. (2006) Location and Aggregation of the Spin-Labeled Peptide Trichogin GA IV in a Phospholipid Membrane as Revealed by Pulsed EPR, *Biophys. J. 91*, 1532-1540.
72. Milov, A. D., Tsvetkov, Y. D., Formaggio, F., Oancea, S., Toniolo, C., and Raap, J. (2003) Aggregation of Spin Labeled Trichogin GA IV Dimers: Distance Distribution between Spin Labels in Frozen Solutions by PELDOR Data, *J. Chem. Phys. B 107*, 13719-13727.
73. Schiemann, O., Piton, N., Mu, Y., Stock, G., Engles, J. W., and Prisner, T. F. (2004) A PELDOR-Based Nanometer Distance Ruler for Oligonucleotides, *J. Am. Chem. Soc. 126*, 5722-5729.
74. Kuznetsov, N. A., Milov, A. D., Koval, V. V., Samoilova, R. I., Grishin, Y. A., Knorre, D. G., Tsvetkov, Y. D., Fedorova, O. S., and Dzuba, S. A. (2009) PELDOR study of conformations of double-spin-labeled single- and double-stranded DNA with non-nucleotide inserts, *Phys. Chem. Chem. Phys. 11*, 6826-6832.
75. Krstić, I., Frolow, O., Sezer, D., Endeward, B., Weigand, J. E., Suess, B., Engels, J. W., and Prisner, T. F. (2010) PELDOR Spectroscopy Reveals Preorganization of the Neomycin-Responsive Riboswitch Tertiary Structure, *J. Am. Chem. Soc. 132*, 1454-1455.

76. Kim, N.-K., Bowman, M. K., and DeRose, V. J. (2010) Precise Mapping of RNA Tertiary Structure via Nanometer Distance Measurements with Double Electron−Electron Resonance Spectroscopy, *J. Am. Chem. Soc. 132*, 8882-8884.
77. Schiemann, O., Weber, A., Edwards, T., Prisner, T. F., and Sigurdsson, S. (2003) Nanometer distance measurements on RNA using PELDOR, *J. Am. Chem. Soc. 125*, 3434-3435.
78. Sicoli, G., Wachowius, F., Bennati, M., and Höbartner, C. (2010) Probing Secondary Structures of Spin-Labeled RNA by Pulsed EPR Spectroscopy, *Angew. Chem., Int. Ed. 49*, 6443-6447.
79. Jeschke, G. (2012) DEER Distance Measurements on Proteins, *Annu. Rev. Phys. Chem. 63*, 419-446.
80. Jeschke, G., Chechik, V., Ionita, P., Godt, A., Zimmermann, H., Banham, J., Timmel, C., Hilger, D., and Jung, H. (2006) DeerAnalysis 2006 - a Comprehensive Software Package for Analyzing Pulsed ELDOR Data, *Appl. Magn. Reson. 30*, 473-498.
81. MacArthur, R., Sazinsky, M. H., Kühne, H., Whittington, D. A., Lippard, S. J., and Brudvig, G. W. (2002) Component B Binding to the Soluble Methane Monooxygenase Hydroxylase by Saturation-Recovery EPR Spectroscopy of Spin-Labeled MMOB, *J. Am. Chem. Soc. 124*, 13392-13393.
82. Zhou, Y., Bowler, B. E., Lynch, K., Eaton, S. S., and Eaton, G. R. (2000) Interspin Distances in Spin-Labeled Metmyoglobin Variants Determined by Saturation Recovery EPR, *Biophys. J. 79*, 1039-1052.
83. Ulyanov, D., Bowler, B. E., Eaton, G. R., and Eaton, S. S. (2008) Electron-Electron Distances in Spin-Labeled Low-Spin Metmyoglobin Variants by Relaxation Enhancement, *Biophys. J. 95*, 5306-5316.
84. Hirsh, D. J., Beck, W. F., Innes, J. B., and Brudvig, G. W. (1992) Using saturation-recovery EPR to measure distances in proteins: applications to photosystem II, *Biochemistry 31*, 532-541.
85. Rakowsky, M. H., More, K. M., Kulikov, A. V., Eaton, G. R., and Eaton, S. S. (1995) Time-Domain Electron Paramagnetic Resonance as a Probe of Electron-Electron Spin-Spin Interaction in Spin-Labeled Low-Spin Iron Porphyrins, *J. Am. Chem. Soc. 117*, 2049-2057.
86. Martin, R. E., Pannier, M., Diederich, F., Gramlich, V., Hubrich, M., and Spiess, H. W. (1998) Determination of End-to-End Distances in a Series of TEMPO Diradicals of up to 2.8 nm Length with a New Four-Pulse Double Electron Electron Resonance Experiment, *Angew. Chem. Int. Ed. 37*, 2833-2837.
87. Margraf, D., Bode, B. E., Marko, A., Schiemann, O., and Prisner, T. F. (2007) Conformational flexibility of nitroxide biradicals determined by X-band PELDOR experiments, *Mol. Phys. 105*, 2153 - 2160.
88. Freed, D. M., Horanyi, P. S., Wiener, M. C., and Cafiso, D. S. (2010) Conformational Exchange in Membrane Transport Protein Is Altered in Protein Crystals, *Biophys. J. 99*, 1604-1610.
89. Fleissner, M. R., Cascio, D., and Hubbell, W. L. (2009) Structural origin of weakly ordered nitroxide motion in spin-labeled proteins, *Protein Sci. 18*, 893-908.
90. Guo, Z., Cascio, D., Hideg, K., and Hubbell, W. L. (2008) Structural determinants of nitroxide motion in spin-labeled proteins: Solvent-exposed sites in helix B of T4 lysozyme, *Protein Science 17*, 228-239.

91. Guo, Z., Cascio, D., Hideg, K., Kalai, T., and Hubbell, W. L. (2007) Structural determinants of nitroxide motion in spin-labeled proteins: Tertiary contact and solvent-inaccessible sites in helix G of T4 lysozyme, *Protein Sci. 16*, 1069-1086.
92. Langen, R., Oh, K. J., Cascio, D., and Hubbell, W. L. (2000) Crystal Structures of Spin Labeled T4 Lysozyme Mutants: Implications for the Interpretation of EPR Spectra in Terms of Structure, *Biochemistry 39*, 8396-8405.
93. Gruene, T., Cho, M.-K., Karyagina, I., Kim, H.-Y., Grosse, C., Giller, K., Zweckstetter, M., and Becker, S. (2011) Integrated analysis of the conformation of a protein-linked spin label by crystallography, EPR and NMR spectroscopy, *J. Biomol. NMR 49*, 111-119.
94. Kroncke, B. M., Horanyi, P. S., and Columbus, L. (2010) Structural Origins of Nitroxide Side Chain Dynamics on Membrane Protein α-Helical Sites, *Biochemistry 49*, 10045-10060.
95. Freed, D. M., Khan, A. K., Horanyi, P. S., and Cafiso, D. S. (2011) Molecular Origin of Electron Paramagnetic Resonance Line Shapes on β-Barrel Membrane Proteins: The Local Solvation Environment Modulates Spin-Label Configuration, *Biochemistry 50*, 8792-8803.
96. Tombolato, F., Ferrarini, A., and Freed, J. H. (2006) Dynamics of the Nitroxide Side Chain in Spin-Labeled Proteins, *J. Phys. Chem. B 110*, 26248-26259.
97. Warshaviak, D. T., Serbulea, L., Houk, K. N., and Hubbell, W. L. (2011) Conformational Analysis of a Nitroxide Side Chain in an α-Helix with Density Functional Theory, *J. Phys. Chem. B 115*, 397-405.
98. Sezer, D., Freed, J. H., and Roux, B. (2008) Parameterization, Molecular Dynamics Simulation, and Calculation of Electron Spin Resonance Spectra of a Nitroxide Spin Label on a Polyalanine α-Helix, *J. Phys. Chem. B 112*, 5755-5767.
99. Polyhach, Y., Bordignon, E., and Jeschke, G. (2011) Rotamer libraries of spin labelled cysteines from protein studies, *Phys. Chem. Chem. Phys. 13*, 2356-2366.
100. Hilger, D., Polyhach, Y., Padan, E., Jung, H., and Jeschke, G. (2007) High-resolution structure of a Na^+/H^+ antiporter dimer obtained by pulsed EPR distance measurements, *Biophys. J. 93*, 3675 - 3683.
101. Oganesyan, V. S. (2011) A general approach for prediction of motional EPR spectra from Molecular Dynamics (MD) simulations: application to spin labelled protein, *Phys. Chem. Chem. Phys. 13*, 4724-4737.
102. Beier, C., and Steinhoff, H.-J. (2006) A Structure-Based Simulation Approach for Electron Paramagnetic Resonance Spectra Using Molecular and Stochastic Dynamics Simulations, *Biophys. J. 91*, 2647-2664.
103. Budil, D. E., Sale, K. L., Khairy, K. A., and Fajer, P. G. (2006) Calculating Slow-Motional Electron Paramagnetic Resonance Spectra from Molecular Dynamics Using a Diffusion Operator Approach, *J. Phys. Chem. A 110*, 3703-3713.
104. Sezer, D., Freed, J. H., and Roux, B. (2009) Multifrequency Electron Spin Resonance Spectra of a Spin-Labeled Protein Calculated from Molecular Dynamics Simulations, *J. Am. Chem. Soc. 131*, 2597-2605.
105. DeSensi, S. C., Rangel, D. P., Beth, A. H., Lybrand, T. P., and Hustedt, E. J. (2008) Simulation of Nitroxide Electron Paramagnetic Resonance Spectra from Brownian Trajectories and Molecular Dynamics Simulations, *Biophys. J. 94*, 3798-3809.

106. Ding, F., Layten, M., and Simmerling, C. (2008) Solution Structure of HIV-1 Protease Flaps Probed by Comparison of Molecular Dynamics Simulation Ensembles and EPR Experiments, *J. Am. Chem. Soc. 130*, 7184-7185.
107. Borovykh, I. V., Ceola, S., Gajula, P., Gast, P., Steinhoff, H.-J., and Huber, M. (2006) Distance between a native cofactor and a spin label in the reaction centre of *Rhodobacter sphaeroides* by a two-frequency pulsed electron paramagnetic resonance method and molecular dynamics simulations, *J. Magn. Reson. 180*, 178-185.
108. Ranaldi, S., Belle, V., Woudstra, M., Bourgeas, R., Guigliarelli, B., Roche, P., Vezin, H., Carrière, F., and Fournel, A. (2010) Amplitude of Pancreatic Lipase Lid Opening in Solution and Identification of Spin Label Conformational Subensembles by Combining Continuous Wave and Pulsed EPR Spectroscopy and Molecular Dynamics, *Biochemistry 49*, 2140-2149.
109. Sale, K., Sar, C., Sharp, K. A., Hideg, K., and Fajer, P. G. (2002) Structural Determination of Spin Label Immobilization and Orientation: A Monte Carlo Minimization Approach, *J. Magn. Reson. 156*, 104-112.
110. Fajer, M. I., Sale, K. L., and Fajer, P. G. (2007) Molecular Modeling of Spin Labels, In *ESR Spectroscopy in Membrane Biophysics* (Hemminga, M. A., and Berliner, L. J., Eds.), pp 254 - 257, Springer, New York.
111. Fajer, M. I., Li, H., Yang, W., and Fajer, P. G. (2007) Mapping Electron Paramagnetic Resonance Spin Label Conformations by the Simulated Scaling Method, *J. Am. Chem. Soc. 129*, 13840 - 13846.
112. Sen, K. I., Logan, T. M., and Fajer, P. G. (2007) Protein Dynamics and Monomer-Monomer Interactions in AntR Activation by Electron Paramagnetic Resonance and Double Electron-Electron Resonance, *Biochemistry 46*, 11639 - 11649.
113. Metropolis, N., Rosenbluth, A. W., Rosenbluth, M. N., and Teller, A. H. (1953) Equation of State Calculations by Fast Computing Machines, *J. Chem. Phys. 21*, 1087-1092.
114. Li, H., Fajer, M., and Yang, W. (2007) Simulated scaling method for localized enhanced sampling and simultaneous “alchemical” free energy simulations: A general method for molecular mechanical, quantum mechanical, and quantum mechanical/molecular mechanical simulations, *J. Chem. Phys. 126*, 024106.
115. Kuo, W., Herrick, D. Z., Ellena, J. F., and Cafiso, D. S. (2009) The Calcium-Dependent and Calcium-Independent Membrane Binding of Synaptotagmin 1: Two Modes of C2B Binding, *J. Mol. Biol. 387*, 284-294.
116. Flores Jiménez, R. H., Freed, D. M., and Cafiso, D. S. (2011) Lipid and Membrane Mimetic Environments Modulate Spin Label Side Chain Configuration in the Outer Membrane Protein A, *J. Phys. Chem. B 115*, 14822-14830.
117. Lesser, D. R., Kurpiewski, M. R., and Jen-Jacobson, L. (1990) The Energetic Basis of Specificity in the EcoRI Endonuclease-DNA Interaction, *Science 250*, 776-786.
118. Sapienza, P. J., Crystal A. dela Torre, IV, W. H. M., Jana, S. V., and Jen-Jacobson, L. (2005) Thermodynamic and Kinetic Basis for the Relaxed DNA Sequence Specificity of "Promiscuous" Mutant EcoRI Endonucleases, *J. Mol. Biol. 348*, 307-324.
119. Grigorescu, A., Horvath, M., Wilkosz, P. A., Chandrasekhar, K., and Rosenberg, J. M. (2004) In *Restriction Endonucleases* (Pingoud, A., Ed.), pp 137-177, Springer-Verlag.
120. Kim, Y., Grable, J. C., Love, R., Greene, P. J., and Rosenberg, J. M. (1990) Refinement of EcoRI Endonuclease Crystal Structure: A Revised Protein Chain Tracing, *Science 249*, 1307 - 1309.

121. Sapienza, P. J., Rosenberg, J. M., and Jen-Jacobson, L. (2007) Structural and Thermodynamic Basis for Enhanced DNA Binding by a Promiscuous Mutant EcoRI Endonuclease, *Structure 15*, 1368-1382.
122. Humphrey, W., Dalke, A., and Schulten, K. (1996) VMD - Visual Molecular Dynamics, *J. Molec. Graphics 14.1*, 33-38.
123. Brooks, B. R., Bruccoleri, R. E., Olafson, B. D., States, D. J., Swaminathan, S., and Karplus, M. (1983) CHARMM: A Program for Macromolecular Energy, Minimization, and Dynamics Calculations, *J. Comput. Chem. 4*, 187-217.
124. Mackerell, A. D., Feig, M., and Brooks, C. L. (2004) Extending the treatment of backbone energetics in protein force fields: Limitations of gas-phase quantum mechanics in reproducing protein conformational distributions in molecular dynamics simulations, *J. Comput. Chem. 25*, 1400-1415.
125. Phillips, J. C., Braun, R., Wang, W., Gumbart, J., Tajkhorshid, E., Villa, E., Chipot, C., Skeel, R. D., Kale, L., and Schulten, K. (2005) Scalable Molecular Dynamics with NAMD, *J. Comput. Chem. 26*, 1781-1802.
126. Dylla-Spears, R., Townsend, J. E., Sohn, L. L., Jen-Jacobson, L., and Muller, S. J. (2009) Fluorescent Marker for Direct Detection of Specific dsDNA Sequences, *Anal. Chem. 81*, 10049-10054.
127. Jeschke, G., Chechik, V., Ionita, P., Godt, A., Zimmermann, H., Banham, J., Timmel, C., Hilger, D., and Jung, H. (2006) DeerAnalysis 2006 - a Comprehensive Software Package for Analyzing Pulsed ELDOR Data, *Appl. Magn. Reson. 30*, 473-498.
128. van Gunsteren, W. F., Dolenc, J., and Mark, A. E. (2008) Molecular simulation as an aid to experimentalists, *Curr. Opin. Struct. Biol. 18*, 149-153.
129. Grigorescu, A. (2003) Structural and Energetic Determinants of the Binding Specificity of EcoRI Endonuclease, University of Pittsburgh, Pittsburgh PA.
130. www.epr.ethz.ch/sofware/index.
131. Jen-Jacobson, L. (1997) Protein-DNA Recognition Complexes: Conservation of Structure and Binding Energy in the Transition State, *Biopolymers 44*, 153-180.
132. Jen-Jacobson, L., Engler, L. E., Ames, J. T., Kurplewski, M. R., and Grigorescu, A. (2000) Thermodynamic Parameters of Specific and Nonspecific Protein-DNA Binding, *Supramol. Chem. 12*, 143-160.
133. Rosenberg, J. M. (1991) Structure and function of restriction endonucleases, *Curr. Opin. Struct. Biol. 1*, 104-113.
134. Hiller, D. A., Rodriquez, A. M., and Perona, J. J. (2005) Non-cognate Enzyme-DNA Complex: Structrural and Kinetic Analysis of EcoRV Endonuclease Bound to the EcoRI Recognition Site GAATTC, *J. Mol. Biol. 354*, 121-136.
135. Townson, S. A., Samuelson, J. C., Bao, Y., Xu, S.-y., and Aggarwal, A. K. (2007) BstYI Bound to Noncognate DNA Reveals a "Hemispecific" Complex: Implications for DNA Scanning, *Structure 15*, 449-459.
136. Viadiu, H., and Aggarwal, A. K. (2000) Structure of BamHI Bound to Nonspecific DNA: A Model for DNA Sliding, *Mol. Cell 5*, 889-895.
137. Winkler, F. K., Banner, D. W., Oefner, C., Tsernoglou, D., Brown, R. S., Heathman, S. P., Bryan, R. K., Martin, P. D., Petratos, K., and Wilson, K. S. (1993) The crystal structure of EcoRV endonuclease and of its complexes with cognate and non-cognate DNA fragments, *EMBO J. 12*, 1781-1795.

138. Isas, J. M., Langen, R., Haigler, H. T., and Hubbell, W. L. (2002) Structure and Dynamics of a Helical Hairpin and Loop Region in Annexin 12: A Site-Directed Spin Labeling Study, *Biochemistry 41*, 1464 - 1473.
139. Flores Jiménez, R. H., Freed, D. M., and Cafiso, D. S. (2011) Lipid and Membrane Mimetic Environments Modulate Spin Label Side Chain Configuration in the Outer Membrane Protein A, *J. Phys. Chem. B 115*, 14822-14830.
140. Popova, A. M., and Qin, P. Z. (2010) A Nucleotide-Independent Nitroxide Probe Reports on Site-Specific Stereomeric Environment in DNA, *Biophys. J. 99*, 2180-2189.
141. Jen-Jacobson, L., Kurpiewski, M., Lesser, D., Grable, J., Boyer, H. W., Rosenberg, J. M., and Greene, P. J. (1983) Coordinate Ion Pair Formation between EcoRI Endonuclease and DNA, *J. Biol. Chem. 258*, 14638-14646.
142. Stoll, S., and Schweiger, A. (2006) EasySpin, a comprehensive software package for spectral simulation and analysis in EPR, *J. Magn. Reson. 178*, 42-55.
143. Crepeau, R. H., Saxena, S., Lee, S., Patyal, B., and Freed, J. H. (1994) Studies on lipid membranes by two-dimensional Fourier transform ESR: Enhancement of resolution to ordering and dynamics, *Biophys. J. 66*, 1489-1504.
144. McCoy, J., and Hubbell, W. L. (2011) High-pressure EPR reveals conformational equilibria and volumetric properties of spin-labeled proteins, *Proc. Natl. Acad. Sci. U. S. A. 108*, 1331-1336.
145. Bridges, M., Hideg, K., and Hubbell, W. (2010) Resolving Conformational and Rotameric Exchange in Spin-Labeled Proteins Using Saturation Recovery EPR, *Appl. Magn. Reson. 37*, 363-390.
146. López, C. J., Fleissner, M. R., Guo, Z., Kusnetzow, A. K., and Hubbell, W. L. (2009) Osmolyte perturbation reveals conformational equilibria in spin-labeled proteins, *Protein Sci. 18*, 1637-1652.
147. Shin, B.-k., and Saxena, S. (2011) Substantial Contribution of the Two Imidazole Rings of the His13−His14 Dyad to Cu(II) Binding in Amyloid-β(1−16) at Physiological pH and Its Significance, *J. Phys. Chem. A 115*, 9590-9602.
148. Hong, L., Carducci, T. M., Bush, W. D., Dudzik, C. G., Millhauser, G. L., and Simon, J. D. (2010) Quantification of the Binding Properties of Cu2+ to the Amyloid Beta Peptide: Coordination Spheres for Human and Rat Peptides and Implication on Cu2+-Induced Aggregation†, *J. Phys. Chem. B 114*, 11261-11271.
149. Jun, S., Gillespie, J. R., Shin, B.-k., and Saxena, S. (2009) The Second Cu(II)-Binding Site in a Proton-Rich Environment Interferes with the Aggregation of Amyloid-β(1−40) into Amyloid Fibrils, *Biochemistry 48*, 10724-10732.
150. Shin, B.-k., and Saxena, S. (2008) Direct Evidence That All Three Histidine Residues Coordinate to Cu(II) in Amyloid-β1−16†, *Biochemistry 47*, 9117-9123.
151. Jun, S., and Saxena, S. (2007) The Aggregated State of Amyloid-β Peptide In Vitro Depends on Cu2+ Ion Concentration, *Angew. Chem. Int. Ed. 46*, 3959-3961.
152. Dudzik, C. G., Walter, E. D., and Millhauser, G. L. (2011) Coordination Features and Affinity of the Cu2+ Site in the α-Synuclein Protein of Parkinson's Disease, *Biochemistry 50*, 1771-1777.
153. Drew, S. C., Ling Leong, S., Pham, C. L. L., Tew, D. J., Masters, C. L., Miles, L. A., Cappai, R., and Barnham, K. J. (2008) Cu2+ Binding Modes of Recombinant α-Synuclein − Insights from EPR Spectroscopy, *J. Am. Chem. Soc. 130*, 7766-7773.

154. Shin, B.-k., and Saxena, S. (2011) Insight into Potential Cu(II)-Binding Motifs in the Four Pseudorepeats of Tau Protein, *J. Chem. Phys. B 115*, 15067-15078.
155. Kallay, C., David, A., Timari, S., Nagy, E. M., Sanna, D., Garribba, E., Micera, G., De Bona, P., Pappalardo, G., Rizzarelli, E., and Sovago, I. (2011) Copper(ii) complexes of rat amylin fragments, *Dalton Transactions 40*, 9711-9721.
156. Walter, E. D., Stevens, D. J., Spevacek, A. R., Visconte, M. P., Dei Rossi, A., and Millhauser, G. L. (2009) Copper binding extrinsic to the octarepeat region in the prion protein, *Current protein & peptide science 10*, 529-535.
157. Burns, C. S., Aronoff-Spencer, E., Dunham, C. M., Lario, P., Avdievich, N. I., Antholine, W. E., Olmstead, M. M., Vrielink, A., Gerfen, G. J., Peisach, J., Scott, W. G., and Millhauser, G. L. (2002) Molecular Features of the Copper Binding Sites in the Octarepeat Domain of the Prion Protein†, *Biochemistry 41*, 3991-4001.
158. Aronoff-Spencer, E., Burns, C. S., Avdievich, N. I., Gerfen, G. J., Peisach, J., Antholine, W. E., Ball, H. L., Cohen, F. E., Prusiner, S. B., and Millhauser, G. L. (2000) Identification of the Cu2+ Binding Sites in the N-Terminal Domain of the Prion Protein by EPR and CD Spectroscopy†, *Biochemistry 39*, 13760-13771.
159. Ruthstein, S., Stone, K. M., Cunningham, T. F., Ji, M., Cascio, M., and Saxena, S. (2010) Pulsed Electron Spin Resonance Resolves the Coordination Site of Cu2+ Ions in α1-Glycine Receptor, *Biophys. J. 99*, 2497-2506.
160. Sharpe, M. A., Krzyaniak, M. D., Xu, S., McCracken, J., and Ferguson-Miller, S. (2008) EPR Evidence of Cyanide Binding to the Mn(Mg) Center of Cytochrome c Oxidase: Support for CuA−Mg Involvement in Proton Pumping†, *Biochemistry 48*, 328-335.
161. Fittipaldi, M., Steiner, R. A., Matsushita, M., Dijkstra, B. W., Groenen, E. J. J., and Huber, M. (2003) Single-Crystal EPR Study at 95 GHz of the Type 2 Copper Site of the Inhibitor-Bound Quercetin 2,3-Dioxygenase, *Biophys. J. 85*, 4047-4054.
162. Kooter, I. M., Steiner, R. A., Dijkstra, B. W., van Noort, P. I., Egmond, M. R., and Huber, M. (2002) EPR characterization of the mononuclear Cu-containing Aspergillus japonicus quercetin 2,3-dioxygenase reveals dramatic changes upon anaerobic binding of substrates, *European Journal of Biochemistry 269*, 2971-2979.
163. Käss, H., MacMillan, F., Ludwig, B., and Prisner, T. F. (2000) Investigation of the Mn Binding Site in Cytochrome c Oxidase from Paracoccus denitrificans by High-Frequency EPR, *J. Chem. Phys. B 104*, 5362-5371.
164. Lyubenova, S., Siddiqui, M. K., Penning de Vries, M. J. M., Ludwig, B., and Prisner, T. F. (2007) Protein−Protein Interactions Studied by EPR Relaxation Measurements: Cytochrome c and Cytochrome c Oxidase, *J. Chem. Phys. B 111*, 3839-3846.
165. Yang, Z., Kurpiewski, M. R., Ji, M., Townsend, J. E., Mehta, P., Jen-Jacobson, L., and Saxena, S. (2012) ESR spectroscopy identifies inhibitory Cu^{2+} sites in a DNA-modifying enzyme to reveal determinants of catalytic specificity, *Proc. Natl. Acad. Sci. U. S. A.*, In press.
166. Yang, Z., Becker, J., and Saxena, S. (2007) On Cu(II)-Cu(II) distance measurements using pulsed electron electron double resonance, *J. Magn. Reson. 188*, 337-343.
167. Yang, Z., Kise, D., and Saxena, S. (2010) An Approach towards the Measurement of Nanometer Range Distances Based on Cu2+ Ions and ESR, *J. Chem. Phys. B 114*, 6165-6174.

168. van Amsterdam, I. M. C., Ubbink, M., Canters, G. W., and Huber, M. (2003) Measurement of a Cu(II)-Cu(II) distance of 26 Å by a pulsed EPR method, *Angew. Chem., Int. Ed. 42*, 62-64.
169. Yang, Z., Ji, M., and Saxena, S. (2010) Practical Aspects of Copper Ion-Based Double Electron Electron Resonance Distance Measurements, *Applied Magnetic Resonance 39*, 487-500.
170. Kay, C. W. M., El Mkami, H., Cammack, R., and Evans, R. W. (2007) Pulsed ELDOR Determination of the Intramolecular Distance between the Metal Binding Sites in Dicupric Human Serum Transferrin and Lactoferrin, *J. Am. Chem. Soc. 129*, 4868-4869.
171. Lovett, J. E., Bowen, A. M., Timmel, C. R., Jones, M. W., Dilworth, J. R., Caprotti, D., Bell, S. G., Wong, L. L., and Harmer, J. (2009) Structural information from orientationally selective DEER spectroscopy, *PCCP 11*, 6840-6848.
172. Bode, B. E., Plackmeyer, J., Prisner, T. F., and Schiemann, O. (2008) PELDOR Measurements on a Nitroxide-Labeled Cu(II) Porphyrin: Orientation Selection, Spin-Density Distribution, and Conformational Flexibility, *J. Phys. Chem. A 112*, 5064-5073.
173. Narr, E., Godt, A., and Jeschke, G. (2002) Selective measurements of a nitroxide-nitroxide separation of 5 nm and a nitroxide-copper separation of 2.5 nm in a terpyridine-based copper(II) complex by pulse EPR spectroscopy, *Angew. Chem., Int. Ed. 41*, 3907-3910.
174. Jun, S., Becker, J. S., Yonkunas, M., Coalson, R., and Saxena, S. (2006) Unfolding of Alanine-Based Peptides Using Electron Spin Resonance Distance Measurements†, *Biochemistry 45*, 11666-11673.
175. Mathews, C. K., Holde, K. E. V., and Ahern, K. G. (1999) Biochemistry, Prentice Hall.
176. Robinson, B. H., Haas, D. A., and Mailer, C. (1994) Molecular Dynamics in Liquids: Spin-Lattice Relaxation of Nitroxide Spin Labels, *Science 263*, 490-493.
177. Hirsh, D. J., and Brudvig, G. W. (2007) Measuring distances in proteins by saturation-recovery EPR, *Nat. Protocols 2*, 1770-1781.